THESIS

REMOTE VERSUS LOCAL CONTROLS OF EAST PACIFIC INTRASEASONAL VARIABILITY

Submitted by

Adam Rydbeck

Department of Atmospheric Science

In partial fulfillment of the requirements

For the Degree of Master of Science

Colorado State University

Fort Collins, Colorado

Spring 2012

Master's Committee:

Advisor: Eric Maloney

Thomas Birner
Jeffrey Niemann

ABSTRACT

REMOTE VERSUS LOCAL CONTROLS OF EAST PACIFIC INTRASEASONAL VARAIBILITY

The Madden-Julian Oscillation (MJO) is the dominant mode of tropical intraseasonal variability and propagates eastward at 5 m/s with primary signals in wind and precipitation. During boreal summer, interactions between intraseasonal variability in the eastern Hemisphere and the east Pacific warm pool are often described as a local amplification of the propagating MJO. However, the precise mechanism by and degree to which intraseasonal variability in the eastern Hemisphere affects the east Pacific warm pool are not well understood. One school of thought holds that the MJO initiates a dry intraseasonal Kelvin wave response in the west Pacific that rapidly propagates into the Western Hemisphere and initiates intraseasonal convective variability there.

To quantify the relationship between the source (eastern Hemisphere) and amplification region (east Pacific warm pool), sensitivity tests in two separate models are used to determine the importance of local versus remote controls of east Pacific warm pool intraseasonal variability. The two models include the National Center for Atmospheric Research Community Atmosphere Model 3 (CAM3) and the International Pacific Research Center Regional Atmosphere Model (IRAM). The two models use different schemes to isolate the east Pacific from eastward-propagating intraseasonal variability that impinges from the west.

Removing the influence of the MJO on the east Pacific warm pool in these two models reveals different insights into local versus remote control of intraseasonal variability in the east Pacific. The CAM3 produces comparable intraseasonal variability in winds and precipitation in the east Pacific when Kelvin wave signals from the west are removed, suggesting that the Eastern Hemisphere MJO helps to pace east Pacific intraseasonal variability, although east Pacific variability can exist in isolation from the MJO. Thus, the CAM3 supports independent intraseasonal variability in the east Pacific warm pool that may be phase locked to intraseasonal variability in the Eastern Hemisphere in observations. However, the IRAM has very small east Pacific intraseasonal variability when isolated from global MJO signals. The weak intraseasonal variability in IRAM may be a result of mean low-level wind biases that cause 30-90-day surface flux anomalies to be out of phase with 30-90-day precipitation and low-level wind anomalies. As a result, the IRAM model does not support an independent local mode of intraseasonal variability in the east Pacific.

ACKNOWLEDGEMENTS

The research presented in this thesis is indebted to several individuals. I would like to thank Dr. Eric D. Maloney for his invaluable guidance, labor, and insight during this study. I am grateful to Dr. Shang-Pin Xie and Jan Hafner at the International Pacific Research Center in the School of Ocean and Earth Science and Technology at the University of Hawai'i for the work performed in the IRAM model simulations. I would also like to thank Dr. Thomas Birner and Dr. Jeffrey Niemann for serving on my Master's committee and the members of the Maloney Group for their constant availability to answer questions. The NOAA Model Analysis and Prediction Program of the Climate Program Office under contract number NA08OAR4320893 funded this work.

TABLE OF CONTENTS

1. Introduction and Background

1.1. Purpose

The Madden-Julian oscillation (MJO; Madden and Julian 1971; Madden and Julian 1994; Zhang 2005) is the chief mode of intraseasonal variability in the tropics. During boreal summer, intraseasonal variability in the east Pacific warm pool is often described as a local amplification of the eastward propagating MJO that originates in the Eastern Hemisphere. (Knutson and Weickmann 1987; Maloney and Hartmann 2000; Maloney and Kiehl 2002 (a)). However, many possibilities exist for the manner in which the Eastern Hemisphere and east Pacific warm pool interact, as suggested by Maloney and Esbensen (2003) and Maloney et al. (2008). To quantify the relationship between the source and amplification region, sensitivity tests in two distinct models are used to isolate the east Pacific warm pool from intraseasonal variability in other regions, and determine the importance of local versus remote controls of intraseasonal variability there.

1.2. The Madden-Julian Oscillation

1.2.1. Madden-Julian Oscillation Fundamentals

The MJO is the principal mode of tropical intraseasonal variability. It consists of a large-scale circulation coupled response to convection that

produces coherent signals in wind and precipitation. Madden and Julian (1971) first documented the oscillation upon finding spectral peaks of 40-50 day periods in the upper and lower tropospheric zonal winds, surface pressure, and temperature at Canton Island (formerly). Broadly defined, the MJO operates on 30-90 day timescales and propagates to the east at an average speed of 5 m/s in the Indian and west Pacific Oceans. It is dominated by eastward zonal wavenumbers 1-3 in precipitation, and zonal wave number 1 for zonal wind (Zhang 2005). Although it is most evident in the Indian and western Pacific oceans, the MJO affects the entire tropical troposphere.

In the Indian and western Pacific Oceans, the MJO consists of propagating and coherent signals in wind and convection. Equatorial wave dynamics strongly influence the large-scale circulation anomalies that are coherent with MJO convection, and appear important to MJO dynamics. The Gill Model (Gill 1980) shows the circulation response for a resting atmosphere to a positive heating applied at the equator for a linear damped shallow-water equation model on an equatorial β plane. Like the Gill Model, the MJO circulation response involves low-level easterlies (inflow) and upper-level westerlies (outflow) to the east of the heat source, similar to that of an equatorial Kelvin wave. The evolution of an MJO event is shown in figure 1.1. Although the construction of the figure is detailed later, it shows the eastward propagation of both 30-90-day precipitation and 850-hPa horizontal wind anomalies over a composite MJO event. To the west of the positive heating, low-level westerlies and upper-level easterlies are forced. Within this region, cyclonic (anticylonic)

Rossby gyres are found on each side of the equator at the surface (upper-levels). The overturning circulations to the east and west of MJO convection link the active phase of the MJO to the suppressed phase. The convective heating anomaly and the coupled atmospheric circulation propagate eastward at an average speed of 5 m/s in the Eastern Hemisphere until it reaches the dateline. During the transit from the Indian Ocean to the western Pacific Ocean, the phase relationship between the convective center and zonal wind varies. These phase relationships differ from the Gill model. In the Indian Ocean, the convective center is in upper level westerlies and between surface westerlies to the west and surface easterlies to the east. As the MJO moves into the western Pacific Ocean, the convective center moves into upper-level (lower-level) easterlies (westerlies). The MJO convective anomaly is generally limited to the Eastern Hemisphere due to relatively cooler SSTs and reduced climatological convection east of the date line (Hendon and Salby 1994). As MJO convection weakens, the Kelvin-Rossby wave packet associated with the MJO decouples. Uncoupled to convection, the MJO signals in zonal wind and surface pressure propagate eastward across the central and eastern Pacific Ocean as a 30-35 m/s Kelvin wave (Milliff and Madden 1996; Matthews 2000; Zhang 2005 (figure 4)). A dry Kelvin wave has a phase speed of approximately 40-50 m/s. Hence, in addition to the propagating signal, the MJO consists of a radiating atmospheric response to convection (Heckley and Gill, 1984). These emitted signals propagate at speeds much greater than those coupled to convection and can be seen in

surface pressure and low level wind anomalies extending to the Americas (Krishnamurti et al., 1985; Knuston and Weickmann, 1987).

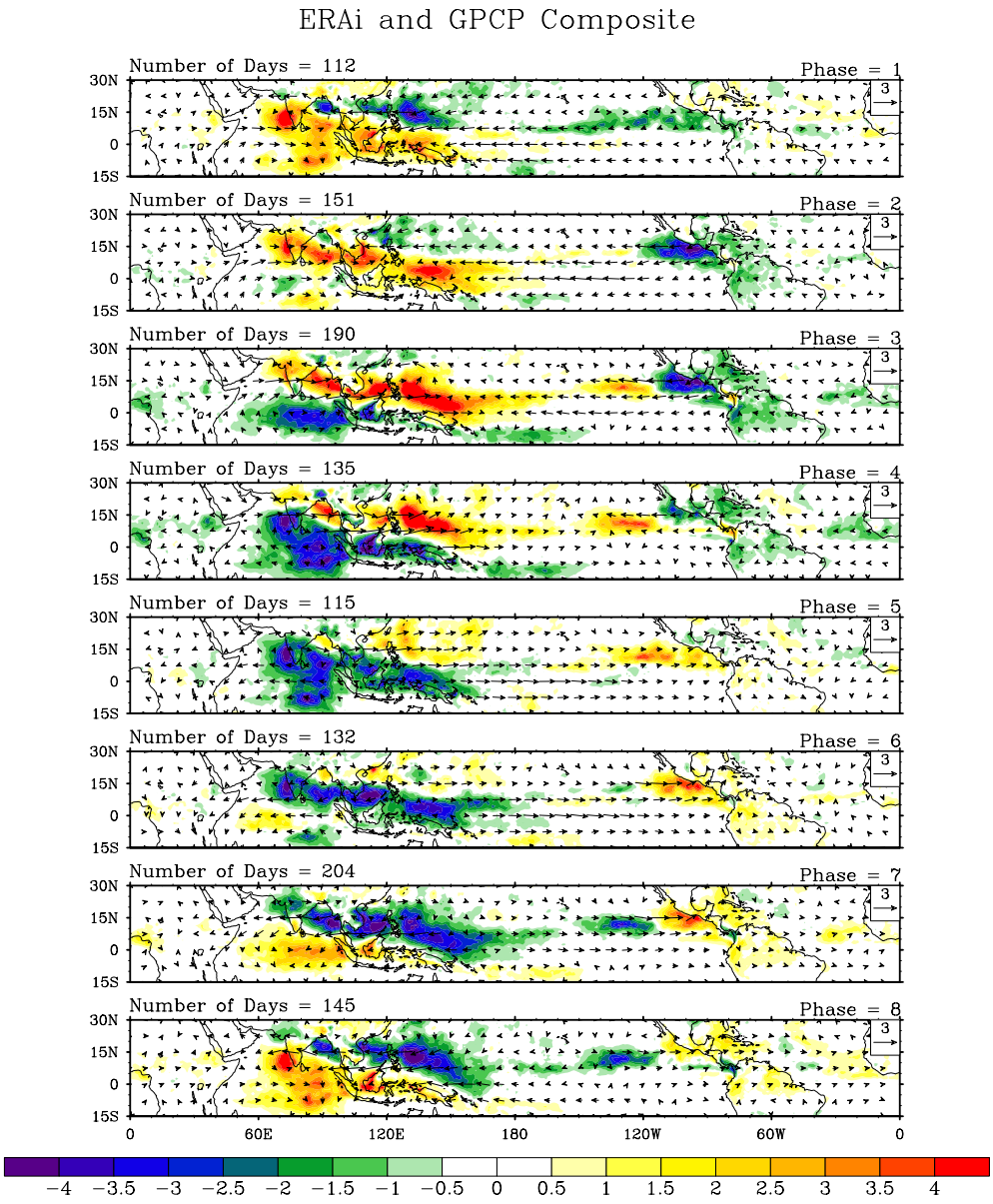

Figure 1.1 ERAi and GPCP composite of 30-90-day 850-hPa horizontal wind anomalies (m/s, vectors) and 30-90-day precipitation anomalies (mm/day, contours) for 1997 – 2008 summers (June – October). The precipitation anomaly contour interval is 0.5 mm/day.

1.2.2. Leading Theories

It is important to briefly discuss leading MJO theories of propagation in order to better understand the intraseasonal signals that enter the east Pacific warm pool and perhaps those mechanisms that might be shared between intraseasonal variability in the Eastern Hemisphere and east Pacific warm pool. A comprehensive theory of the MJO must explain the 30-90 day period, zonal spatial scale selection of wavenumbers 1-3, approximately 5 m/s^{-1} eastward propagation speed in the Eastern Hemisphere that accelerates east of the dateline, and the coupled planetary circulation response to the convective complex. The most popular theories include moisture mode theory (Sobel et al. 2001; Raymond 2001), wind induced surface heat exchange (WISHE) (Emanuel 1987; Neelin et al. 1987) and frictional wave-conditional instability of the second kind (CISK) (Wang 1988; Wang and Li 1994).

Moisture modes exist under weak temperature gradients (Sobel et al. 2001; Raymond and Fuchs 2009) such that diabatic heating is assumed to balance adiabatic cooling to first order. Under this balance emphasis is placed on free tropospheric humidity to determine where convection and column latent heat anomalies occur. Under weak temperature gradient theory, moisture anomalies determine moist static energy anomalies. An additional result of weak temperature gradient theory is that heating anomalies drive vertical motion, which generates vorticity, and hence the large-scale flow. Gross moist stability is the measure used to diagnose the ability of convective processes to grow column moist static energy anomalies, which then supports further convection. Gross

moist stability is defined as the ratio of exported moist static energy from a column by the mean circulation per unit vertical mass flux. When moist static energy sources such as latent heat flux and cloud-radiative feedbacks are incorporated into the definition, it is termed effective gross moist stability. Moisture modes depend on negative gross moist stability because in its absence there is no positive feedback between moist static energy anomalies and diabatic sources to promote instability. If gross moist stability is negative, the actions of convection cause a decrease in column moist static energy, weakening convection. Modeling studies of moisture modes show that they can propagate eastward through moisture advection (Sobel et al. 2001; Maloney 2009).

In linear WISHE theory (Emanuel 1987, Neelin et al. 1987), eastward propagating convective disturbances in regions of climatological easterlies are produced by enhanced surface heat fluxes in anomalous easterlies. The enhanced fluxes to the east of convection help maintain the convective disturbance by supporting convective heating in regions of anomalous temperature anomalies, thus generating eddy available potential energy. The disturbance also moves eastward as a result of the formation of convection to the east of the original convective complex. While linear WISHE theory differs in details from observations, particularly in the direction of the mean wind (Lin and Johnson 1996, Zhang and McPhaden 2000), convective destabilization due to wind induced surface fluxes and cloud-radiative feedbacks have shown to be important to the MJO (Raymond et al. 2009; Maloney et al. 2010; Landu and Maloney 2011). Because anomalous surface fluxes have been shown to be

important in model studies of the MJO (Maloney and Sobel 2004;Sobel et al. 2010; Maloney et al. 2010), nonlinear WISHE theories that operate in mean westerlies may be useful for explaining some aspects of MJO dynamics.

Frictional wave-CISK theory first suggested by Wang (1988) was based on a simple modeling study with a 2-layer troposphere and ½ layer boundary layer model where heating is parameterized based on tropospheric low-level convergence and boundary layer frictional convergence. This theory expands on the traditional wave-CISK theory that describes the positive feedback between latent heating and moisture convergence by including the effects of surface friction such that the instability does not collapse to the smallest scales. In this study, boundary layer frictional moisture convergence ahead of the convective complex in the equatorial wave trough supports instability in the stable regime of wave-CISK. The phase relations between interior wave convergence and friction-induced moisture convergence helps to suppress the growth of the shortest wavelengths. Maloney and Hartmann (1998) showed that frictional moisture convergence takes place ahead of the MJO convective complex and is important in moistening the atmosphere ahead and thus regulating the timing for convection to occur. Additionally, in general circulation models, boundary layer frictional moisture convergence has been shown to be important to the MJO (Waliser et al. 1999, Maloney 2002).

1.3. East Pacific Intraseasonal Variability

1.3.1. East Pacific Basics

Numerous studies have suggested the importance of the mean background state to the MJO (Hendon et al. 2000; Kemball-Cook et al. 2002; Inness et al. 2003). Thus, it is important to understand the summer climatological conditions of the east Pacific warm pool. Similar to previous studies like Xie et al. (2005) and Maloney et al. (2008), the east Pacific warm pool is defined as the region north of the equator off the coast with SSTs above 27° C most of the year (see Maloney et al. 2008 figure 1). Mean SST determines the geographical preference for MJO convective activity by keeping moist static stability low (Neelin and Held 1987). Figure 1.2 shows mean GPCP precipitation and ERAi 850-hPa horizontal winds in this region for the 1996-2008 summer seasons (June-October). The precipitation maximum associated mainly with the ITCZ that stretches along 9° N has values above 12 mm/day. The precipitation maximum is twice as strong in summer as in winter, causing the annual mean to resemble the summer mean (Xie et al. 2005). The precipitation maximum is also centered in the convergence zone of the meridional winds. Strong meridional precipitation gradients exist to the north and south of the precipitation maximum. The minimum in precipitation along and south of the equator is associated with climatological SSTs below 26° C year round, including a notable equatorial cold tongue.

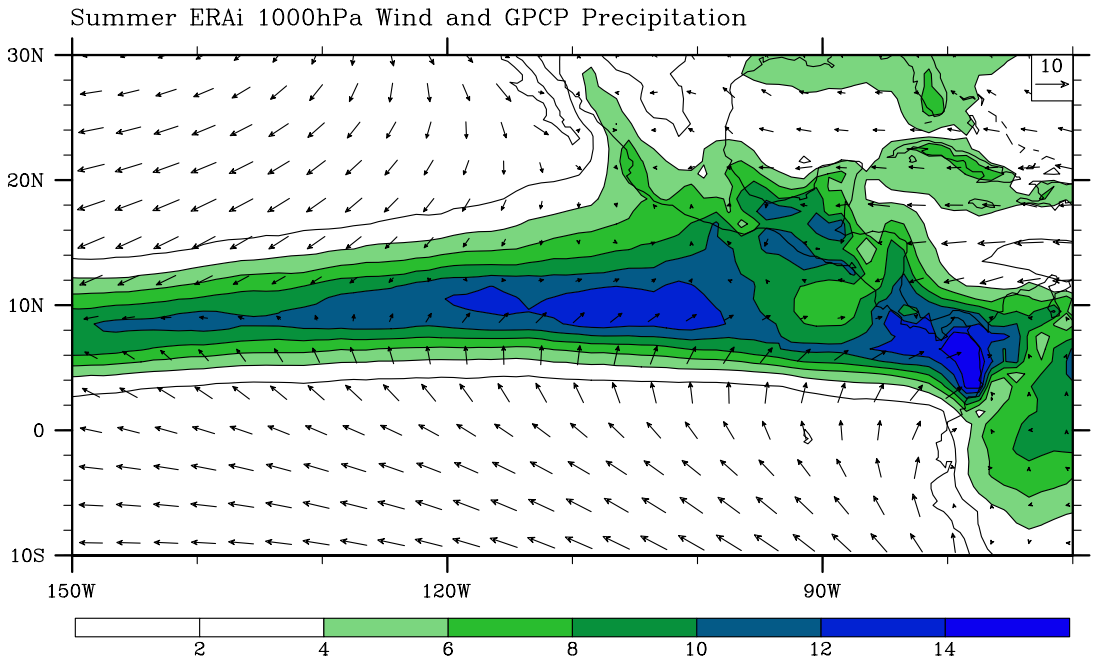

Figure 1.2 Mean summer (June – October) ERAi 1000-hPa horizontal winds (vectors, m/s) and GPCP precipitation (contours, mm/day).

Just to the east of the ITCZ precipitation maximum, a relative minimum in precipitation forms a dry hole in the precipitation field near 10°N, 90°W. Xie et al. (2005) showed that the zonally oriented Papagayo jet induces upwelling through positive wind stress curl producing a shallow thermocline feature called the Costa Rica dome. Although the Papagayo jet weakens during the summer, the Costa Rica Dome is able to persist and maintain a cold spot that suppresses local convection due to the presence of positive wind stress curl produced by monsoonal westerly surface flow. The precipitation maximum to the east of the Costa Rica Dome dry hole in the Panama Bight is related to the strong diurnal cycle of precipitation originating over the Andes Mountains and propagating westward at approximately 15 m/s. The propagation speed is in good agreement with that of a gravity wave in a baroclinic atmosphere (Mapes 2003, Part I and

III). Additionally in figure 1.2, trade wind easterlies dominate the wind field of tropical east Pacific Ocean except for the east Pacific warm pool where weak 1000-hPa westerlies persist. Similar results are found using QuikSCAT 10 m wind data for June – September averages (Maloney and Esbensen 2007, figure 1b). The maxima in precipitation are mostly located in the westerly wind region.

Another unique feature of the east Pacific is the moist static energy budget as it is affected by the depth of convection in the ITCZ. In contrast to other tropical convergence zones, the east Pacific mean vertical circulation imports moist static energy, resulting in a moist static instability that must be relieved by tropical and extratropical eddies (Back and Bretherton 2006; Peters et al. 2008). In the east Pacific, the mean moist static energy of detraining air is much lower than that of the west Pacific (Back and Bretherton 2006). During periods of shallow convection, a moist static energy surplus results, implying negative gross moist stability, which is favored for MJO moisture mode instability.

1.3.2. Characteristics of East Pacific Intraseasonal Variability

During boreal summer, low-level zonal winds and precipitation in the east Pacific warm pool contain significant spectral peaks near 50 days (Maloney and Esbensen 2003; Maloney et al. 2008). One leading characteristic of intraseasonal variability in the tropical Pacific Ocean is alternating periods of westerly and easterly low-level zonal wind anomalies (Maloney and Hartmann 2001). These alternating periods are at least partially related to Northern Hemisphere MJO convective anomalies in the west Pacific Ocean that are associated with a large-scale atmospheric circulation response that extends to

the Americas. During westerly flow periods, a quasi-stationary enhancement of convection typically occurs in the east Pacific warm pool. For easterly flow periods, a suppression of convection occurs (Maloney and Hartmann 2000; Maloney and Esbensen 2003; Maloney and Esbensen 2007). Because the east Pacific warm pool has a background westerly flow during the summer east of 120° W, intraseasonal westerly anomalies constructively add to the background flow and enhance surface latent heat fluxes (Maloney and Esbensen 2003, Sobel et al. 2010). Maloney and Esbensen (2003) showed that perturbation available potential energy generation maximizes during periods of strong intraseasonal convection and low-level westerly wind anomalies in the east Pacific warm pool. Maloney and Hartmann (2000) suggested a possible role for local convection and circulation feedbacks whereby circulation anomalies are locally amplified through interaction with convective heating, after being triggered from the west. Intraseasonal easterly periods are associated with suppressed intraseasonal precipitation and latent heat fluxes (Maloney and Esbensen 2003; Maloney and Esbensen 2007).

The enhanced convection associated with the intraseasonal westerly wind anomalies progresses eastward and slowly northward with time (Maloney et al. 2008). Composite plots of Maloney and Esbensen (2007) show a zonal dipole structure in precipitation with a nodal point near longitude 120°W. During the life cycle of an east Pacific intraseasonal oscillation event, precipitation initiates outside of the east Pacific warm pool to the west of 120° W under surface easterlies and persists for 10 – 15 days. Afterwards, precipitation to the west of

120°W is suppressed and precipitation in the warm pool is enhanced under surface westerlies (Maloney and Esbensen 2007, figure 3). The greatest intraseaonal precipitation variance is in the east Pacific warm pool and is significantly correlated with the MJO time series (Maloney et al. 2008).

1.3.3. Proposed Theories for East Pacific Intraseasonal Variability

As suggested by Maloney et al. (2008), there are many possible interactions between intraseasonal variability in the tropical Eastern Hemisphere and the east Pacific warm pool. They are broken down here into the simplest two categories. The boldest category is that of independence of the Eastern Hemisphere and east Pacific intraseasonal timescales. Within this category it is possible that the two intraseasonal oscillations are phased locked and have synchronized pulses. If hypothetically buffered from the surrounding physical environment, the east Pacific warm pool would produce an independent intraseasonal oscillation. This category most importantly suggests that the requirements and mechanisms for an intraseasonal oscillation are entirely locally available, which may have important implications about intraseasonal convective variability in general. The second category is that of east Pacific dependence on the Eastern Hemisphere. Significant east Pacific intraseasonal variability cannot exist without communication from the Eastern Hemisphere. The intraseasonal variability observed in the east Pacific is to some degree remotely forced and maintained from the Eastern Hemisphere. Additionally, it is possible that no local feedbacks are necessary for the initiation and maintenance of east Pacific intraseasonal variability.

The literature contains hypotheses that support the independence of the intraseasonal oscillations in the Eastern Hemisphere and east Pacific. In the absence of any outside forcing, intraseasonal variability in the east Pacific warm pool at periods of 50-days could be sustained. Zhang and Dong (2004) using observational data of low level winds and precipitation suggest that intraseasonal signals in the Eastern Hemisphere and east Pacific are disconnected. The absence of strong MJO signals along the ITCZ between the west Pacific and east Pacific and the lack of continually propagating deep convection lead the authors to conclude no direct relationship exists between the two intraseasonal oscillations. Additionally, Jiang et al. (2011) evaluates the representation of east Pacific intraseasonal variability among 11 climate models. In models with the most realistic representation of east Pacific intraseasonal variability, the convective signals originate in the central Pacific. Thus, the eastward propagating MJO that originates in the Indian Ocean is not necessary in some of the models for the initiation of east Pacific intraseasonal variability.

The second category includes theories that support the dependence of the east pacific intraseasonal variability on the propagating MJO signal from the Eastern Hemisphere. If isolated from eastward propagating intraseasonal signals, the east Pacific would have negligible intraseasonal variability. Evidence does exist in the literature for the importance of remote forcing. Precipitation and sea surface temperature (SST) anomalies in the east Pacific warm pool are significantly correlated with the MJO time series (Maloney et al. 2008). The high correlation suggests that remote forcing from the Eastern Hemisphere by the

MJO is important for intraseasonal variability in the east Pacific warm pool in some way. Additionally, composite plots that utilize an MJO index based on multivariate empirical orthogonal functions (EOFs) from 30-90-day bandpass filtered equatorial fields of outgoing longwave radiation, 850mb zonal wind, and 200mb zonal wind anomalies (Wheeler and Hendon 2004) show a timely evolution of MJO dynamical signals from the Indian Ocean, across the west and central Pacific Ocean, and into the east Pacific warm pool. Similar conclusions are seen in RMM based phase diagrams of MJO propagation and amplitude of Wheeler and Hendon and Hovmueller diagrams of precipitation and low-level zonal winds. These plots indicate that the phase of the propagating MJO determines the phase of the intraseasonal variability in the east Pacific warm pool.

Strong evidence exists for the hypothesis that stresses both the importance of remote influence and local feedbacks for east Pacific intraseasonal variability. A reasonable theory for the strong relationship between the global MJO signal and the intraseasonal variability in the east Pacific during boreal summer is described simply as a local amplification of the eastward propagating MJO. The MJO loses much of its convective coupling near the dateline. As a result, it propagates at much faster speeds, like that of a Kelvin wave, due to an increased effective equivalent depth. Upon entering the east Pacific warm pool, convective coupling reoccurs, the equivalent depth is reduced, and the propagation speed is slowed. It is possible that the Kelvin wave signal from the MJO impinges on the western flank of the east Pacific warm pool causing an

intensification of MJO convection through enhanced latent heat fluxes by anomalous westerlies adding constructively to mean westerlies.

Similarly, Small et al. 2010 proposes a theory for the remote forcing of east Pacific intraseasonal variability from an MJO initiated Kelvin wave response. During the suppression of MJO convection in the Eastern Hemisphere, a dry Kelvin wave propagates eastward as a wave response to a negative heating anomaly (Gill 1980). Associated with the Kelvin wave response are cool tropospheric temperature anomalies and equatorial westerly surface anomalies that are rapidly communicated to the east Pacific. Ekman convergence is then initiated on the northern flank of the Kelvin wave in the east Pacific to begin an intraseasonal event. Support for surface meridional convergence is seen in QuikSCAT surface winds of MJO-related intraseasonal events and in the composites shown later in this study (Maloney and Esbensen 2007).

1.4. Impacts of East Pacific Intraseasonal Variability

The east Pacific warm pool contains a major tropical convective center. Such an area of intense convection is important for global circulation patterns and climate. During boreal summer, the Western Hemisphere warm pool that includes parts of the eastern North Pacific, the Gulf of Mexico, the Caribbean, and the western tropical North Atlantic supports the summer Hadley circulation of the Western Hemisphere (Wang and Enfield 2003). The region of the intertropical convergence zone located in the east Pacific warm pool is well known to have shallow mode and deep modes of convection (Zhang et al. 2004,

Nolan et al. 2007, Nolan et al. 2010). Periods of shallow convection in the east Pacific have been shown to transition to deep convection in the presence of tropical and extratropical eddies. The depth of convection impacts the export of moist static energy in this region and thus the sign of gross moist stability (Back and Bretherton 2006, Back and Bretherton 2009).

If the intraseasonal variability located in the east Pacific warm pool is considered to be a local amplification of the globally propagating MJO signal, the recoupling of convection that occurs in the east Pacific to the eastward moving dynamical signals of the MJO have important consequences for the propagation speed of the MJO. Yu et al. (2011) suggested that the delayed impact of the MJO on surface winds and pressure in the Atlantic Ocean might be a result of the convective coupling that occurs in the east Pacific warm pool. Such a delay has potential impacts for the proposed MJO pathway through the Isthmus of Panama and into the Caribbean Sea, Gulf of Mexico, and Atlantic Ocean.

The MJO has a strong statistical relationship with tropical cyclone development in the east Pacific, Gulf of Mexico, and western Caribbean Sea. Because of the landfall that often occurs with tropical cyclones located in the Gulf of Mexico and western Caribbean, this research has received the most attention. Associated with the propagation of the MJO into the Western Hemisphere are alternating periods of intraseasonal easterly and westerly surface wind anomalies that are added to the mean flow. Westerly phases of the MJO are associated with a four times greater likelihood of hurricane genesis versus easterly phases in the east Pacific. Similarly strong relationships for tropical cyclone activity are

found in the western Caribbean and Gulf of Mexico for westerly and easterly phases of the MJO (Maloney and Hartmann 2000; Maloney and Hartmann 2001; Maloney and Hartmann 2002). This impact is particularly important because the ability of the east Pacific warm pool to produce intraseasonal variability independent of the Eastern Hemisphere has large implications for tropical cyclone prediction in these regions. The lead-time for prediction may be greater if Western Hemisphere intraseasonal variability is tied to slowly evolving MJO activity in the Eastern Hemisphere. Additionally, MJO signals are observed in the North American Monsoon. Easterly waves and tropical cyclones in the east Pacific that are modulated by periods of intraseasonal easterly and westerly low level winds are potentially important mechanisms for triggering gulf moisture surges up the Gulf of California and into northwest Mexico and Arizona (Bordoni and Stevens 2006).

The MJO is theorized to influence coupled ocean-atmosphere variability on longer interannual timescales. Although models of MJO and El Nino Southern Oscillation (ENSO) interactions are still unrefined, there is observational support for strong MJO events to precede the beginning and development of major ENSO warm events (McPhaden 1999, 2004). In initial scientific endeavors to identify the relationship between the two oscillations, the MJO was thought to be a source of stochastic forcing for ENSO (Jin et al. 1996). MJO forcing through westerly wind bursts could produce a downwelling Kelvin wave to initiate an ENSO event and could more generally explain the broader range of ENSO periods through stochastic forcing (Neale et al. 2008).

1.5 Study Overview

This study is organized as follows. Chapter two provides detailed descriptions of the models used to analyze east Pacific intraseasonal variability and the observational data used for comparison. This section also contains the methodology for time filtering and compositing both observational and model data to describe the intraseasonal events. Chapter three details the results from the control simulations and the simulations that isolate the east Pacific from remote intraseasonal influences. The effectiveness of the isolation techniques is first determined. A summary, conclusions, and future work are presented in chapter four.

2. Data and Methodology

2.1. Models and Data

In order to test the independence of intraseasonal variability in the east Pacific from that in the Eastern Hemisphere in a model, the east Pacific must be isolated on intraseasonal timescales (30-90 days). The intraseasonal isolation of the east Pacific ensures that non-local signals are not influencing local intraseasonal variability. Several methods can be used to achieve this goal. The first method is the removal of MJO activity in the Eastern Hemisphere through the suppression of surface latent heat fluxes in the Indo-Pacific warm pool. If the MJO is not able to initiate, it is not able to influence intraseasonal variability in the east Pacific. Another method is the suppression of Kelvin wave signals that propagate eastward into the east Pacific. The final method used in this study is the use of boundary conditions that are filtered to remove 30-90 day forcing signals.

2.1.1. NCAR CAM3

The National Center for Atmospheric Research (NCAR) Community Atmosphere Model 3 (CAM3) is used in this study. The standard deep convection parameterization of Zhang and McFarlane (1995) is substituted in the model for the Relaxed Arakawa-Schubert (RAS) convection scheme of Moorthi

and Suarez (1992). In the RAS convection scheme we use here, both a minimum entrainment rate and convective rainfall re-evaporation into unsaturated air aid in more realistic intraseasonal variability (Tokiaka et al. 1988; Sud and Molod 1988). As in previous modeling studies, the convection scheme substitution improves intraseasonal variability globally (Maloney and Sobel 2004; Maloney 2009; Hannah and Maloney 2011) and in the east Pacific warm pool during boreal summer (Maloney and Kiehl 2002 (b); Maloney and Esbensen 2005). Eric Maloney and Walter Hannah of the Department of Atmospheric Science at Colorado State University have significantly improved the representation of intraseasonal variability both globally and in the east Pacific in CAM3, and this study is indebted to their efforts (Hannah and Maloney 2011).

For all simulations using CAM3, the horizontal resolution is T85 (approximately 1.4° x 1.4°). The spectral resolution is increased from the typical T42 resolution of former studies to better resolve features such as the topography in Mexico and Central America and mesoscale precipitation structures like those associated with the Costa Rica thermocline dome (Maloney and Esbensen 2005; Xie et al. 2005). The model uses twenty-six vertical levels with a 20-minute time step. For the CAM3 control run, observed daily SSTs and insolation were used over a 10-yr period.

2.1.2. Isolation of East Pacific Intraseasonal Variability in Models

Although it has been well documented that general circulation models have difficulty initiating and maintaining intraseasonal variability (Zhang 2005; Zhang et al. 2006), efforts to terminate and remove intraseasonal variability have

received much less attention. The latter is admittedly not as great or relevant a problem as the former, but is important for testing our hypothesis, and for testing physical processes in general. Several methods are employed to isolate the east Pacific from the influence of the MJO in the CAM3 and IRAM models.

2.1.3. Suppressed Surface Fluxes Simulations

In CAM3, the easiest way to eliminate the influence of the MJO on the east Pacific warm pool is to remove the MJO. Because intraseasonal surface flux variability (or surface moist enthalpy flux variability) is thought to be fundamental in the development and maintenance of intraseasonal oscillations (Maloney and Sobel 2004; Sobel et al. 2010), reducing surface fluxes to their climatology should significantly weaken and perhaps remove intraseasonal oscillations. In our first sensitivity experiment, we attempt to suppress the MJO in the Eastern Hemisphere by suppressing interactive surface latent heat fluxes.

For the CAM3 suppressed surface fluxes run, observed climatological SSTs and insolation were also used over a 10-yr period. However, the experimental run used climatological surface latent heat fluxes in the region surrounding the Indo-Pacific warm pool (45°E - 150°W, 30°S - 30°N). Similar efforts to suppress surface flux variability were performed in Maloney and Sobel (2004). They refer to the simulation using climatological surface latent heat fluxes as the No-WISHE simulation. Since the experimental simulation not only removes the influence of wind speed on surface latent heat flux, but also the effects of low-level specific humidity variations, using the term No-WISHE is somewhat of a misnomer. However, tropical latent heat flux variations

associated with the MJO are overwhelmingly dominated by the wind-driven component.

2.1.4. Sponge Region Simulations

A separate model setup was used for the sponge region simulations to suppress Kelvin wave propagation from the Eastern Hemisphere into the east Pacific. Like the control simulation, the sponge region model run used perpetual August 15th SSTs and insolation. To remove Eastern Hemisphere intraseasonal variability from propagating eastward into the east Pacific warm pool, a sponge region is added to the CAM3 model. The sponge region defines an area of relaxation toward climatology from -20° – 20°N, 175° – 145°W. The relaxation is of the form:

$$U_{sponge} = U_{CAM3} + (\Delta t/\Gamma)(U_{climatology} - U_{CAM3}) \qquad (2.1)$$

for temperature, dry static energy, zonal wind, meridional wind, specific humidity, and surface pressure. Γ is the relaxation timescale and is defined to be 1 day for the purposes of this simulation. Δt is the time step. This particular choice of relaxation timescale effectively damps a 35 m/s phase speed Kelvin wave propagating across the sponge region. The sponge region acts on the variables through all vertical levels.

2.1.5. IRAM

Because the east Pacific is a region of complex topography, oceanographic structure, and mesoscale jet features, a regional model is particularly useful to study the intraseasonal variability of this region. The major motivation for using a regional model is to be able to control the boundary

conditions. The International Pacific Research Center Regional Atmosphere Model (IRAM) used in this study solves the hydrostatic primitive equations in spherical coordinates in the horizontal and in a terrain-following sigma coordinate in the vertical. The model has 28 vertical levels with 11 levels below 800 hPa to better resolve processes in the atmospheric boundary layer. The model domain used here ranges from 25°S to 45°N and 150° to 30°W with the unstaggered 0.5° X 0.5° model grid covering approximately one-third of the global tropical belt. IRAM includes a physical package for convection, cloud, radiation, and turbulent mixing that is detailed in Wang et al. (2004). Except for the SST taken from the National Centers for Environmental Prediction/Marine Modeling and Analysis Branch analysis, the initial and boundary conditions for IRAM are from NCEP/NCAR reanalysis. Precipitation is not explicitly passed to IRAM at the boundaries and thus it must be generated based on the passed moist thermodynamic variables.

The IRAM has shown increased skill in resolving the climatology of the eastern Pacific versus typical general circulation models. Such successes include the atmospheric adjustment to the equatorial front north of the equator (Small et al. 2005), atmospheric boundary layer clouds over the southeast Pacific (Small et al. 2003), and orographic effects of the Central American mountains (Xu et al. 2005). More importantly to this study, IRAM has significant ability in simulating realistic intraseasonal variability. In addition to a realistic overall level of intraseasonal variability and realistic spatial structure, a correlation of 0.5 exists between the 850-mb zonal wind of the coupled model and observations on

the equator in the intraseasonal band over the 1998 – 2003 period. This correlation exceeds the 95% significance level (Xie et al. 2007). In a study of the same coupled model in Small et al. (2010), 30-90-day filtered 850-hPa zonal winds between 10°N - 15°N, 130°W - 100°W were used to capture the intraseasonal signal in a zonal wind index for the coupled model and observations, respectively. The correlation of the model index and observational index was 0.8 at zero lag, which is significant at the 99% confidence level. Small et al. (2010) found that east Pacific warm pool intraseasonal convection and winds agree in phase with those from observations. Additionally, the study found that convective variability in IRAM has only a weak dependence on the SST variability, but a stronger dependence on the climatological SST. As a result, ocean-atmosphere coupling is not used in the present study even though significant spectral peaks of 50-days exist in the east Pacific warm pool SST (Maloney et al. 2008).

A notable difference in the IRAM between this study and the study of Small et al. (2010) is the sign of the mean boreal summer low-level winds in the east Pacific warm pool. In this study the winds are easterly, while in the study of Small et al. (2010) and in observations the winds are westerly. The sign of the mean winds in the east Pacific warm pool are important because they help determine the sign of the total wind during an intraseasonal event in the east Pacific warm pool. The total wind is defined as the mean wind plus the 30-90-day wind anomalies and is critical in determining the phase of wind induced surface heat flux anomalies during an intraseasonal event.

2.1.6. Filtered Boundary Conditions Simulations

A 12 year simulation from 1997 – 2008 was run for IRAM with no modifications performed to the initial and boundary conditions, known as the IRAM control model run. To remove intraseasonal variability from propagating into the IRAM domain from the Eastern Hemisphere, a 30-90 day bandpass filter was applied to the initial and boundary conditions. The filtering was performed on all lateral model boundaries and through all vertical levels. In the lateral boundaries, the model is nudged towards four-times daily values of temperature, humidity, and wind components from NCEP/NCAR reanalysis in a 6° wide buffer zone. The filtered boundary conditions effectively remove the propagating MJO signal and thus the ability of the MJO to force the atmospheric model. This simulation is called the IRAM filter model run.

2.1.7. Observational Data

The following data products comprise the observational truth used to assess the models. The CAM3 simulations are compared with GPCP and ERAi products. Since the IRAM model boundary conditions use the same NCEP/NCAR reanalysis, the IRAM model is compared with GPCP and NCEP/NCAR reanalysis.

2.1.7.1. GPCP

The Global Precipitation Climatology Project (GPCP) 1-degree daily combination dataset contains total precipitation at one-degree daily resolution from 1997- 2008. The GPCP Global Merge Development Centre developed the estimates of tropical precipitation used for this study. Between 40°S – 40°N, the

estimates are from the Threshold Matched Precipitation Index based on infrared temperatures for cold pixels (Huffman et al. 2001).

2.1.7.2. ERAi

The European Center for Medium-Range Weather Forecasts (ECMWF) interim global reanalysis product, ERAi, was produced to replace the ERA-40 reanalysis. Improvements of ERAi over ERA-40 include better representation of the hydrologic cycle, stratospheric circulation, and time consistency of reanalysis fields (Dee et al. 2011). ERAi has 1.5°x1.5° grid spacing and 37 vertical levels over the selected 12 year period of 1997 – 2008.

2.1.7.3. NCEP/NCAR

The joint reanalysis project between the National Center for Environment Prediction (NCEP) and the National Center for Atmospheric Research (NCAR) is used in this study both as boundary inputs for IRAM and as an observational dataset to compare with models. Daily data is available at 17 pressure levels with 2.5° grid spacing (Kalnay et al. 1996). Although coarser than ERA-interim data, NCEP/NCAR reanalysis provides a good reference for IRAM because the model uses the NCEP/NCAR reanalysis for the initial and boundary conditions.

2.2. Methodology

2.2.1. Time Filters

Because intraseasonal signals are of physical interest for this study, time filtering is used to isolate them. To retain the dominant MJO signals of 40-50-days in the CAM3, the IRAM, and observational data, a linear non-recursive

digital bandpass filter with half-power points at 30 and 90 days is applied to the data. The application of the 30-90-day bandpass filter creates intraseasonal anomalies that have nearly full frequency power at 40-50 day timescales. Both the 30 and 90-day filters have fifty-nine weights, resulting in the loss of one hundred eighteen days from the beginning and end of the time series. To smooth the response function, Lanzcos smoothing is applied to the filter weights. Additionally, bandpass filters have the ability to make noise appear somewhat periodic. As a result, significance testing is essential to determine those signals and statistical relationships that are not likely to be random. Predetermined significance levels of 95% are used throughout the study and degrees of freedom are based on twice the *e*-folding timescale of the equatorially averaged 30-90-day 850-hPa zonal winds, 80 days.

2.2.2. Composites

In this study composites are useful to show the spatial patterns of atmospheric intraseasonal variability as they develop over time. Compositing is based on significant intraseasonal events, those determined to be greater than at least one standard deviation from zero using some index of intraseasonal variability. Compositing is based on indices derived from atmospheric variables that represent intraseasonal activity such as outgoing longwave radiation, precipitation, and/or lower/upper tropospheric zonal winds. For typical composites, the data is initially bandpass filtered to 30-90-days after the seasonal cycle and time mean are removed. The data is then normalized. For the lag composites used in this study, the normalized first principal component (PC)

of 30-90-day 850-hPa zonal wind and precipitation anomalies over the east Pacific (10°S - 25°N, 150°W - 70°W) must be one and a half standard deviations from zero and a relative maximum to be considered a significant event. During the selection process, events are not allowed to occur 20 days before or after another event. Data lagged at intervals of -20, -15, -10, -5, 0, 5, 10, and 15 days for particular 30-90-day variables are then averaged to give a lag composite plot.

Intraseasonal events are also composited based on global indices of the MJO (Wheeler and Hendon 2004). Multivariate empirical orthogonal functions (EOFs) are calculated from 15°S - 15°N averaged and 30-90-day bandpass filtered 850-hPa zonal wind, 200-hPa zonal wind, and precipitation anomalies. The data is also normalized. The multivariate EOFs describe the eastward propagating signal of the MJO and are shown in figures 2.1, 2.2, and 2.3 for ERAi/GPCP reanalysis, the CAM3 control model, and the CAM3 filter model, respectively. The bandpass filtered anomalies are then projected onto the first two EOFs to form two PC time series that are used as a basis for compositing. To qualify as an MJO event, the amplitude given in equation (2.2) must be greater than 1 similar to Wheeler and Hendon (2004). Furthermore, the phase can be determined from equation (2.3).

$$Amplitude = \sqrt{PC1^2 + PC2^2} \qquad (2.2)$$

$$Phase = \arctan\left({}^{PC1}/_{PC2}\right) \qquad (2.3)$$

A plot of MJO amplitude for reanalysis data is shown in figure 2.4. MJO phases are defined based on eight equal angular segments of width 45°. Considering that one MJO event lasts approximately 50 days, each MJO phases lasts 5-6 on

average. Our index differs from that of Wheeler and Hendon (2004) in that we bandpass filter the data before evaluating the EOFs and precipitation is used instead of outgoing longwave radiation as a proxy for convection.

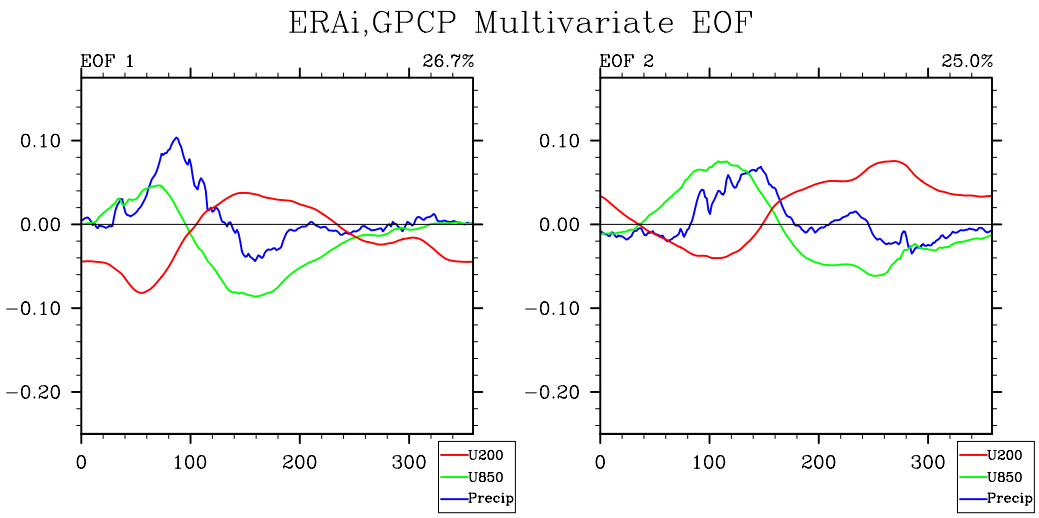

Figure 2.1 First two multivariate EOFs of ERAi/GPCP reanalysis are shown with percent variance explained in the upper right hand corner of each plot. EOFs are based on 15°S - 15°N averages of 30-90-day filtered 200-hPa zonal wind (red), 850-hPa zonal wind (green), and precipitation (blue) anomalies. The plot abscissa is longitude.

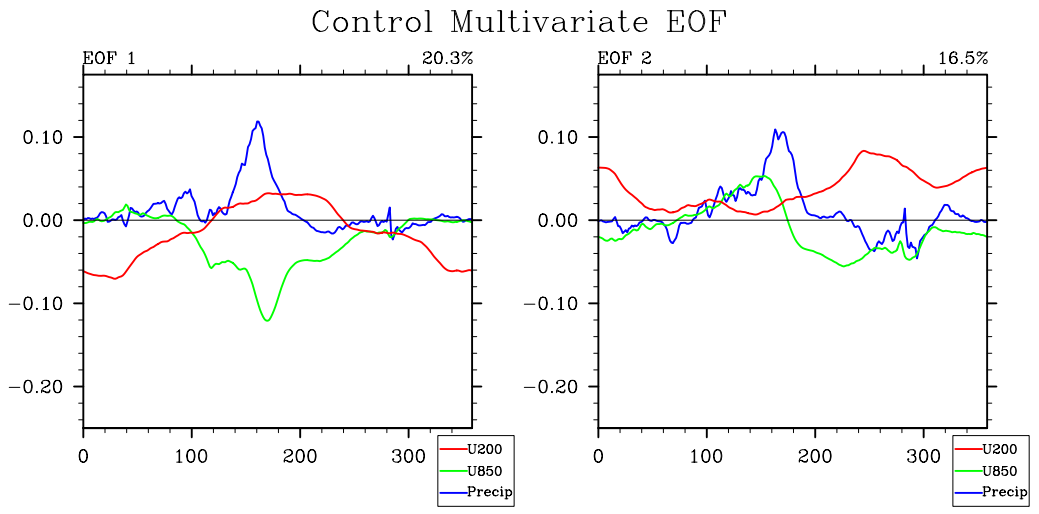

Figure 2.2 First two multivariate EOFs of the CAM3 control model are shown with percent variance explained in the upper right hand corner of each plot. EOFs are based on 15°S - 15°N averages of 30-90-day filtered 200-hPa zonal wind (red), 850-hPa zonal wind (green), and precipitation (blue) anomalies. The plot abscissa is longitude.

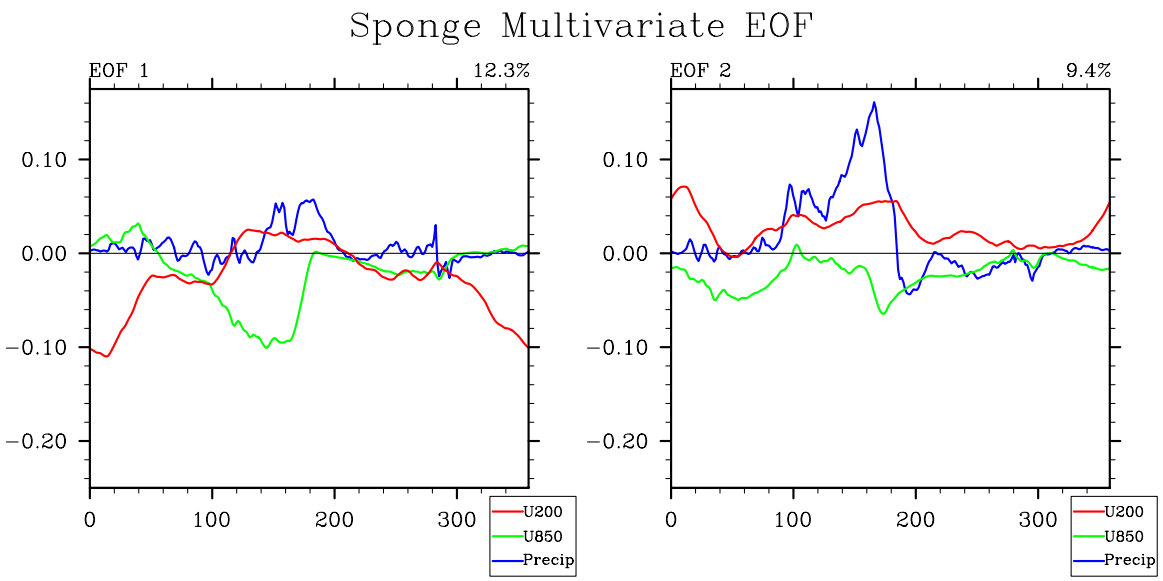

Figure 2.3 First two multivariate EOFs of the CAM3 sponge model are shown with percent variance explained in the upper right hand corner of each plot. EOFs are based on 15°S - 15°N averages of 30-90-day filtered 200-hPa zonal wind (red), 850-hPa zonal wind (green), and precipitation (blue) anomalies. The plot abscissa is longitude.

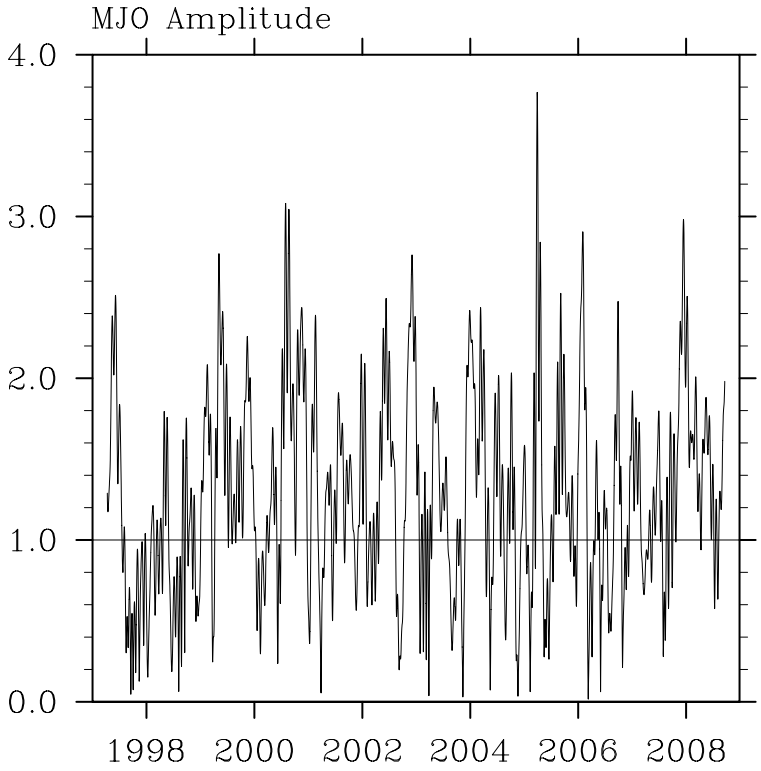

Figure 2.4 MJO Index Amplitude from 1997 – 2008 for ERAi and GPCP reanalysis data.

Special consideration is taken when using a global index to describe intraseasonal activity in IRAM. The boundaries of IRAM do not span the tropical belt and thus a global index based on only IRAM data is not possible. However, since IRAM uses input from NCEP/NCAR reanalysis data, a global index is based on the reanalysis data and applied to IRAM. The indices used to composite an MJO event are taken from the NCEP/NCAR reanalysis and GPCP precipitation, and the time steps used to describe a particular phase of an MJO event are applied to IRAM. The primary assumption for these composites is that IRAM has intraseasonal variability of comparable timing and magnitude to NCEP/NCAR reanalysis such that the index derived from the NCEP/NCAR reanalysis adequately describes the process in the domain of IRAM. Care should be taken when interpreting the results. IRAM takes time to initiate convection since the reanalysis only passes moist thermodynamic values, and not vertical velocities or precipitation. The composites shown below indicate that the assumptions are reasonable and agree satisfactorily in timing and structure with composites based on local indices.

3. Results

3.1. CAM3

3.1.1. Effectiveness of Sponge Region

In order to isolate the east Pacific from the effects of intraseasonal variability in the Eastern Hemisphere, a sponge region is placed in the CAM3 model to remove the primary means of equatorial communication between the hemispheres, eastward propagating Kelvin waves. To test the efficacy of the sponge region, the east Pacific warm pool is used as a reference area for lag correlation plots across the tropical belt. A 10°x10° horizontal box in the east Pacific (0° – 10°N, 110° – 100°W) is averaged for certain 30-90-day filtered variables. The box is then lag correlated with the latitudinally averaged tropical belt of a 30-90-day filtered variable. Kelvin waves originating in association with intraseasonal convection in the west Pacific propagate rapidly eastward and produce significant lag correlations across the tropics in 30-90-day upper and lower tropospheric zonal winds (figure 3.1). The 30-90-day 850-hPa zonal wind anomalies near 150°E are significantly correlated with 30-90-day 850-hPa zonal wind anomalies in the east Pacific at lags of 14 days. The degrees of freedom used to calculate the 95% significance are determined from two times the *e*-folding time scale, 80 days, of the 30-90-day 850-hPa zonal wind anomalies.

Thus, the total number of days used in the plots is divided by 80 days to obtain the conservative degrees of freedom. After crossing the east Pacific from the Eastern Hemisphere, the intraseasonal signal in 30-90-day 850-hPa wind anomalies appears to be mostly blocked by the elevated terrain in Central America consistent with previous observational studies (Matthews 2000, Yu et al. 2011). In the upper troposphere, significant correlations begin near 150°E when the east Pacific lags by 12 days and extend to 80°E when the east Pacific leads by 12 days. The region of significant correlation does not quite circumnavigate the tropics, with decreased correlations near Central America and the Indian Ocean.

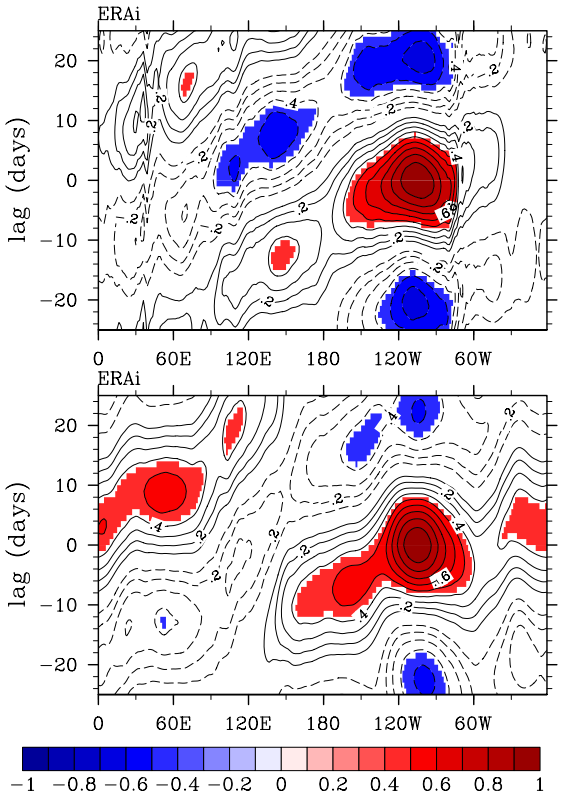

Figure 3.1 (a.) ERAi 30-90-day 850-hPa zonal wind anomalies in the east Pacific averaged from 0° – 10°N, 110° – 100°W lag correlated with 30-90-day 850-hPa zonal wind anomalies at each longitude averaged from 0° – 10°N. Values significant at the 95% threshold are shaded. **(b)** Same as (a) except 30-90-day 200-hPa zonal wind anomalies in east Pacific are correlated with averaged 5°S– 5°N 30-90-day 200-hPa zonal wind anomalies in the tropical belt.

The CAM3 model that does not contain the sponge region, known as the CAM3 control run, contains significant correlations in the western and central Pacific in 30-90-day 850-hPa zonal wind anomalies (figure 3.2). Significant correlations are also present in 30-90-day 200-hPa zonal wind anomalies in the central Pacific at comparable lags to reanalysis, as seen in figure 3.1. Intraseasonal 850-hPa zonal wind correlations are weaker and not as continuous across the Pacific Ocean basin as compared to ERAi reanalysis. Additionally, intraseasonal 200-hPa zonal wind correlations are weaker in the central Pacific and do not continue at longer leads into the Indian Ocean when compared to ERAi reanalysis. Correlations are not significant in the central and west Pacific when filtered 850-hPa zonal wind anomalies are averaged from 5°S - 5°N (plot not shown). CAM3 has several biases in the representation of intraseasonal variability. Among those include weaker intraseasonal variability in the Indian Ocean and preferred initiation of intraseasonal variability in the west Pacific. These biases can result in weaker correlations between intraseasonal zonal wind anomalies between the CAM3 control run and ERAi reanalysis over the central Pacific and Indian Oceans. Keeping such biases in mind, the relationship between the Eastern Hemisphere and east Pacific in the 30-90-day zonal wind anomaly fields used to capture Kelvin wave communication is evident in the CAM3 control model. These plots provide evidence of the ability of the CAM3 control model to capture eastward propagating 30-90 day zonal wind anomalies and significant correlations in upper and lower tropospheric zonal winds anomalies between the two hemispheres.

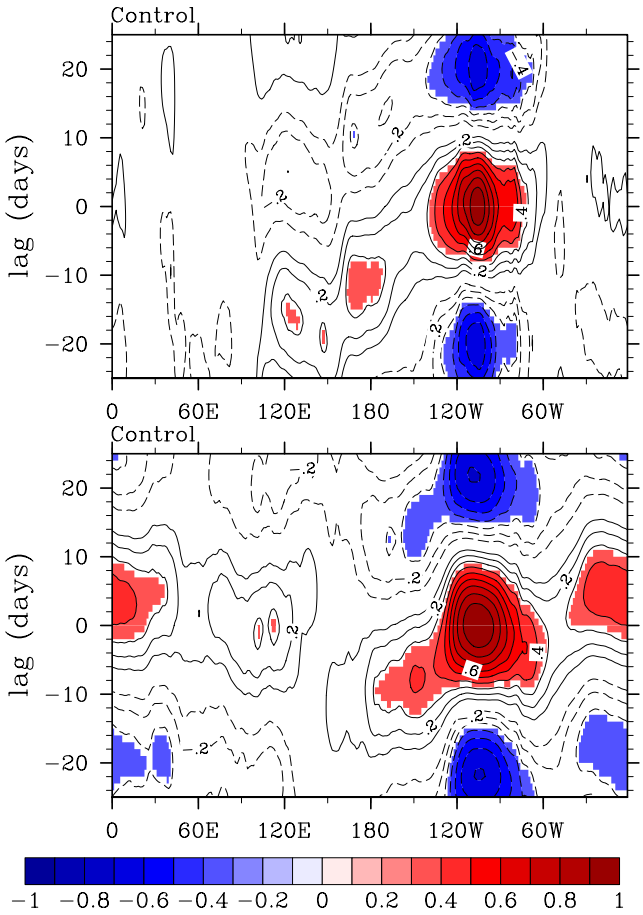

Figure 3.2 (a) Same as figure 3.1 (a) except for the CAM3 control model. **(b)** Same as figure 3.1 (b) except for the CAM3 control model.

To quantify the reduced communication between hemispheres in the CAM3 sponge model, lag correlations are used to account for possible communication mechanisms like Kelvin waves and westward propagating Rossby waves. There are no significant lag correlations between equatorial 30-90-day 850-hPa zonal wind anomalies in the east Pacific warm pool and the Eastern Hemisphere tropical belt (figure 3.3). In fact, no significant correlations exists beyond 150°W. For the 30-90-day 200-hPa zonal wind correlations, most of the significant correlations lie to the east of 125°W with the exception of a small area near 110°E at lag day 3. There are no significant correlations

between this point and the east Pacific warm pool. The significant correlation in the Eastern Hemisphere that does not show any coherent signal across the central Pacific is also within the main area of intraseasonal variability in the Eastern Hemisphere. As a result, it is possible that such a significant correlation in the main intraseasonal variability regions of the global tropical belt could be spurious. Comparing the control model (figure 3.2) and the sponge model (figure 3.3), it is clear that upper and lower tropospheric intraseasonal zonal wind signals of the sponge model that are typically associated with Kelvin wave emission from a diabatic source such as MJO convection in the Indian Ocean and west Pacific Ocean do not show clear propagating signals and are uncorrelated with the east Pacific warm pool from 120°E - 150°W. These results support the efficacy of the sponge region for removing the eastward propagating Kelvin wave pathway for communication between the west Pacific and east Pacific warm pools. Other than the Kelvin wave, no other pathways on intraseasonal timescales from the Eastern Hemisphere to the east Pacific warm pool have been found.

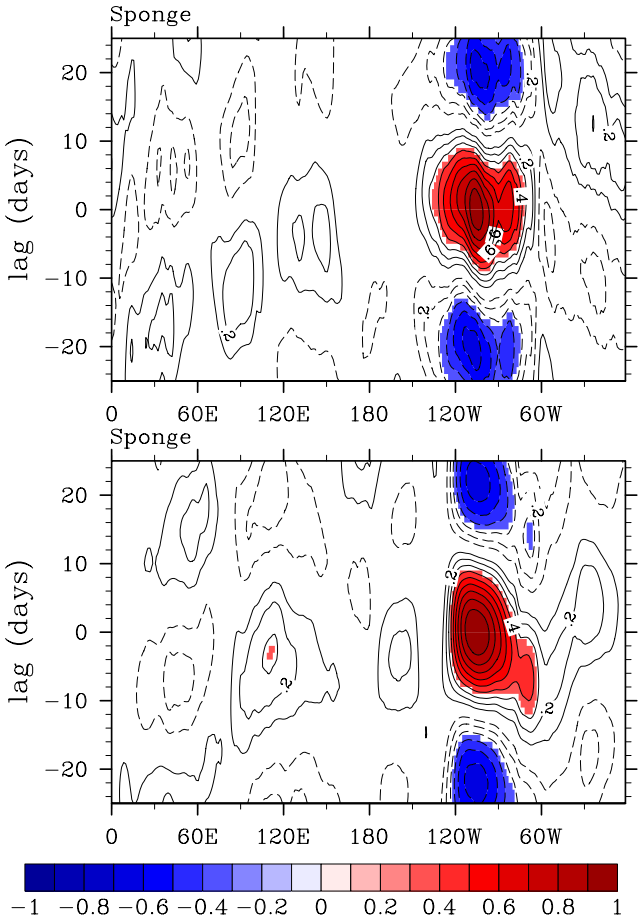

Figure 3.3 (a) Same as figures 3.1 and 3.2 (a) except for the CAM3 sponge model. **(b)** Same as figures 3.1 and 3.2 (b) except for the CAM3 sponge model.

3.1.2. Mean State

The sensitivity of the CAM3 mean state to the inclusion of a sponge region in the central Pacific Ocean is evaluated to determine the existence of any undesired feedbacks and to study the climatological background for intraseasonal variability in CAM3 with and without a sponge region. While differences in the mean state between model versions are generally small, differences in precipitation rates do exist, mainly in the intertropical convergence zone (ITCZ) band between 170°W – 160°W (figure 3.4). The sponge model has precipitation rate increases on the order of 8 mm/day in this band. Additionally,

the control model has precipitation increases of approximately 3 mm/day in the south pacific convergence zone (SPCZ) around 180°. Both of these differences are just west of or in the sponge region, which suggests some modest local changes in the climatological precipitation field between the two models are produced by the experiment design. Fundamental changes in the 850-hPa zonal and meridional wind fields do not vary much between model runs. The precipitation climatology does not appear substantially different in the rest of the tropical belt.

Both of the CAM3 models have a precipitation rate bias during boreal summer over west Pacific Ocean and Maritime Continent, featuring a strong band of mean precipitation north of the equator. This precipitation bias is consistent with other models. Models with strong representations of intraseasonal variability generally have higher mean precipitation in the South Asian summer monsoon and northwestern Pacific monsoon regions (Kim et al. 2011). The CAM3 model runs have increased precipitation and larger spatial coverage in the west Pacific between 10° – 20°N and east of 180°W. Additional high precipitation biases exist along the coast of Central America and Mexico west of the Sierra Madre Occidental and Bight of Panama. Mean precipitation in the east Pacific in the CAM3 is not as continuous from the warm pool to the coastline as in GPCP reanalysis. In the CAM3 two distinct maxima exist with one along the coastline of the Sierra Madre Occidental, and a second in the east Pacific/central Pacific. In observations, mean August precipitation gradually decreases from the east Pacific/central Pacific towards the coast. For 850-hPa

horizontal winds, the CAM3 has a larger northerly contribution than ERAi south of the ITCZ between 110° - 80°W. In the central Pacific, the CAM3 has stronger mean equatorial easterlies between 180° - 120°W (by approximately 7 m/s).

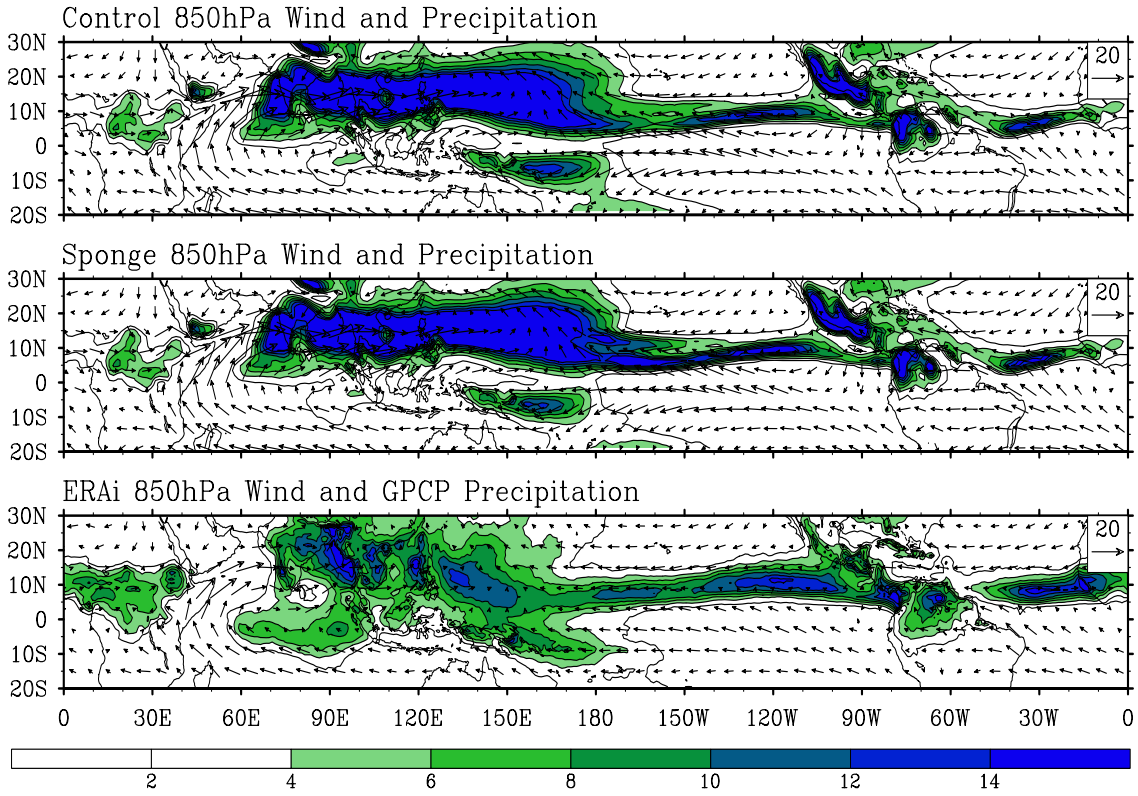

Figure 3.4 (a) The CAM control model mean 850-hPa wind vectors (m/s) and precipitation contours (mm/day) **(b)** The CAM3 sponge model. **(c)** The ERAi winds and GPCP precipitation for August (1997 – 2008)

3.1.3. Model Variability

The east Pacific warm pool is a center for intraseasonal convective and zonal wind variability that appears to be controlled by both remote and local processes. The ability of the CAM3 to simulate such intraseasonal variability comparable to observations needs to be established first before firm conclusions can be drawn from sensitivity tests. If the CAM3 control model does not have analogous intraseasonal variability to observations, then the results of the

sponge model cannot be expected to have real world implications to east Pacific intraseasonal variability.

Figure 3.5 shows the distribution of 30-90-day precipitation variance over the east Pacific for the CAM3 versions and GPCP data. Both models have comparable intraseasonal precipitation variance with no major systematic differences in the location or magnitude. The major features are the maxima in variance along 10°N from 120°W to 105°W, collocated with the climatological precipitation maximum. The CAM3 control model does have slightly higher intraseasonal variance (less than 4 mm^2/day^2) along the southwest coast of Mexico near 16°N, 100°W and extending into the climatological precipitation maximum. For the entire tropics (not shown) intraseasonal precipitation variance is very similar between the two models with no key differences in locations of variance and relatively minor changes in magnitude in the SPCZ and the central/western Pacific along 10°N.

Figure 3.6 shows the 30-90 day variance for 850-hPa zonal winds in the east Pacific for the CAM3 versions and ERAi data. For the CAM3 control model, intraseasonal variance in the 850-hPa zonal winds has two relative maxima in the east Pacific and nearby landmasses located near 12°N, 110°W and 16°N, 98°W respectively. Compared with ERAi reanalysis, the CAM3 control model has a bias towards increased intraseasonal variance in the eastern maximum along the southwest coast of Mexico. The CAM3 sponge model has 850-hPa intraseasonal zonal wind variances in approximately the same locations as the CAM3 control model although it is of slightly weaker magnitude and spread over

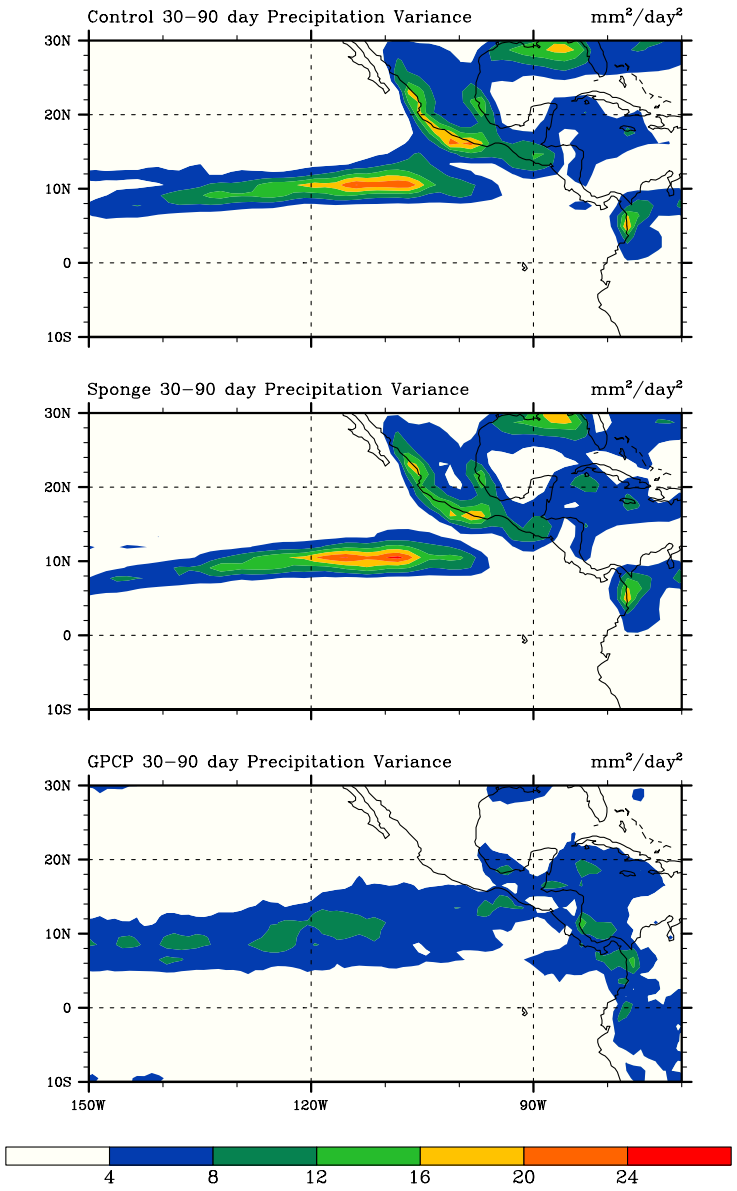

Figure 3.5 30-90-day filtered precipitation variance (mm^2/day^2) for **(a)** the CAM control model, **(b)** the CAM sponge model, and **(c)** GPCP reanalysis. The contour interval is 4 mm^2/day^2.

a smaller area. The CAM3 sponge model variance does not extend as far to the east as the control model. Over the global tropical belt (not shown), the models have comparable magnitudes of intraseasonal low-level zonal wind variance except in the equatorial western Pacific (150° - 165°E) and the equatorial longitudes of the sponge region where the sponge model has weaker magnitudes of approximately 2-3 m^2/s^2. The weaker variance in theses regions

is a likely result of the sponge model suppressing Kelvin waves in the equatorial waveguide.

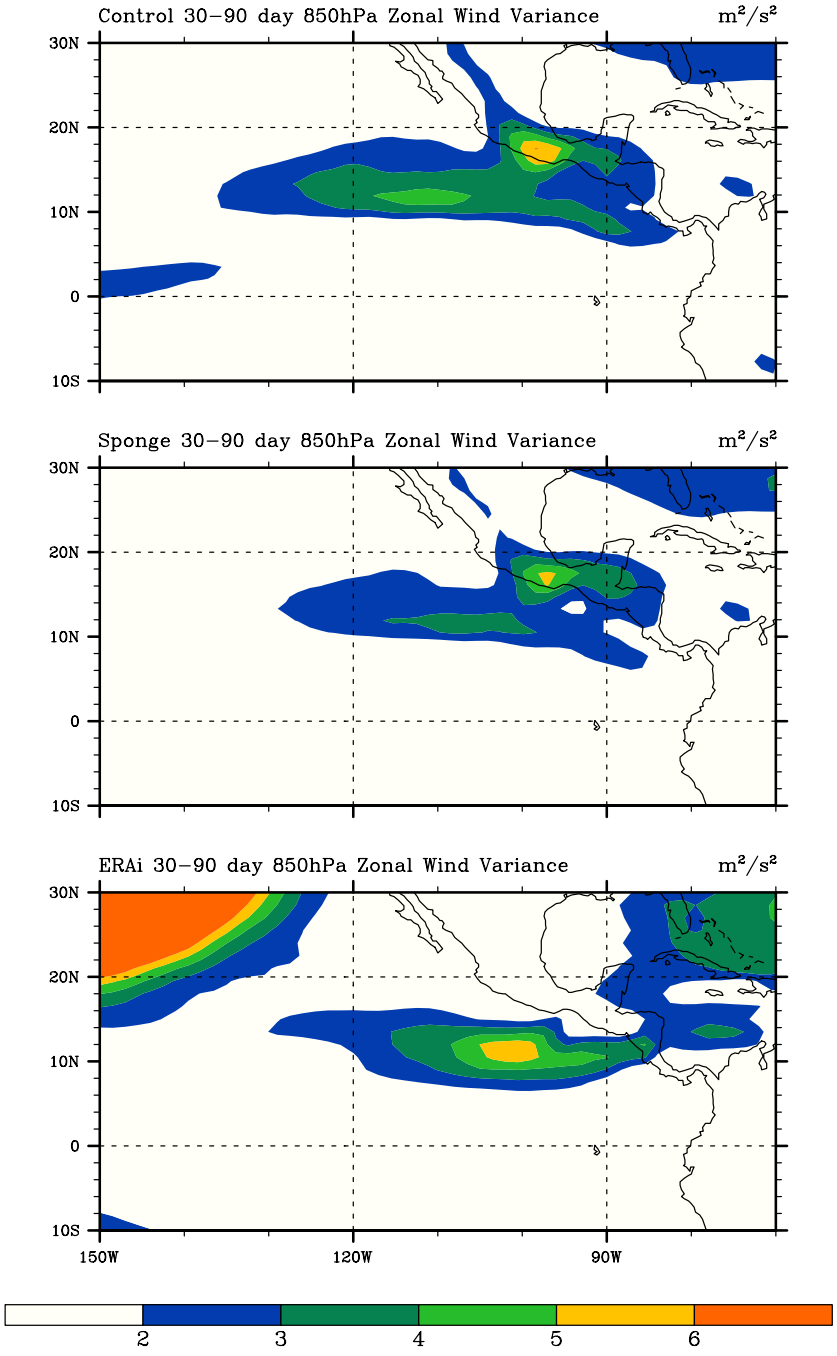

Figure 3.6 30-90-day filtered 850-hPa zonal wind variance (m^2/s^2) for **(a)** the CAM control model, **(b)** the CAM sponge model, and **(c)** ERAi reanalysis. The contour interval is 1 m^2/s^2.

Power spectra are computed for east Pacific precipitation in GPCP reanalysis data, the CAM3 control model, and the CAM3 sponge model. To compute the power spectra, the seasonal cycle is first removed from GPCP data (not necessary for CAM3 models that use perpetual August 15th conditions). Next data is averaged over a 12°x12° box in the east Pacific (coordinates shown in figures) and then subset into 180-day periods. Power spectra are computed for each 180-day period, and then the power spectra for each period are averaged together to produce a composite spectrum. Significance for the 95% and 5% upper and lower bounds are calculated. In figure 3.7, significant intraseasonal power exists for all datasets, but for the CAM3 sponge experiment, intraseasonal power occurs at a shorter 35-day period compared to the observational 50-day period. CAM3 model versions are more sensitive to the averaging box position than GPCP with considerably less intraseasonal power to the east and west (plots not shown).

Power spectra are also calculated for 850-hPa zonal winds for the CAM3 model versions and ERAi reanalysis (figure 3.8). The CAM3 control model and ERAi have significant intraseasonal power at comparable 50-day periods in the east Pacific. The CAM3 sponge model does not have significant intraseasonal power over the east Pacific no matter the center coordinates of the averaging box. Additionally, ERAi data has increasing intraseasonal power toward the equator at 140°W longitude while the power in the CAM3 control model gradually decreases to the north and south (plots not shown).

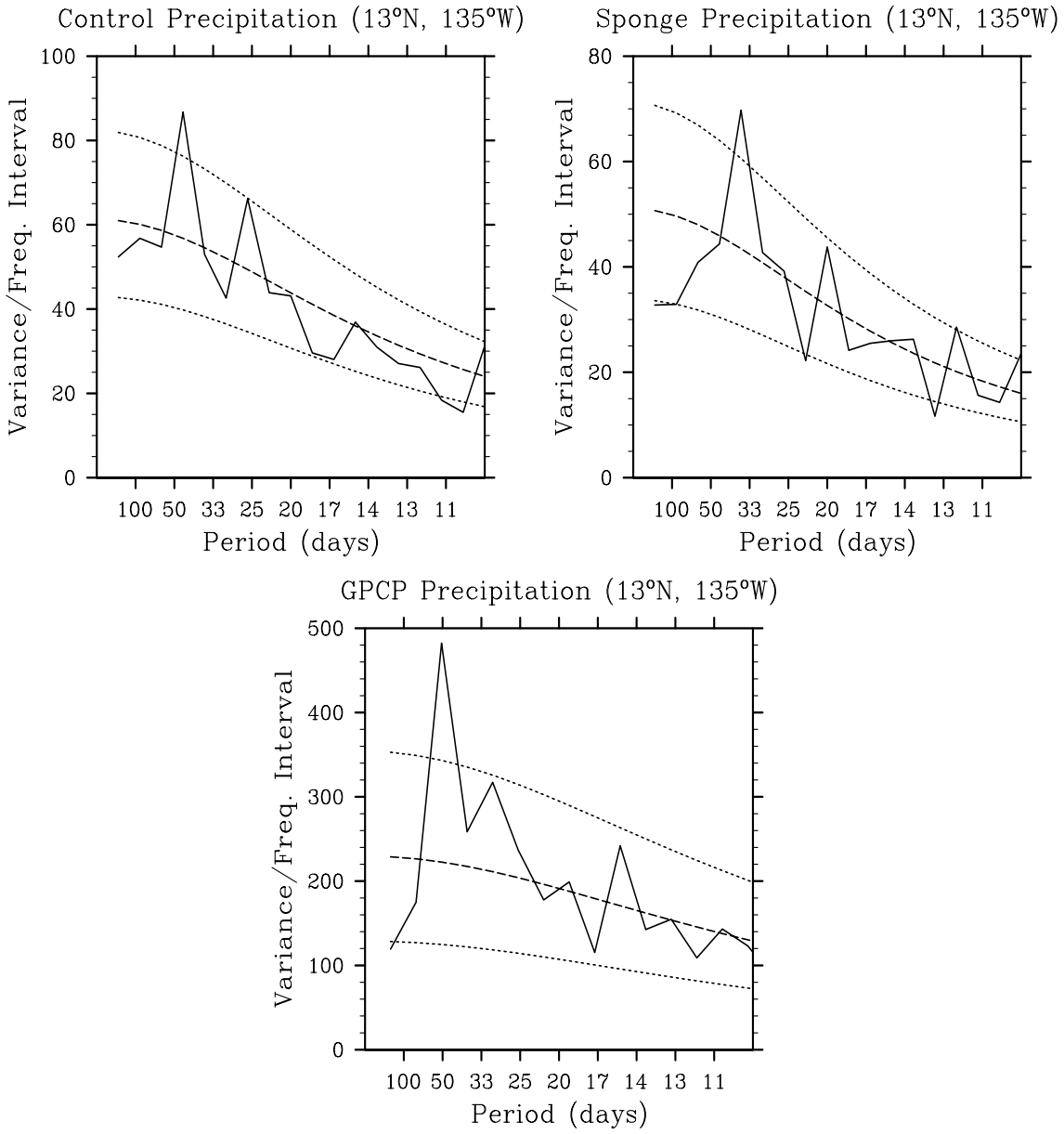

Figure 3.7 Power Spectrum for **(a)** the CAM3 control model **(b)** the CAM3 sponge model and **(c)** summer season (June – October) GPCP reanalysis. Values are averaged over a 12°x12° box centered on the shown latitude and longitude. Dashed line is red noise spectrum and dotted lines are the upper and lower 95% and 5% upper and lower bounds, respectively.

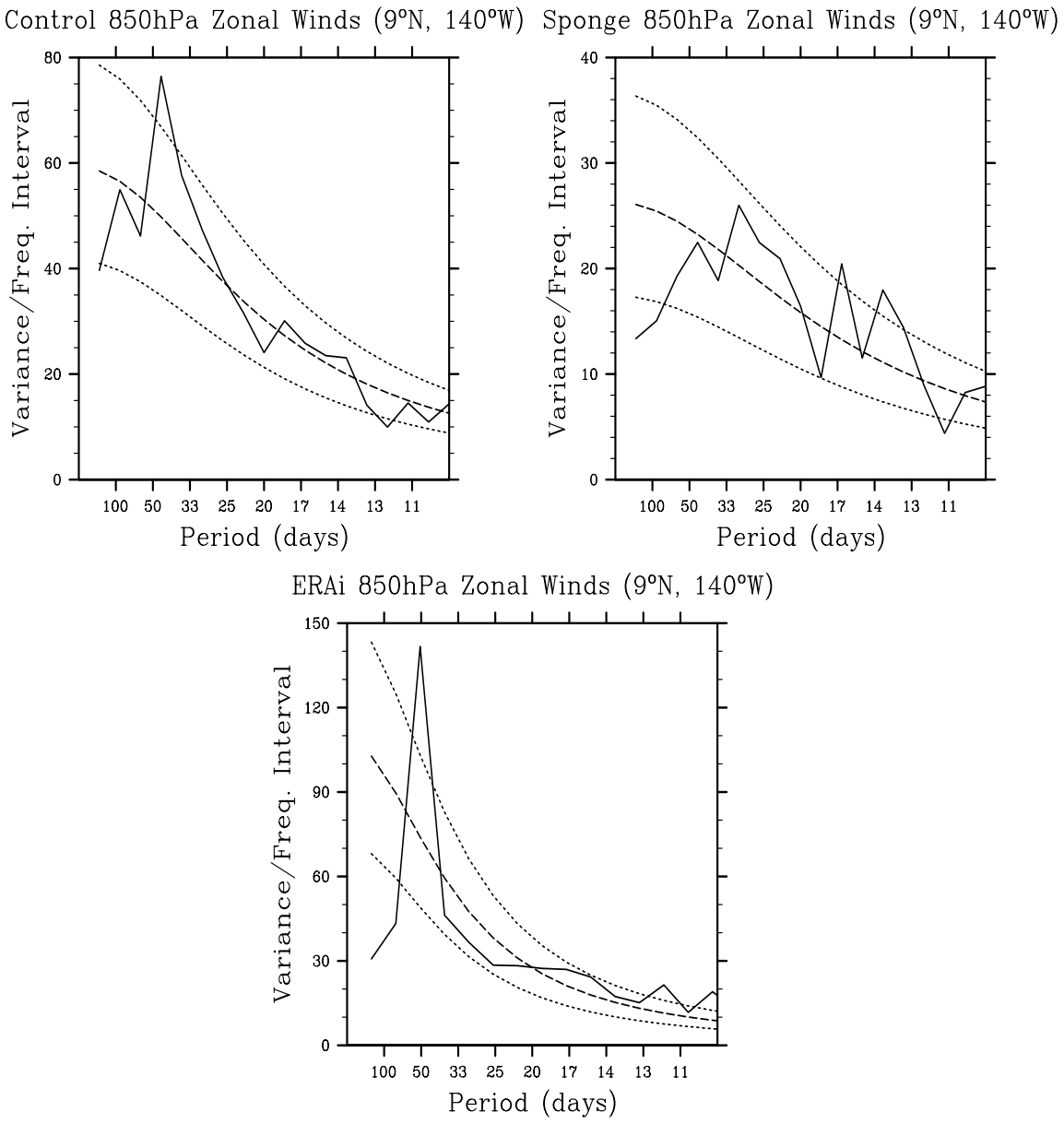

Figure 3.8 Power Spectrum for **(a)** the CAM3 control model **(b)** the CAM3 sponge model and **(c)** summer season (June-October) ERAi reanalysis. Values are averaged over a 12°x12° box centered on the shown latitude and longitude. Dashed line is red noise spectrum and dotted lines are the upper and lower 95% and 5% upper and lower bounds, respectively

3.1.4. Composites

Given the amount of intraseasonal variability shown in the east Pacific warm pool for both CAM3 model versions, it is useful to show the evolution of intraseasonal events in composite fields. Composites derived from the first two

combined EOFs of 30-90 day filtered 850-hPa zonal winds, 200-hPa zonal winds, and precipitation around the global tropical belt (15°S - 15°N) are shown in figures 1.1, 3.10, and 3.12 for ERAi and GPCP reanalysis, CAM3 control model, and CAM3 sponge model, respectively. Figures 3.9, 3.11, and 3.13 show the same composites only zoomed for the east Pacific. In figure 1.1 for observations, phase 1 displays strong 30-90-day precipitation anomalies in the Indian Ocean with a low level wind response similar to that of the Gill model. Strong 30-90-day 850-hPa westerly wind anomalies extend through the Indian Ocean to the west of the positive 30-90-day precipitation anomalies, and opposite signed intraseasonal wind anomalies reside to the east extending into the central Pacific and impinging on the east pacific, consistent with a Kelvin wave response. The off-equatorial 30-90-day wind anomalies to the west of the positive equatorial diabatic heating are consistent with the Rossby gyre structure of the Gill model. In figure 3.9, negative 30-90-day precipitation anomalies start to form in the east Pacific during the beginning of an MJO event in Phase 1. The center of east pacific anomalies moves slightly eastward by phase 2. Phase 2 has stronger negative 30-90-day precipitation anomalies in the east Pacific and the Kelvin wave response has shifted eastward to extend strong 30-90-day easterly anomalies across the central and east Pacific from 0° - 15°N.

Beginning in Phase 3, suppressed 30-90-day precipitation anomalies occur in the equatorial Indian Ocean with strong westerly anomalies persisting though the northern Indian Ocean and across the Maritime Continent. In the east Pacific, intraseasonal convection has a dipole structure with positive anomalies

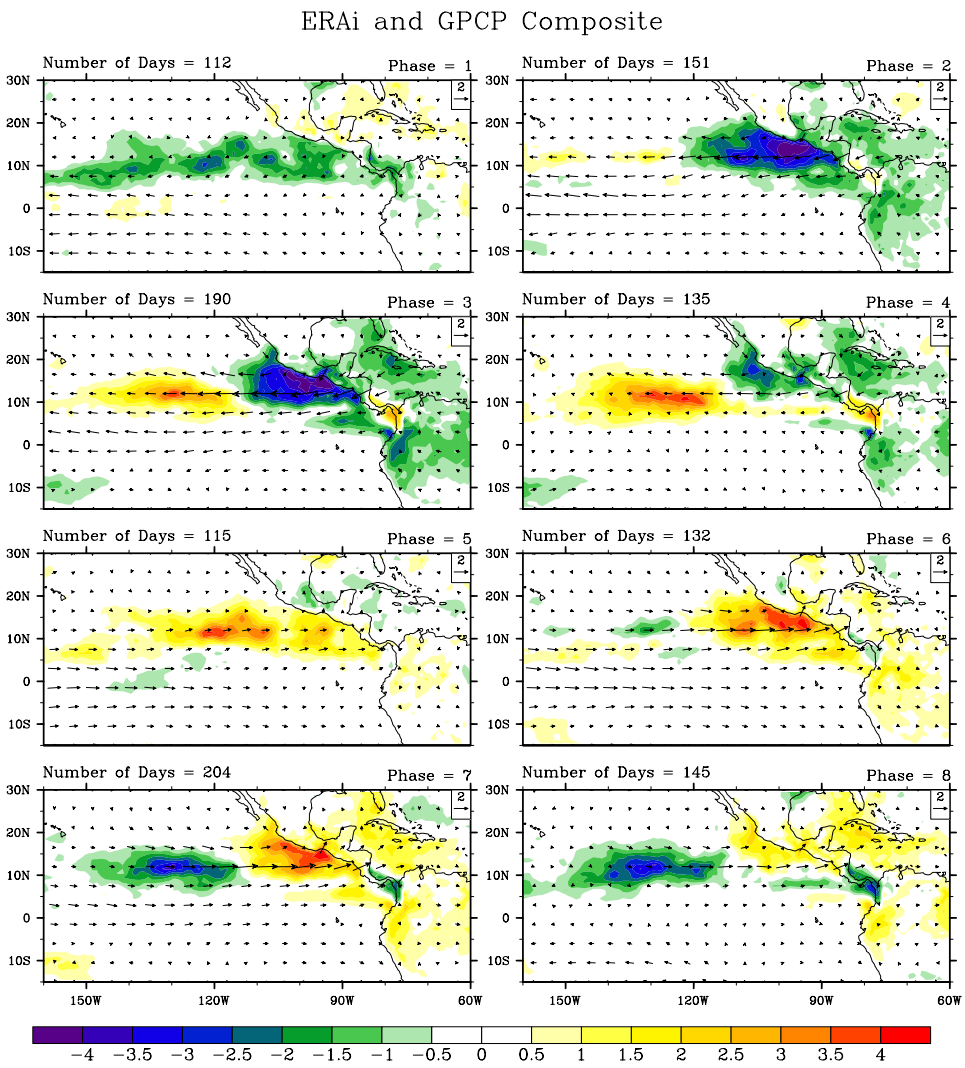

Figure 3.9 ERAi and GPCP composite of 30-90-day 850-hPa horizontal wind anomalies (m/s, vectors) and 30-90-day precipitation anomalies (mm/day, contours) zoomed in for east Pacific.

from 10° - 15°N, 150° - 120°W. As noted by Maloney and Esbensen (2007), 120°W is approximately where mean surface winds in the east Pacific change sign from westerlies (to the east) to easterlies (to the west). The precipitation anomaly rapidly changes sign just to the east of 120°W and persists to the coast of Mexico. Anomalies of both signs are approximately 3-4 mm/day in magnitude and occur in easterly wind anomalies, although the positive 30-90-day precipitation anomaly is positioned in slightly weaker easterly anomalies. During

phase 4 the negative precipitation anomaly in the Indian Ocean increases in magnitude and spatial coverage to the north with 850-hPa westerly anomalies situated from the Indian Ocean to the central Pacific Ocean along the equator. Easterly anomalies in the east Pacific are weakened and the negative precipitation anomalies east of 120°W have eroded to the north with no significant changes to the east Pacific precipitation anomalies west of 120°W.

Phase 5 has strong negative precipitation anomalies in the central and eastern Indian Ocean and across much of the Maritime continent. Easterly anomalies cover much of the equatorial central Indian Ocean and westerly anomalies extend across much of the Pacific Ocean, impinging on the east Pacific warm pool. Positive precipitation anomalies that were west of 120°W in phase 4 do not extend as far westward and precipitation anomalies to the east of 120°W have become positive. In phase 6, negative precipitation anomalies stretch from the Indian Ocean across the Bay of Bengal and Maritime Continent into the west Pacific along with easterly anomalies across much of the same area. Westerly anomalies have completely established themselves in the central and east Pacific Ocean. Weakly negative precipitation anomalies are located over a small area near 12°N just to the west of 120°W. Positive precipitation anomalies are located east of 120°W near 14°N along with strong westerly anomalies north of 5°N. During phases 7 and 8 the negative precipitation anomalies associated with the suppressed phase of the MJO in the Eastern Hemisphere are mainly located in the west Pacific Ocean as positive precipitation anomalies grow in the west and central Indian Ocean. Westerly wind anomalies

are confined mainly to the east Pacific with the dipole structure in precipitation persisting across 120°W. In phase 8 the dipole precipitation structure has weakened along with the westerly anomalies in the east Pacific as precipitation in the Indian Ocean intensifies to complete the cycle.

In figure 3.10 the composite structure of an MJO event is shown for the CAM3 control model. Compared to observations, the control model composites have similar phase developments in 30-90-day precipitation and 850-hPa horizontal wind anomalies. A notable difference is the location of positive 30-90-day precipitation anomalies in the initial phases. The CAM3 control model has precipitation anomalies beginning in the west Pacific Ocean as opposed to the Indian Ocean in the reanalysis composite. Throughout the progression of the MJO event, the control model has weaker intraseasonal precipitation anomalies of both signs in the Indian Ocean, Maritime Continent, west Pacific Ocean, and east Pacific Ocean.

The phase development of the 30-90-day 850-hPa horizontal wind anomalies is comparable between the control model and reanalysis across the tropical belt, although the phase relationship of precipitation with the wind anomalies in the Eastern Hemisphere is not necessarily consistent between the two. In the east Pacific similar but weaker development of the dipole in precipitation anomalies occur (figure 3.11). Also the sign of precipitation anomalies and direction of zonal wind anomalies are in agreement with reanalysis. When winds are anomalously westerly, precipitation anomalies to the east of 120°W are generally enhanced, as in observations. These comparable

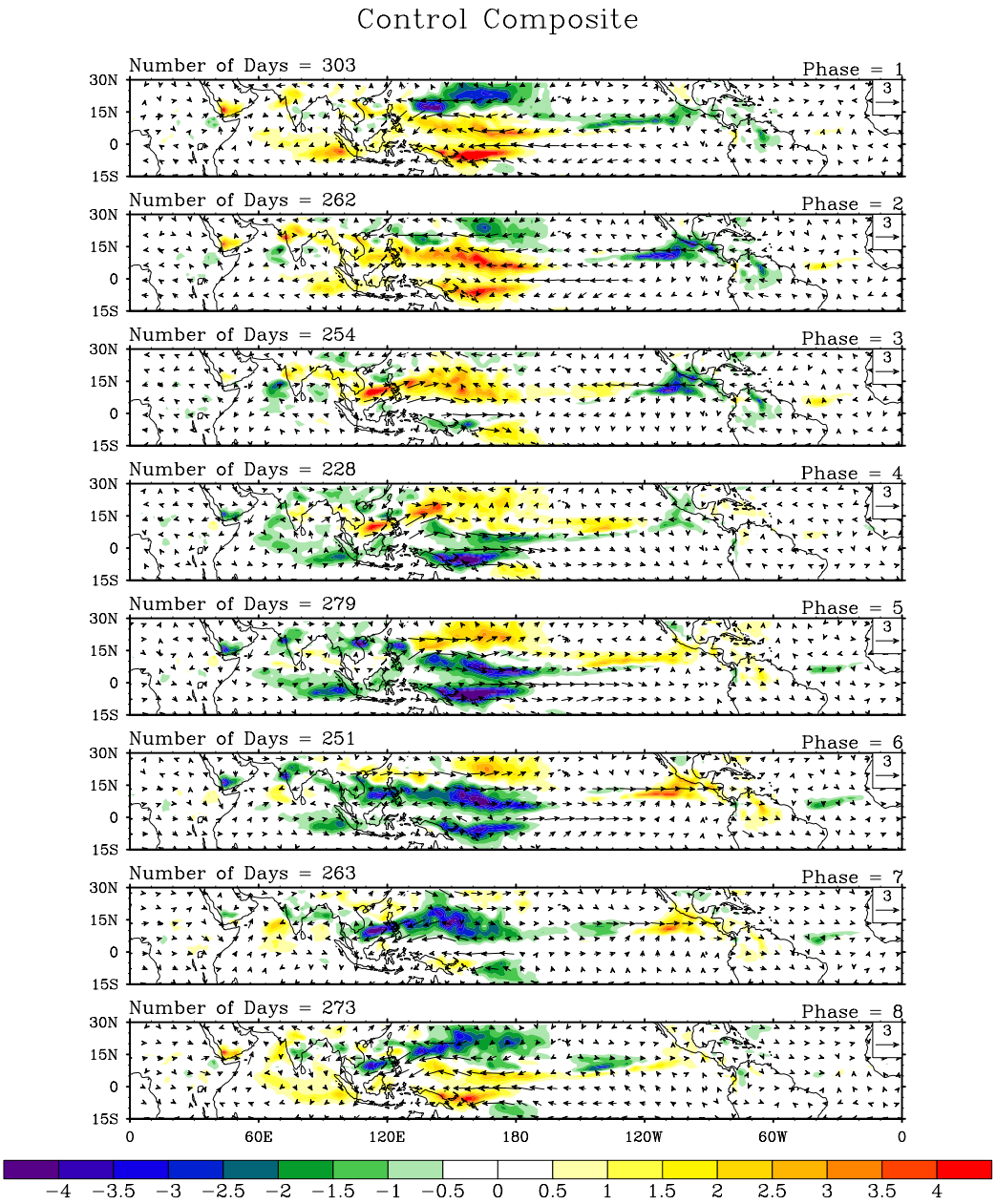

Figure 3.10 The CAM3 control model composite of 30-90-day 850-hPa horizontal wind anomalies (m/s, vectors) and 30-90-day precipitation anomalies (mm/day, contours).

evolutions of MJO events between the reanalysis and CAM3 control model gives confidence that the model is capturing the development of MJO events and the related propagation across the tropical belt, particularly in the east Pacific Ocean.

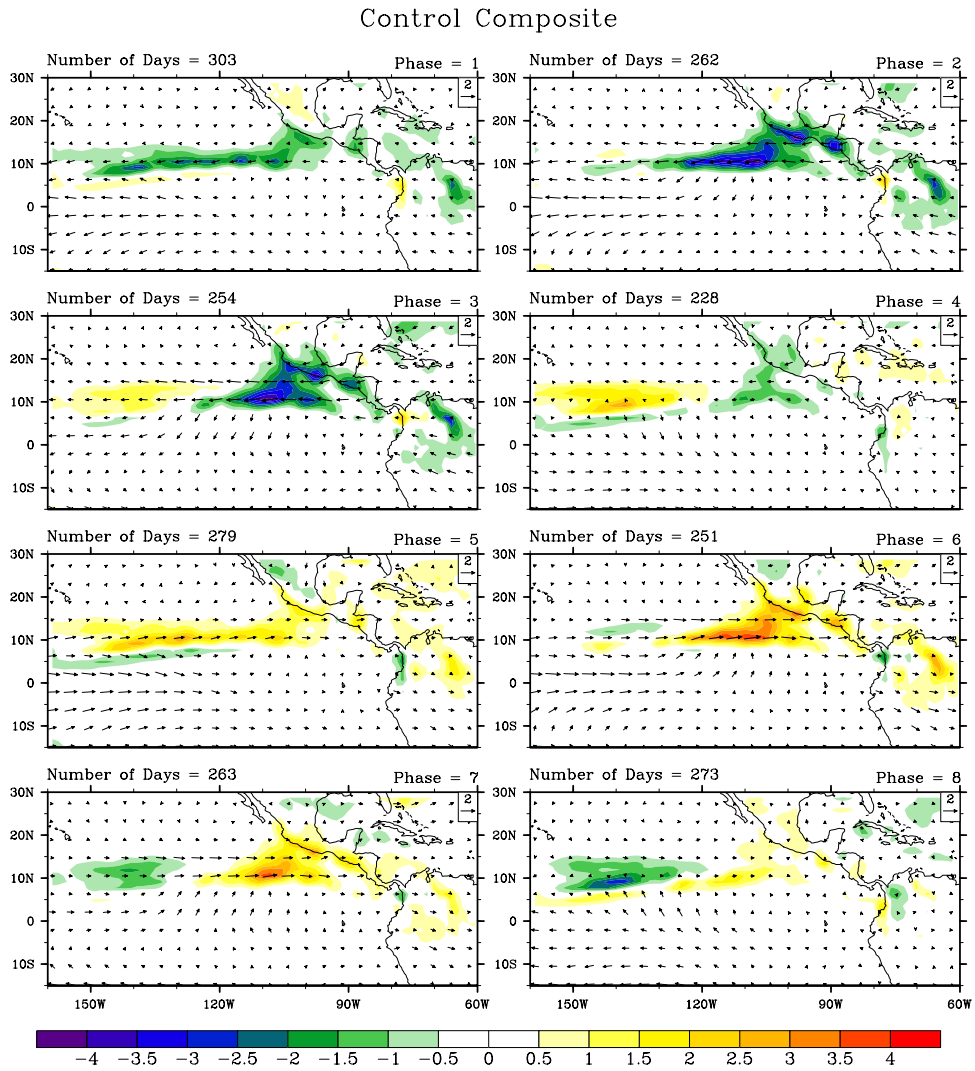

Figure 3.11 The CAM3 control model composite of 30-90-day 850-hPa horizontal wind anomalies (m/s, vectors) and 30-90-day precipitation anomalies (mm/day, contours) zoomed in for east Pacific.

The composite MJO evolution in the CAM3 sponge model is shown in Figure 3.12. The sponge model composite does not have large 850-hPa horizontal wind anomalies east of 180° at any phase. The evolution of the wind anomalies in the Eastern Hemisphere of the sponge model composite is qualitatively similar to those of the control model; the phase of precipitation anomalies with respect to the wind anomalies varies. Coherent propagation of

precipitation anomalies is difficult to discern in the sponge model composite. Additionally the sponge model appears to have less coherent large-scale circulation responses to convection in the Eastern Hemisphere. In the east Pacific weak amplitude intraseasonal precipitation anomalies do not display any dipole structure or smooth phase transitions, at least when keyed to strong intraseasonal events (figure 3.13). Moreover, in the east Pacific for most phases the precipitation anomalies are of opposite sign than the reanalysis and control model composites, indicating that east Pacific intraseasonal variability does not project well onto the global EOFs used for the MJO composite. In summary, the composite plots derived from the sponge model combined EOFs show less coherent propagation of MJOs across hemispheres and weak intraseasonal variance in the east Pacific that does not have the same phase relations with the Eastern Hemisphere as the reanalysis and CAM3 control model composites. However, it should be noted that this does not necessarily preclude strong intraseasonal variability in the east Pacific that is independent of global MJO evolution.

Even if east Pacific variability that is coherent with the MJO is not produced, local intraseasonal variability can still exist, as suggested by the significant spectral peak in figure 3.7 (b). Multivariate EOF analysis is used in Figures 3.14 and 3.16 to determine if systematic differences exist in the structure of 30-90-day variability between the CAM3 control and sponge model in the east Pacific. Multivariate EOF analysis is performed on 30-90-day precipitation and 850-hPa zonal wind anomalies. Multivariate EOF analysis can account for the

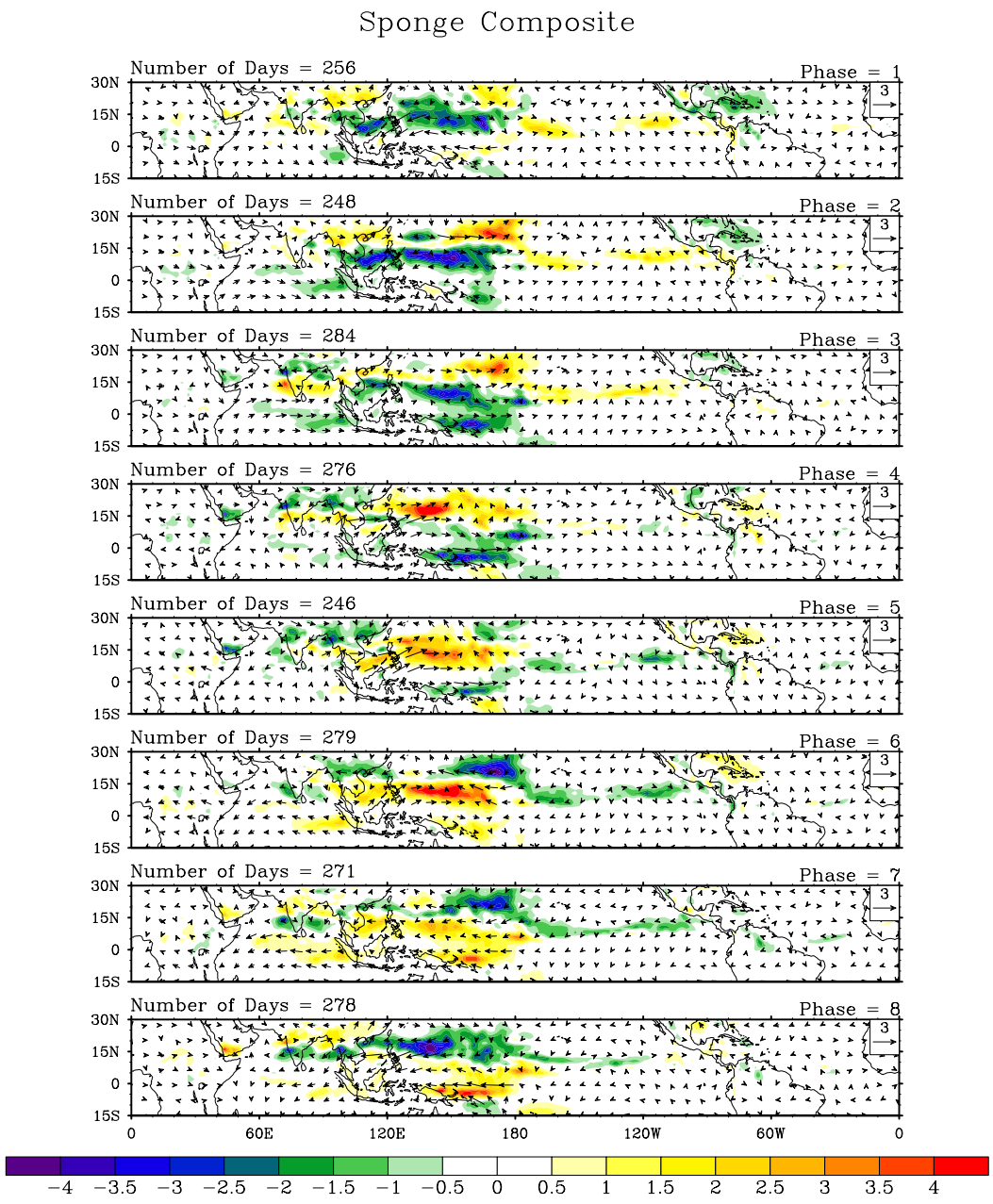

Figure 3.12 The CAM3 sponge model composite of 30-90-day 850-hPa horizontal wind anomalies (m/s, vectors) and 30-90-day precipitation anomalies (mm/day, contours).

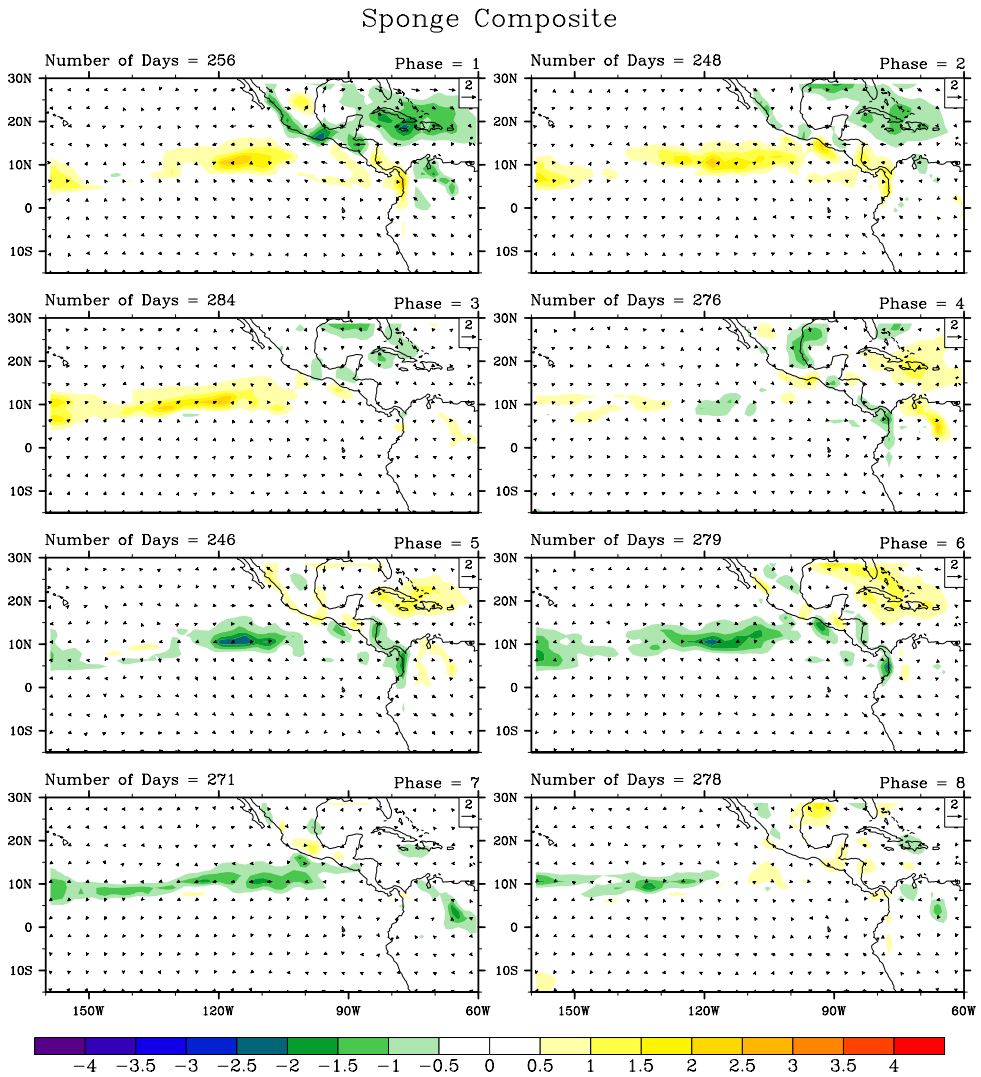

Figure 3.13 The CAM3 sponge model composite of 30-90-day 850-hPa horizontal wind anomalies (m/s, vectors) and 30-90-day precipitation anomalies (mm/day, contours) zoomed in for east Pacific.

coupled covariability of two anomaly fields in a single EOF. So that the amplitudes of the two different variables are comparable when put into the multivariate EOF analysis, the data for each field is first normalized individually. Also, the variables are weighted by cosine of latitude. In the control model, the first two multivariate EOFs shown in figure 3.14 explain 25.7% and 10.5% of the intraseasonal variance over the shown domain, respectively. The third and fourth EOFs explain 8.5% and 4.6% of the intraseasonal variance, respectively.

For the sponge model, the first two multivariate EOFs shown in figure 3.15 explain 19.8% and 9.0% of the intraseasonal variance over the same domain as figure 3.14. The third and fourth EOFs of the sponge model explain 7.6% and 6.4% of the intraseasonal variance, respectively. The EOF pairs in figures 3.14 and 3.15 show very similar features for 850-hPa zonal wind (color contours) and precipitation (black outlined contours) suggesting that the east Pacific modes of intraseasonal variability look similar between the two models. Only the first EOFs of the CAM3 control and sponge models are significantly different according to the criterion of North et al. (1982). The first EOFs in both models shows westerly anomalies corresponding to the dipole pattern of precipitation anomalies. In the first EOF of the CAM3 control model, a strong signal in the 850-hPa zonal wind colored contours near the equatorial western boundary is present, presumably as a result of the eastward propagating Kelvin wave. The first EOF of the CAM3 sponge model does not have an equatorial maximum in the 850-hPa zonal wind colored contours that extends to the western boundary.

Because intraseasonal variability in the sponge model has similar leading modes of variability to the control model, but does not appear to project well onto the global MJO composites (figures 3.12 and 3.13), a composite based on local east Pacific indices should better represent intraseasonal variability there. The local index is based on the first principal component of 30-90-day 850-hPa zonal wind anomalies and 30-90-day precipitation anomalies. Intraseasonal events are chosen and averages are composited based on lag days from the peak amplitude of the event. For the CAM3 control model in figure 3.16, a similar

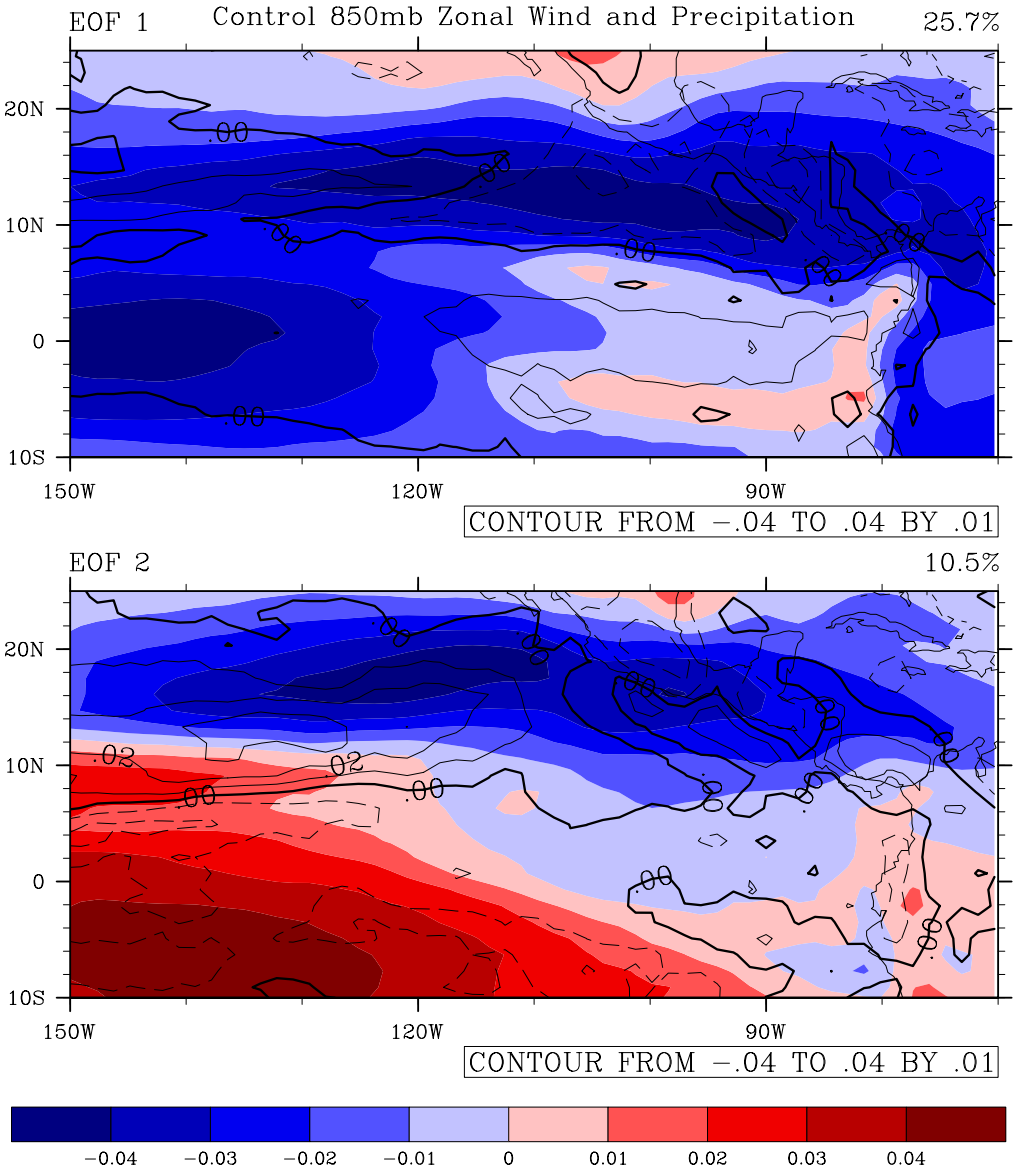

Figure 3.14 Multivariate EOF analysis of the CAM3 control model 30-90 day filtered precipitation (line contour) and 850-hPa zonal wind anomalies (color contours) over the shown domain. The contour interval for precipitation is from -.04 to .04 by .01 with the heavy black line indicating the 0 contour. The shading interval for 850-hPa zonal wind anomalies is from -.05 to .05 by .01.

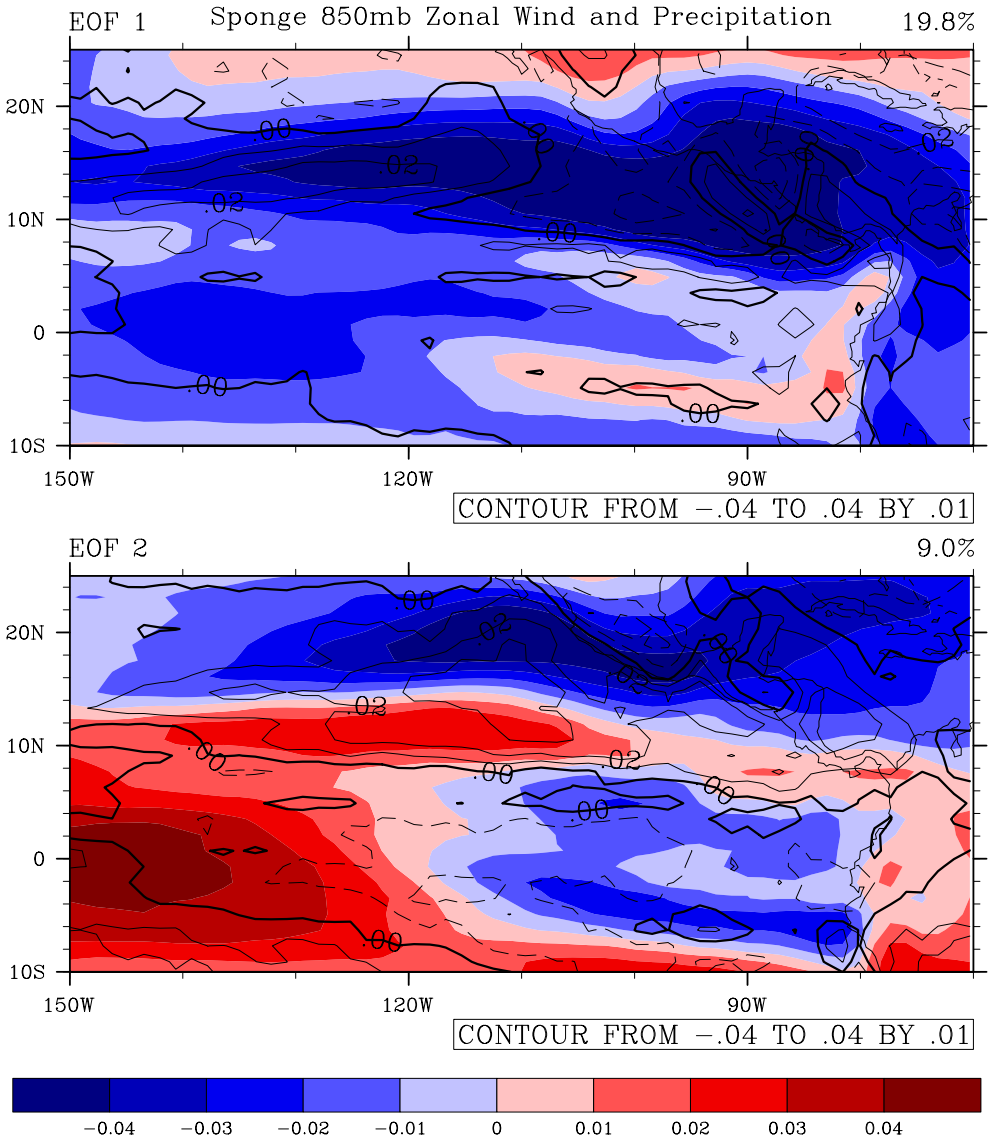

Figure 3.15 Multivariate EOF analysis of the CAM3 sponge model 30-90 day filtered precipitation and 850-hPa zonal wind anomalies over the shown domain. Contour and shading intervals are the same as the CAM3 control model multivariate EOFs.

progression of 30-90-day precipitation and 850-hPa horizontal wind anomalies is seen in the local composite and global composite. Composites based on the local index have larger magnitudes in the east Pacific than those based on the global index. During the easterly phase (lags -20 and -15), positive precipitation anomalies are located to the west of 120°W with negative precipitation anomalies immediately to the east. As the easterly phase weakens, the dipole structure

becomes less coherent. Westerly anomalies increase by lag -5, and positive precipitation anomalies are present in the ITCZ band. At lag 0 a dipole structure in precipitation anomalies of opposite sign to lag -20 occurs and is located in strong westerly wind anomalies. As the westerly phase weakens, the dipole structure in precipitation gradually erodes in lags 5, 10, and 15. The westerly phase can be seen propagating into the domain from the equatorial west beginning at lag -10 and more notably at lag -5, consistent with the global composite before a westerly phase in the east Pacific. The equatorial 30-90-day westerly anomalies seen in lags -5, 0, and 5 rapidly weaken to the east of 120°W.

For the CAM3 sponge model local composite shown in figure 3.17, the evolution and structure of an east Pacific intraseasonal event is very similar to that of the CAM3 control model local and global composites. The dipole structure in precipitation at lags -20 and -15 is present during the easterly phase and has the same sign as in the control model. Unlike the control model, the westerly phase is slower to develop, and does not have as great of a westward extension out of the main precipitation region, and does not have as strong of positive precipitation anomalies east of 120°W. Similar to the control model, the dipole structure in precipitation anomalies gradually erodes as the easterly and westerly phases weaken. The results of the sponge model in the local composite suggest that intraseasonal variability in the east Pacific is of the same form as that of the control model. The differences in global and local composites of the

sponge model suggest intraseasonal variability in the east Pacific is paced by that in the Eastern Hemisphere, but can exist in isolation in the same form.

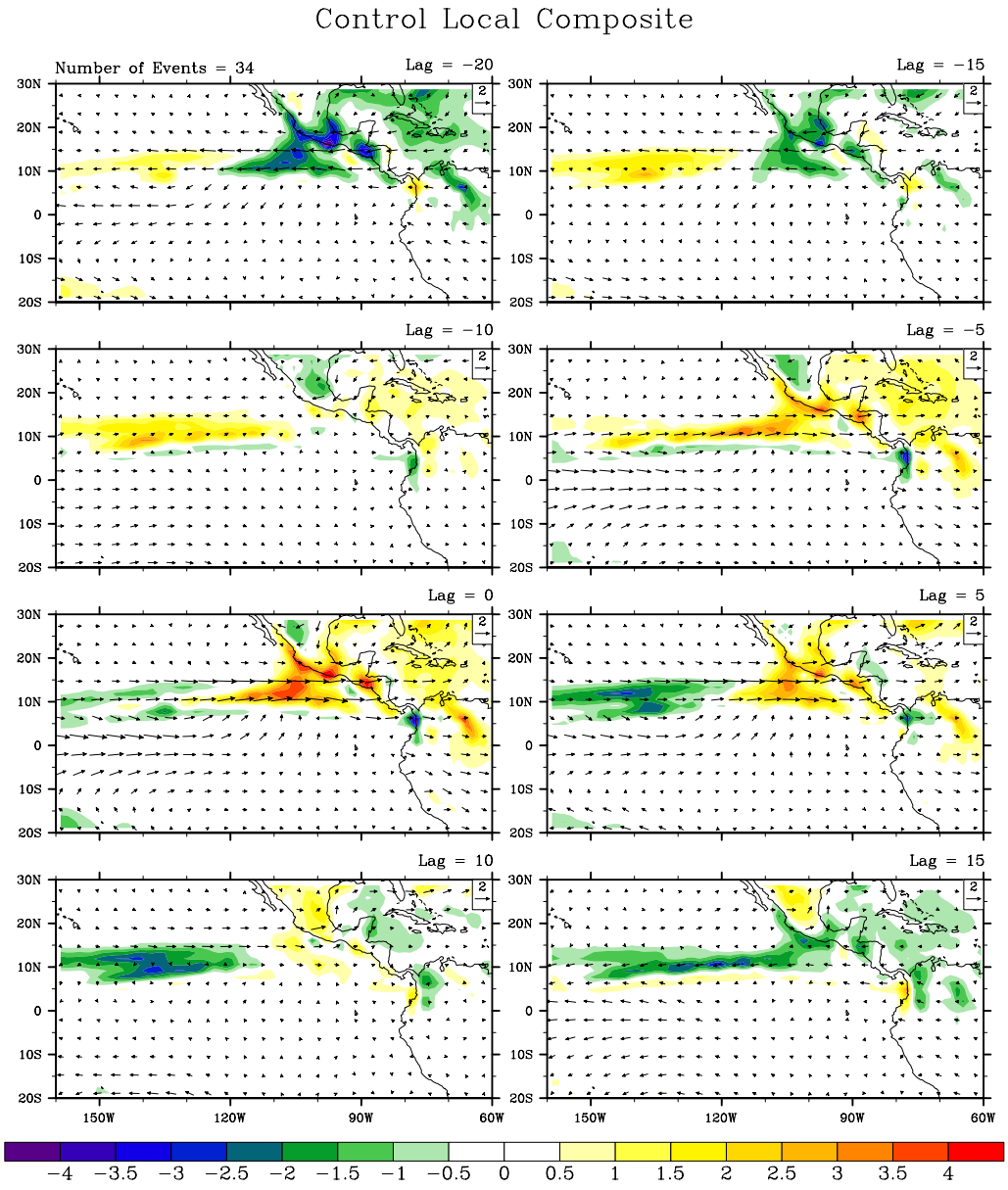

Figure 3.16 Local composite of 30-90-day precipitation (mm/day, contours) and 850-hPa wind anomalies (m/s, vectors) for the CAM3 control model.

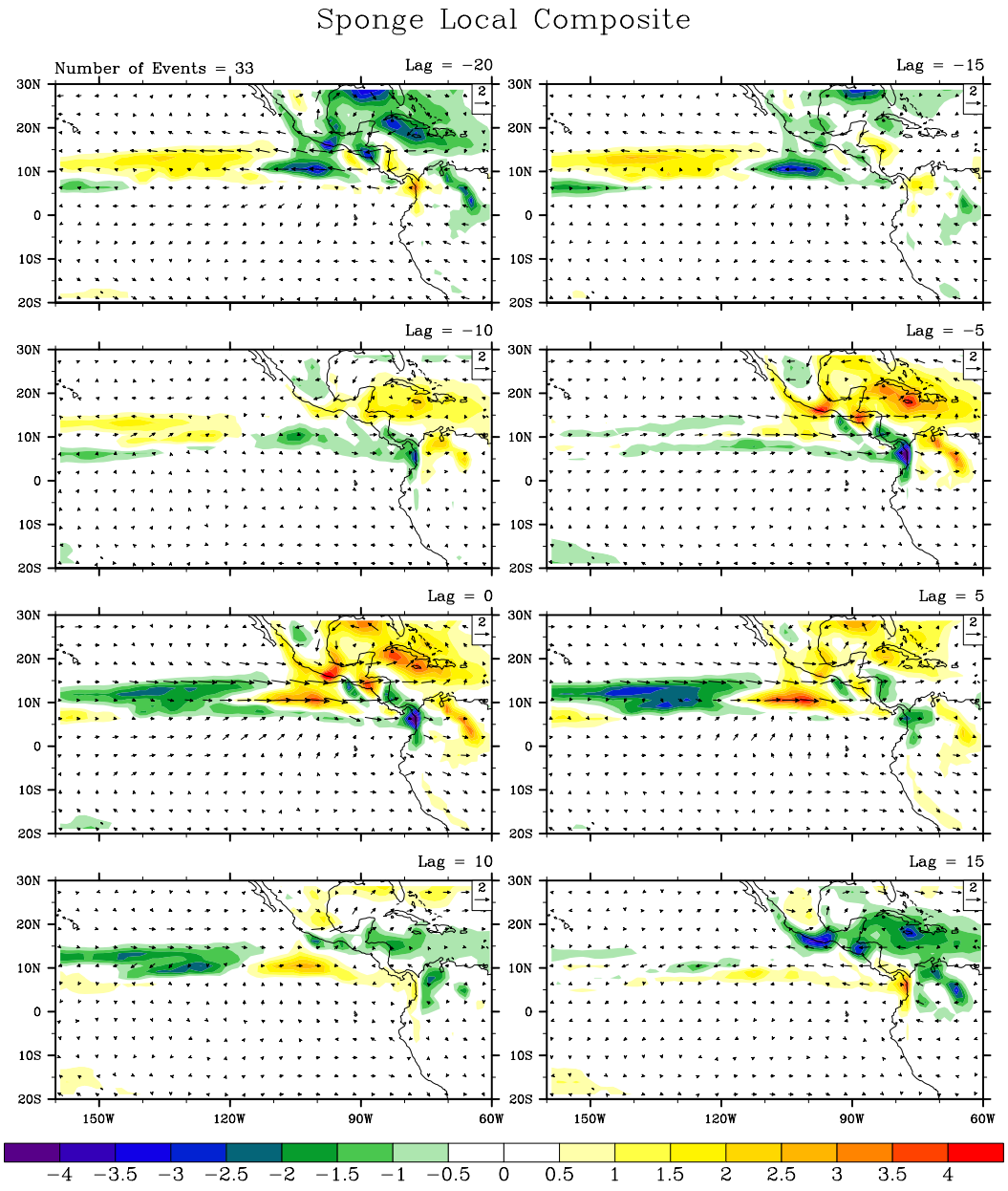

Figure 3.17 Local composite of 30-90-day precipitation (mm/day, contours) and 850-hPa wind anomalies (m/s, vectors) for the CAM3 sponge model.

3.1.5. Possible Mechanisms

To briefly explore some possible mechanisms by which the CAM3 sponge model produces local intraseasonal variability without influences from global MJO signals, composite fields of relevant variables are generated based on the same

local index as figure 3.17. Focus is placed on those variables that can strongly influence the moisture field and thus moist static energy to regulate east Pacific convection. Figure 3.18 shows composite 30-90-day latent heat flux anomalies for the CAM3 control model. Figure 3.20 shows the same for the CAM3 sponge model. In general both plots show suppressed intraseasonal latent heat flux anomalies in the east Pacific during easterly phases and enhanced latent heat flux anomalies during westerly phases, consistent with Maloney and Esbensen (2003) and Maloney and Esbensen (2007), suggesting that surface flux anomalies support convection. The 30-90-day westerly anomalies constructively add to the mean summer wind field in the east Pacific to enhance westerly flow and latent heat fluxes east of 120°W (Maloney and Kiehl 2002). Latent heat fluxes in the east Pacific east of 120°W intensify in conjunction with increased 30-90-day westerly and precipitation anomalies (figure 3.16).

The 30-90-day 1000-hPa convergence anomalies are shown in figure 3.19 for the CAM3 control model. In the east Pacific along the Mexican coast, surface convergence anomalies are in phase with precipitation anomalies (figure 3.16). In the observational analysis of east Pacific intraseasonal events in Maloney and Hartmann (1998), surface convergence leads precipitation by approximately 5 days. In the CAM3 control model surface convergence anomalies do not appear to lead precipitation. Surface convergence anomalies gradually increases beginning at lag -5 around 15°N, 100°W with increasing 30-90-day precipitation anomalies. Surface convergence could be a possible mechanism for the initiation of convection due to the Ekman convergence that occurs on the

northeastward flank of the dry Kelvin wave as it propagates into the east Pacific (Maloney and Esbensen 2007, Xie et al. 2009, Small et al. 2010). Additionally, these intensifications of both 30-90-day latent heat flux and surface convergence anomalies are consistent with diabatic heating intensifying the low-level circulation and thus latent heat flux and surface convergence anomalies possibly intensifying the diabatic heating to cause more precipitation (Maloney and Esbensen 2003).

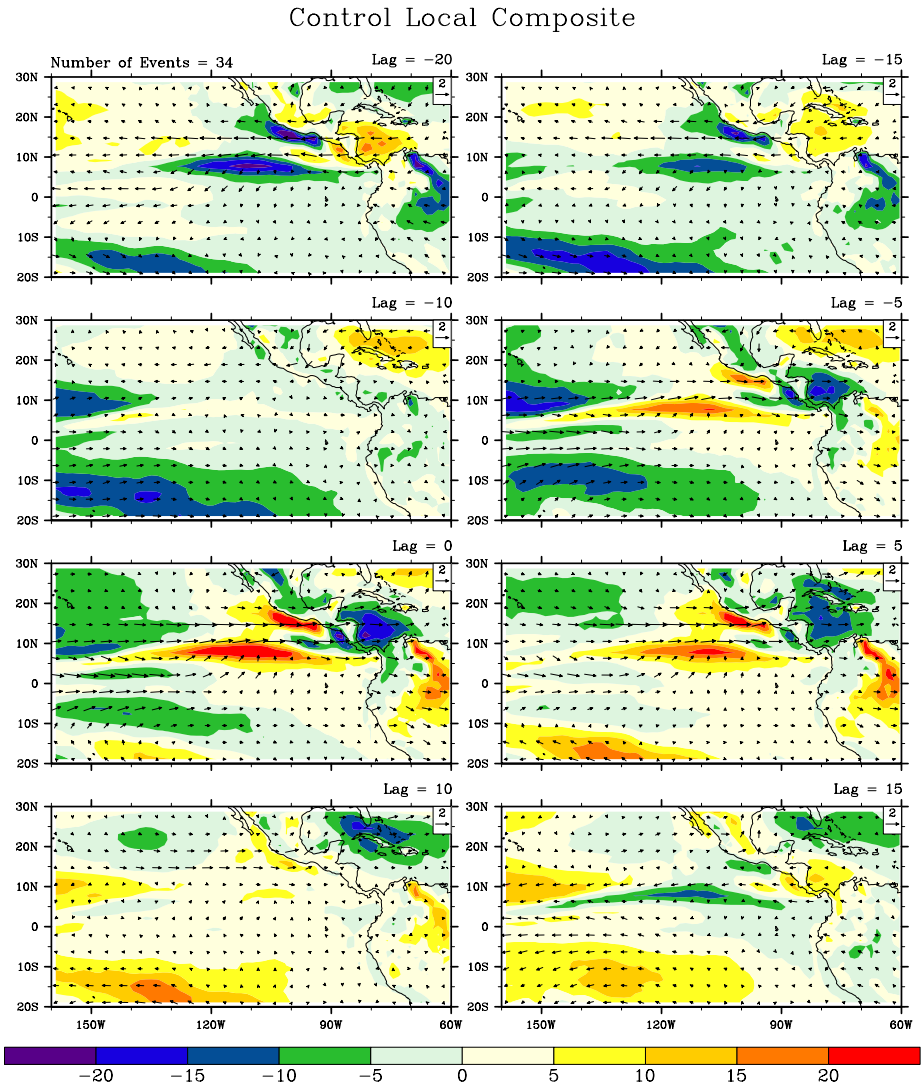

Figure 3.18 Local composite of 30-90-day latent heat flux (W/m^2, contours) and 850-hPa wind anomalies (m/s, vectors) for the CAM3 control model.

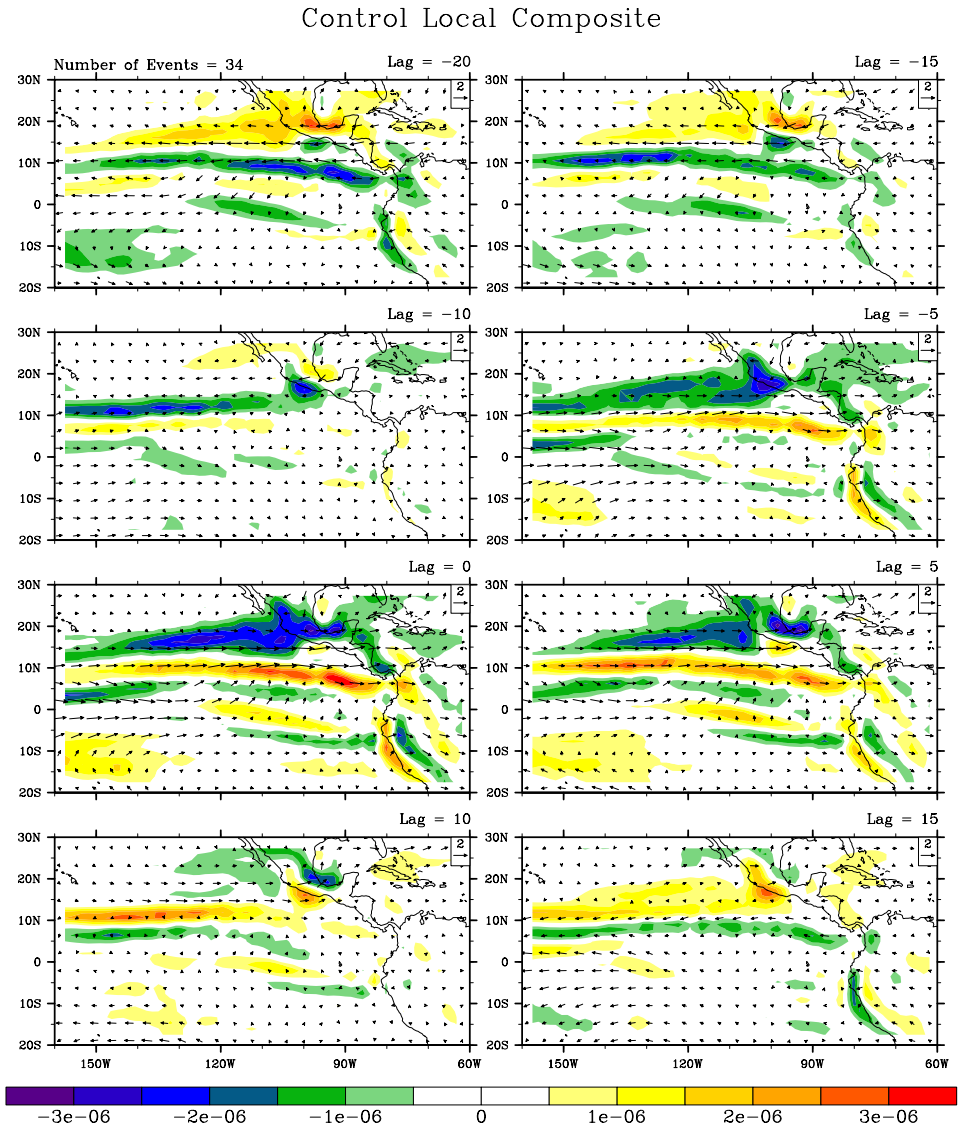

Figure 3.19 Local composite of 30-90-day 1000-hPa divergence (s^{-1}, contours) and 850-hPa wind anomalies (m/s, vectors) for the CAM3 control model.

In the CAM3 sponge model, 30-90-day composite latent heat flux anomalies based on the local index show very similar locations and intensity changes with increasing lags as for the control model (figure 3.20). The sponge model has stronger 30-90-day latent heat flux anomalies in the Caribbean Sea and Gulf of Mexico associated with stronger 30-90-day low-level wind anomalies in these regions. The 30-90-day latent heat flux anomalies in the sponge model

generally do not extend as far west as in the control model for most phases. Because the control model includes Kelvin wave signals that propagate into the domain from the west, the eastward propagating zonal wind signal could contribute to the westward extension of the latent heat flux maxima and minima. Most importantly, the CAM3 sponge model shows strong similarity to the control model in the evolution of the latent heat flux anomalies in the east Pacific with very similar locations and magnitudes of maxima and minima.

The 30-90-day 1000-hPa surface convergence anomalies for the CAM3 sponge model (figure 3.21) show comparable spatial structure and evolution to those of the CAM3 control model. Both models have similar convergence anomalies in the east Pacific warm pool that begin to increase at lag -5 for the westerly phase. During easterly phases, the warm pool region has weak intraseasonal divergence anomalies at 1000-hPa in both model versions. Although the sponge model cannot support the possible mechanism of surface convergence on the northern flank of a Kelvin wave propagating from the west Pacific, similar diabatic and low-level circulation feedbacks are possible as in the control model. Similar to some of the observational conclusions of Maloney and Esbensen (2003), the importance of a wind induced surface heat exchange mechanism (Emanuel 1987, Neelin and Held 1987) cannot be ruled out in supporting boreal summer intraseasonal convection in the east Pacific, nor can the importance of the rotational flow to inducing latent heat fluxes to the south and west of convection (Raymond 2001).

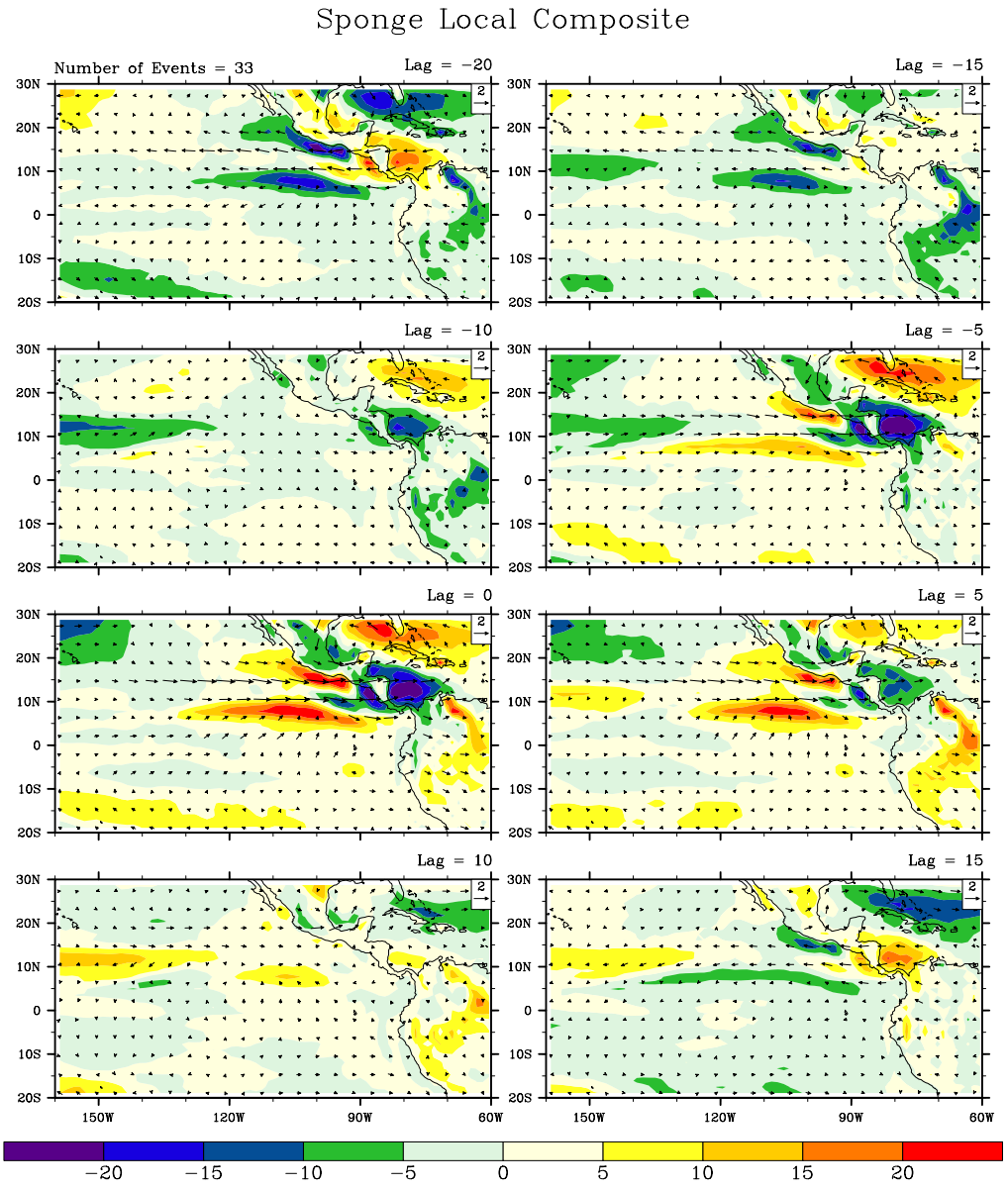

Figure 3.20 Local composite of 30-90-day latent heat flux anomalies (W/m^2, contours) and 850-hPa wind anomalies (m/s, vectors) for the CAM3 sponge model.

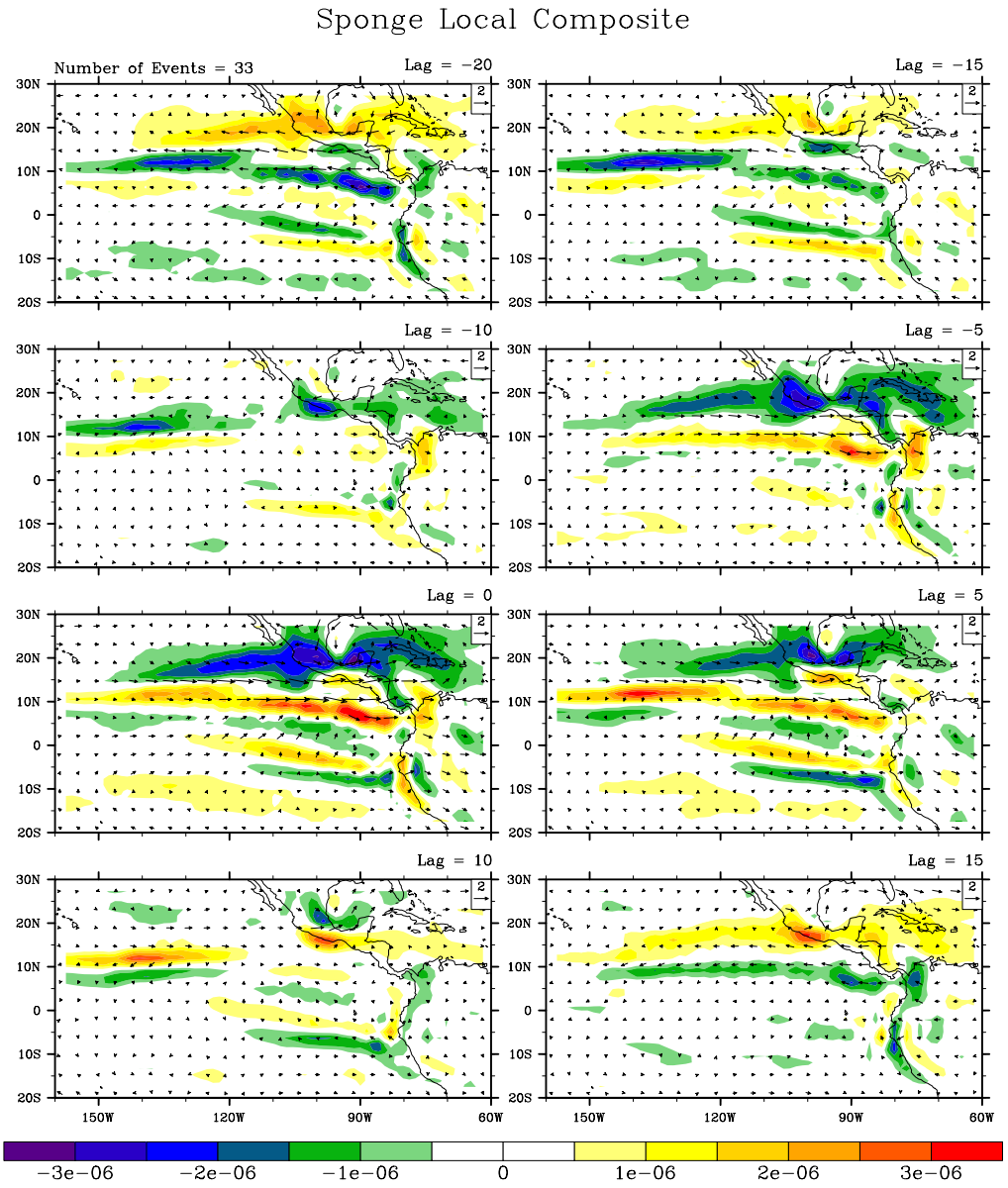

Figure 3.21 Local composite of 30-90-day 1000-hPa divergence anomalies (s^{-1}, contours) and 850-hPa wind anomalies (m/s, vectors) for the CAM3 sponge model.

The CAM3 model versions propose that significant and independent intraseasonal precipitation anomalies can exist without MJO influence in the east Pacific. The independent east Pacific intraseasonal variability in the CAM3 sponge model is of similar form to that of the CAM3 control model, as seen in the EOF and local composite analyses. Coherent signals in 30-90-day wind-driven

flux and near surface convergence anomalies suggest roles for both in east Pacific intraseasonal events. These results propose that the east Pacific perhaps has independent intraseasonal oscillations that are easily tuned to the Eastern Hemisphere through rapid eastward Kelvin wave propagation. Although it appears the MJO enhances intraseasonal variability in the east Pacific, the MJO is not necessary to initiate or maintain east Pacific intraseasonal events in the CAM3. In a separate experiment, CAM3 sensitivity tests using climatological surface fluxes significantly reduced intraseasonal precipitation anomalies in the Eastern Hemisphere. However, dynamical signals were still able to propagate into the east Pacific. Thus, the NO-WISHE experiments did not successfully isolate the east Pacific from the Eastern Hemisphere on intraseasonal timescales.

3.2. IRAM

3.2.1. Effectiveness of Filtered Boundary Conditions

To quantify the effectiveness of the IRAM boundary filtering in removing intraseasonal signals propagating into the domain from any direction, it is useful to correlate intraseasonal variability between the IRAM control model and IRAM filter model (name given to model with filtered boundary conditions). Because the boundaries are forced with the same conditions between the two models except for the removal of the intraseasonal signal in the IRAM filter model, there should be limited correlation between the two models in the intraseasonal band for winds and precipitation. In figure 3.22 cross correlations at zero time lag for

30-90-day 850-hPa zonal wind anomalies between the IRAM control and filter model are shown. The null hypothesis used for this figure is that the two datasets are independent and correlation coefficients that exceed the 95% significance level reject the null hypothesis. Weak but statistically significant positive cross correlations are found in the east Pacific, but most are located outside of the region of main intraseasonal variability. The cross correlations at zero time lag for intraseasonal precipitation anomalies are weaker and less coherent than the 850-hPa zonal wind anomalies (not shown). Additionally, the IRAM multivariate EOFs of 30-90-day precipitation and 850-hPa zonal wind anomalies shown later (figures 3.30 and 3.31) expand on the differences in intraseasonal variability between the IRAM versions. The first EOF of the IRAM filter model explains less than a third of the intraseasonal variance explained by the IRAM control model. Based on the absence of significant cross correlation values in the main region of intraseasonal variability, the weak coherence of significant values outside the region, and the strong differences in EOFs discussed later, the filter appears to be effectively removing intraseasonal signals from all boundaries. Examination of fields at other vertical levels also confirms this.

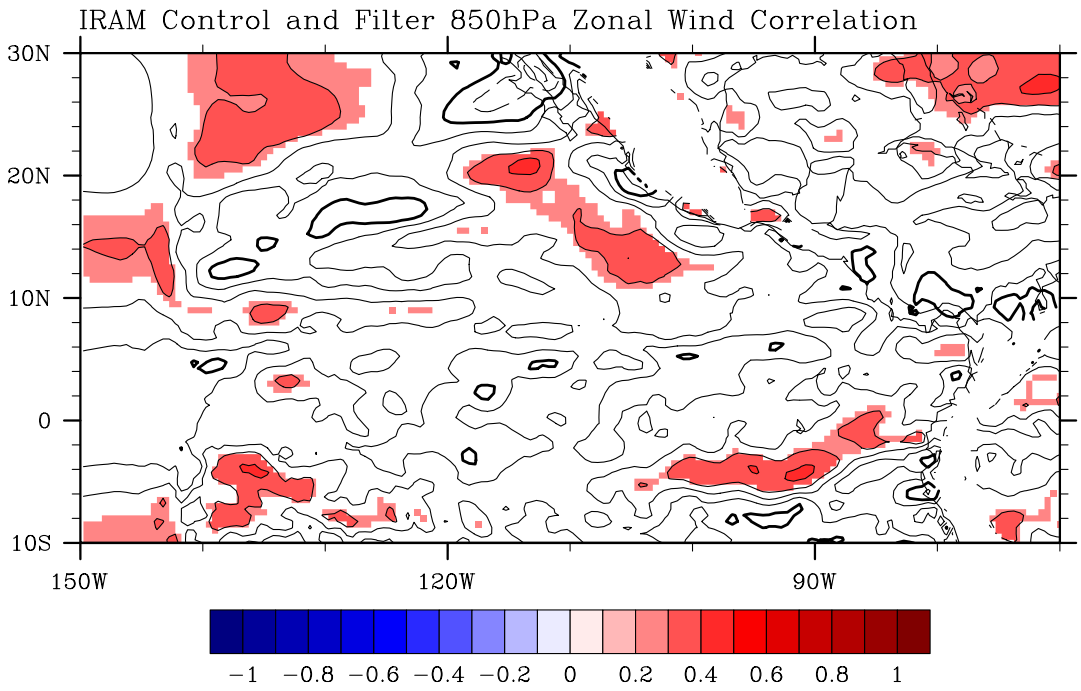

Figure 3.22 Cross correlation at lag 0 for 30-90-day 850hPa zonal wind anomalies between the IRAM control and filter models. Values that reject the null hypothesis at the 95% significance threshold are shaded. The thick black line is the zero contour and negative contours are dashed.

3.2.2. Mean State

Summer season (June – October) averages of 1000-hPa horizontal winds and precipitation are shown in Figure 3.23. Both IRAM models have very comparable summer climatologies with no fundamental differences between the mean winds or precipitation. The inclusion of intraseasonal filters at the boundaries has not systematically changed the summer mean state of the IRAM. When compared with NCEP 1000-hPa horizontal winds, IRAM has weak but easterly winds along 10°N east of 120°W in the east Pacific. NCEP winds are also weak but westerly along the same latitude band during boreal summer. The mean low-level background flow has been shown to be important to a general circulation model's representation of intraseasonal variability (Inness et al. 2003;

Inness and Slingo 2003). In the fully coupled model used in the study of Small et al. (2010), there are mean westerlies in the June – October east Pacific warm pool climatology that agree with observations. Outside of this region, the winds also agree well with observations. The IRAM has larger amounts of precipitation than observations on the order of ~6-10 mm/day extending west of 120°W along the ITCZ. Small et al. (2010) noted that mean IRAM precipitation is about 1.5 times greater than observations and may be related to higher wind speed and evaporation/latent heat fluxes in the IRAM (Xie et al. 2007). In the east Pacific, the IRAM maximum mean summer precipitation is located over a broad area near 145°W while GPCP has its maximum mean summer precipitation near 105°W that slowly dampens to the west. Aside from the magnitude differences, ITCZ locations agree with GPCP reanalysis.

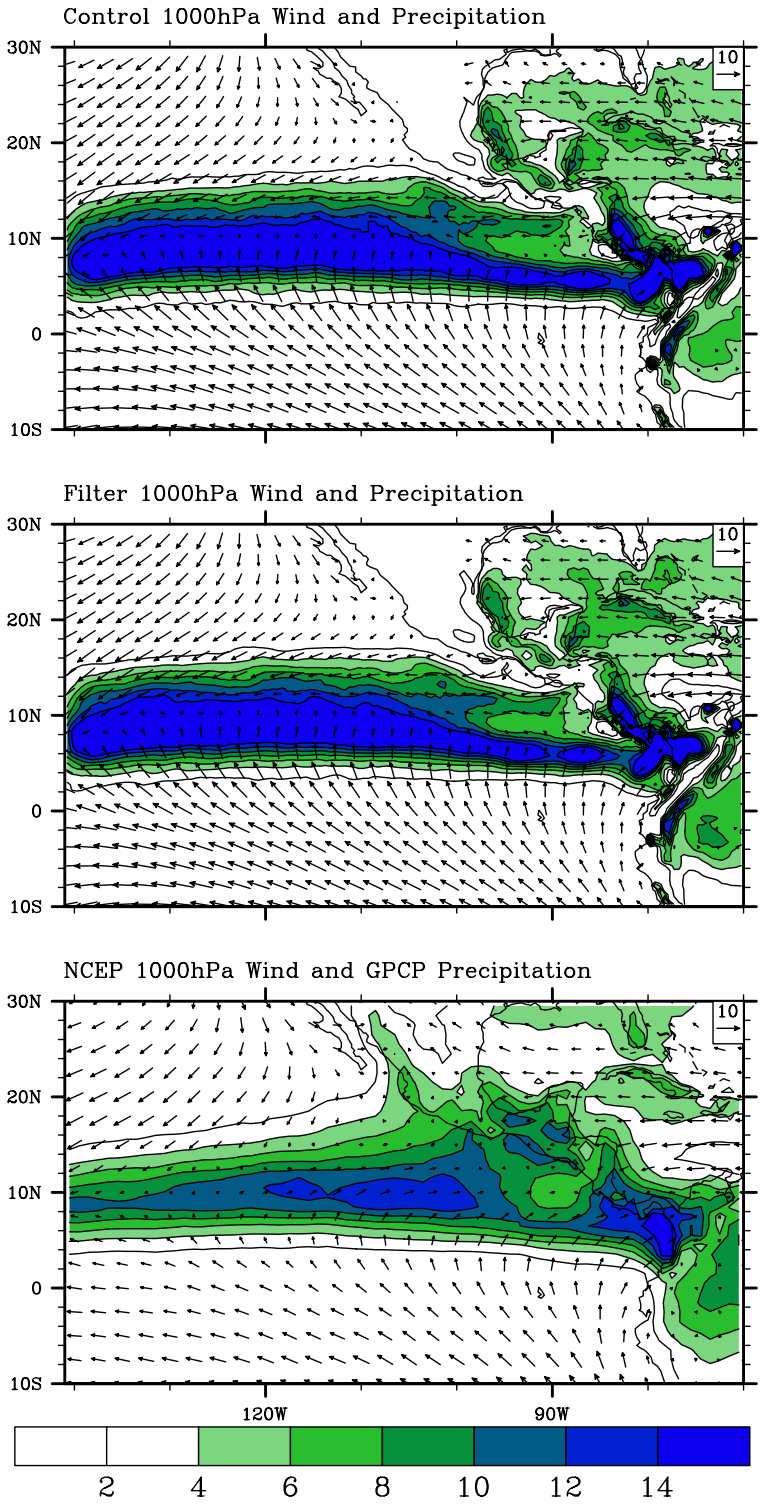

Figure 3.23 (a) IRAM control model 850-hPa horizontal winds (m/s, vectors) and precipitation (mm/day, contours). **(b)** Same as figure (a) except for IRAM filter model. **(c)** NCEP 1000-hPa horizontal winds (m/s, vectors) and GPCP precipitation (mm/day, contours).

3.2.3. Model Variability

The IRAM has shown to reasonably represent intraseasonal variability in the east Pacific compared with observations. Small et al. (2010) analyzed IROAM, the fully coupled atmosphere ocean model, intraseasonal variability by comparing with NCEP/NCAR reanalysis using a low-level zonal wind index. They found that the indices are highly significant at the 99% confidence level. Intraseasonal precipitation in the heart of the warm pool also had similar dominant timescales to those of observations as well as similar temporal evolutions of outgoing longwave radiation and zonal winds. For the atmospheric only part of the model used in the study, similar intraseasonal variability is found.

The intraseasonal variability in the IRAM is further documented here. Figure 3.24 shows the spatial structure of 30-90-day filtered 850-hPa zonal wind variance in the east Pacific for both IRAM model versions for June – October. The IRAM control model is comparable in both magnitude and location of 30-90-day variance to observations (figures 3.5 (c) and 3.6 (c)). The IRAM filter model has much weaker intraseasonal variance on the order of 1-2 m^2/s^2 in the same region as the control model. Figure 3.25 shows the 30-90-day filtered precipitation variance in both models for the same summer months. Both have similar regions of variance along the ITCZ. Most notable are the difference in magnitudes of variance in the east Pacific warm pool region from 120°W to 95°W. The control model has over twice the variance of the filter model in this region. The control model also has a northern local maximum along the Mexican coastline at 15°N, 103°W that is absent in the filter model. This local maximum

agrees well with the intraseasonal maximum in the lag regression plots of Small et al. (2010) (figure 8 (d), (f)) and composites shown later that are derived from global and local indices. By constraining the boundaries in the filter model, the 30-90-day filtered 850-hPa zonal wind and precipitation variances are reduced.

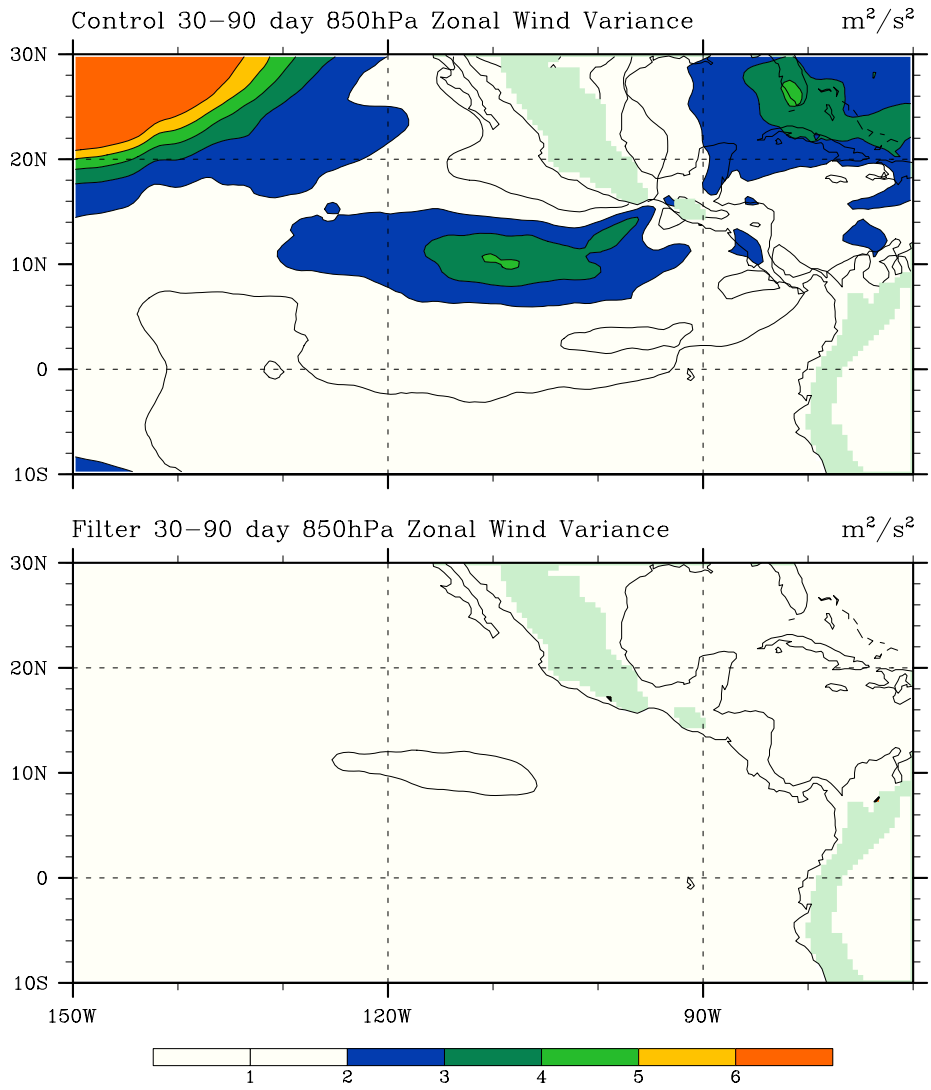

Figure 3.24 (a) 30-90 day filtered 850-hPa zonal wind variance (m^2/s^2) in the IRAM control model for June - October. **(b)** Same as (a) except for the IRAM filter model. Contour interval is 1 m^2/s^2.

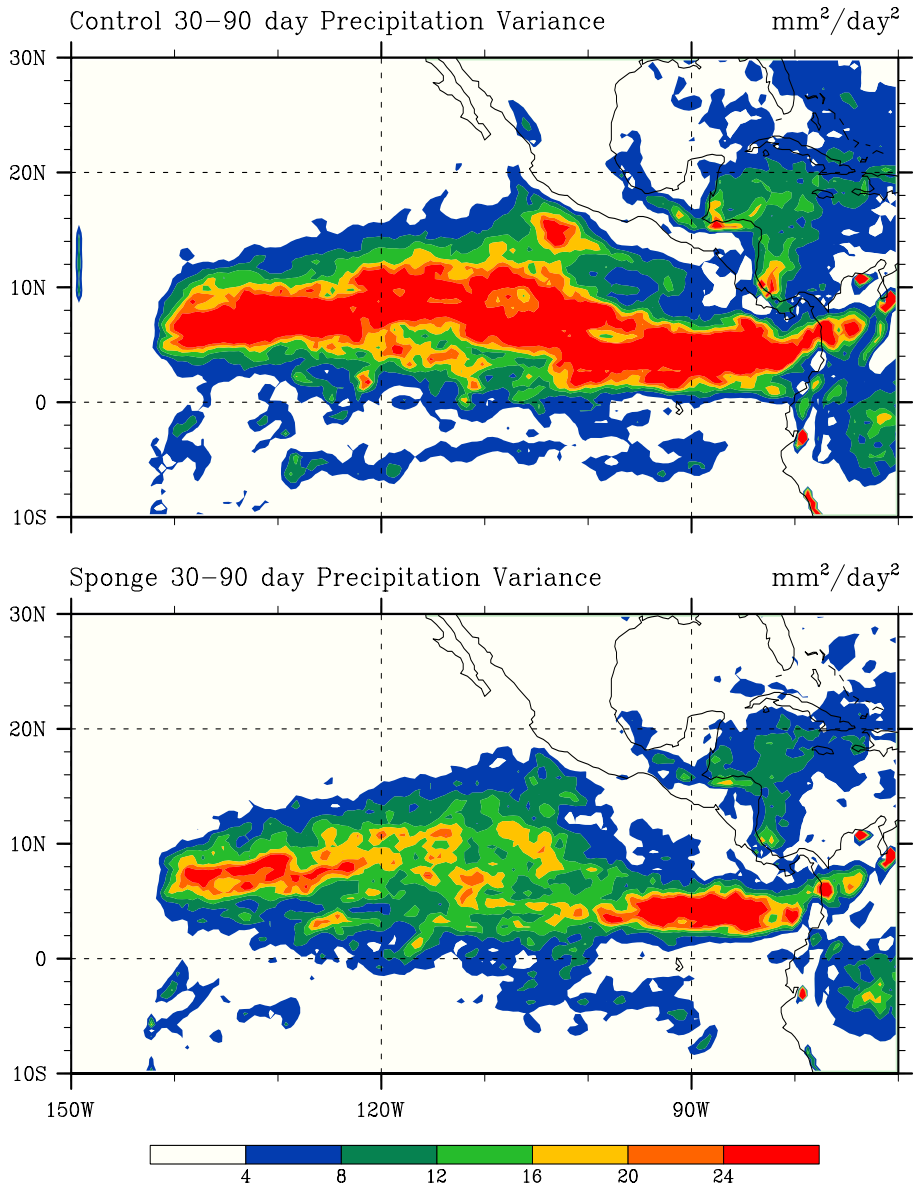

Figure 3.25 (a) 30-90 day filtered precipitation variance (mm^2/day^2) in the IRAM control model for June - October. **(b)** Same as (a) except for the IRAM filter model. Contour interval is 4 mm^2/day^2.

In evaluating the power spectra for 850-hPa winds and precipitation in the model versions, each individual summer (June – October) was evaluated over the 12-year period from 1997 – 2008 and averaged together for the power spectra. The variables for each power spectrum were first averaged over a 10° x 10° box with the center point of the box shown in the figure. Strong power exists

at similar dominant timescales to observations in the control model 850-hPa zonal winds and precipitation (figure 3.26). Both 850-hPa zonal winds and precipitation have significant peaks that exceed 95% significance at 50-day periods in the middle of the east Pacific warm pool.

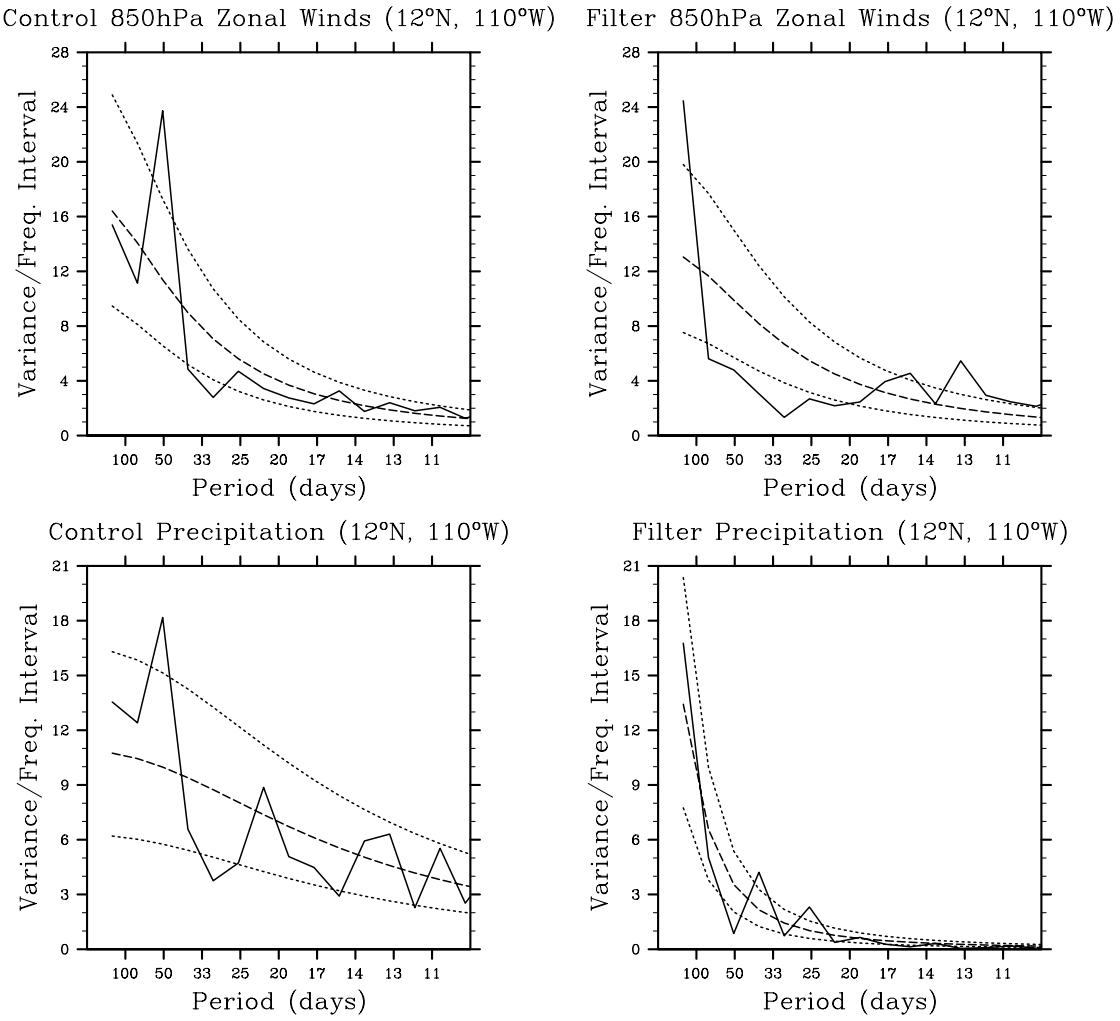

Figure 3.26 Power Spectrum for **(a)** IRAM control model **(b)** IRAM filter model 850-hPa zonal winds and **(c)** IRAM control model and **(d)** IRAM filter model precipitation for the summer season. Values are averaged over a 10°x10° box centered on the shown latitude and longitude. Dashed line is red noise spectrum and dotted lines are the upper and lower 95% and 5% upper and lower bounds, respectively.

In the IRAM filter model, a similar analysis of summer season power spectra reveal no significant power on intraseasonal timescales for 850-hPa

zonal winds and only marginally significant power in precipitation at shorter periods than the observations (figure 3.26). Unlike the IRAM filter model, the CAM3 sponge model has significant power in precipitation at comparable periods to observations. Both the IRAM filter and CAM3 sponge models have insignificant power at 30-90-day periods in 850-hPa zonal winds.

3.2.4. Composites

In order to look at east Pacific intraseasonal variability in the broader context of global MJO activity, an MJO index is formed based on global 30-90-day NCEP 850-hPa zonal wind, NCEP 200-hPa zonal wind, and GPCP precipitation anomalies. The dates averaged for each phase of the composite are then applied to IRAM data and used to form IRAM control and filter model composites. Figure 3.27 shows the NCEP and GPCP composite based on the global index zoomed in on the east Pacific. Both ERAi/GPCP (figure 1.1) and NCEP/GPCP composites (figure 3.27) are very similar in phase, structure, and amplitude in the evolution of east Pacific intraseasonal events based on a global MJO index. Both have the same phase evolution of winds and precipitation with the dipole structure in precipitation along the 120°W longitude axis in the east Pacific.

Figure 3.28 shows the IRAM control model composite plots based on the same global composite index as figure 3.27. Generally, the IRAM model has much weaker 30-90-day 850-hPa zonal wind and precipitation anomalies compared to observations. The IRAM control model also has much more latitudinal structure in the precipitation field with adjacent negative and positive

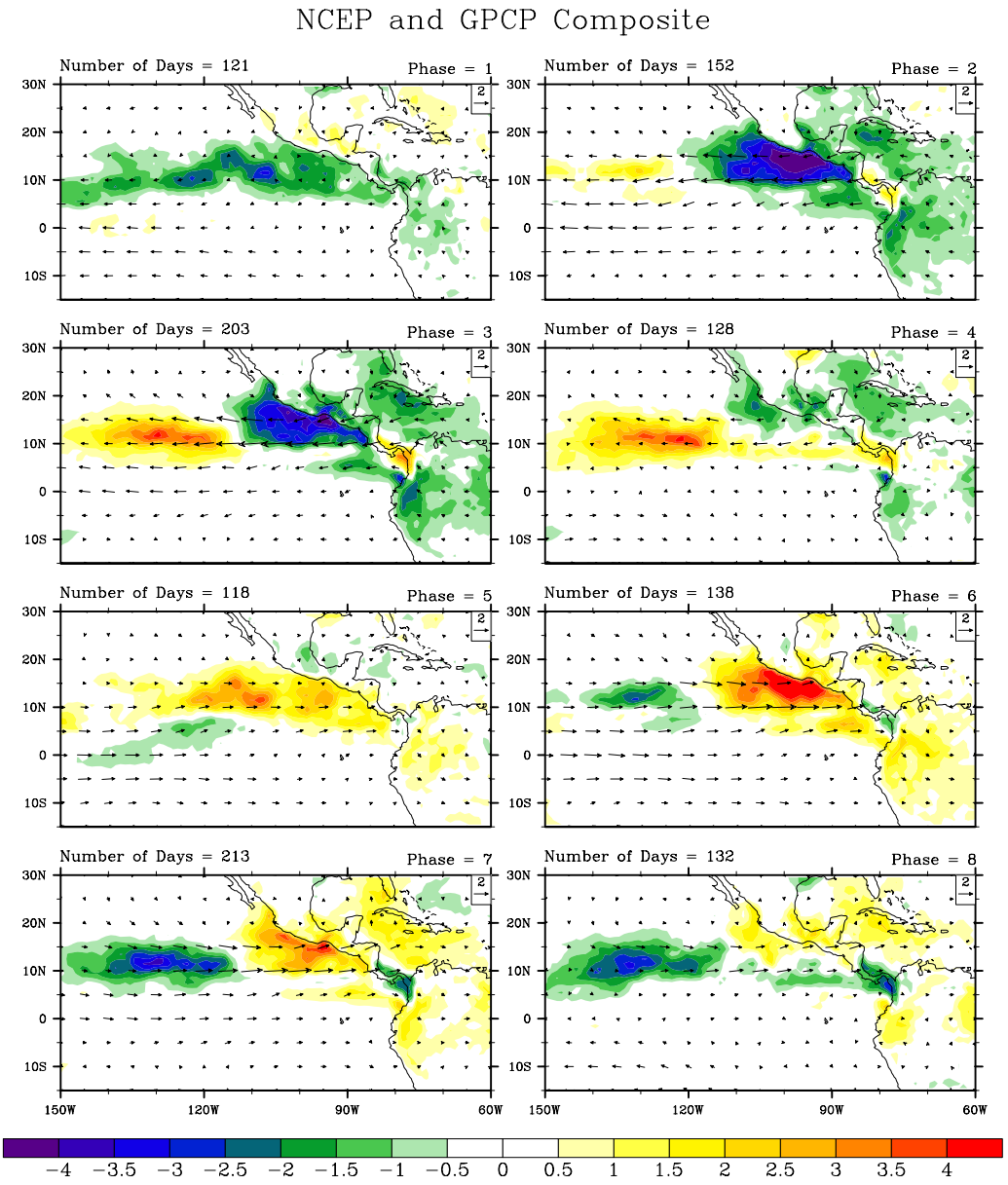

Figure 3.27 NCEP and GPCP MJO composite of 30-90-day filtered 850-hPa horizontal wind anomalies (m/s, vectors) and precipitation (mm/day, contours) for 1997 – 2008 summers (June – October) zoomed in for east Pacific.

intraseasonal precipitation anomalies. Some of the differences in composite structure might be a result of the differences in grid spacing. North of 5°N the precipitation field has a very weak dipole structure in precipitation with similar phases of zonal winds to that of the NCEP/GPCP composite plots in phase 6. The phase of the 850-hPa zonal winds in the east Pacific warm pool are

generally in phase with 850-hPa equatorial zonal winds on the western boundary of the model presumable due to the phasing that occurs with Kelvin wave signals from MJO convection in the Eastern Hemisphere reanalysis being communicated at the model boundaries. The IRAM control model does not have the same amplitude of intraseasonal 850-hPa zonal wind and precipitation anomalies as observations. The 30-90-day 850-hPa wind anomalies have similar phases to observations, but the 30-90-day precipitation anomalies do not display the same longitudinal structure typically associated with the wind phases in observations.

For the IRAM filter model, figure 3.29 shows the composite based on the global NCEP/GPCP indices. Intraseasonal 850-hPa horizontal wind and precipitation anomalies are weak and no discernible phase relationship between the two is evident. No coherent dipole structure in the intraseasonal precipitation field is present and the field appears to be mainly composed of noise. The 850-hPa zonal wind anomalies do not show any coherent structure and no equatorial westerly or easterly winds are seen propagating into the east Pacific from the western boundary. When the student's t test is applied to each phase, the east Pacific 30-90-day precipitation and horizontal wind anomalies are not significant at the 95% level (regions on land along the Sierra Madre and Andes Mountains are significant in precipitation but over very small areas). These results are consistent with the filter effectively removing intraseasonal signals at the boundaries.

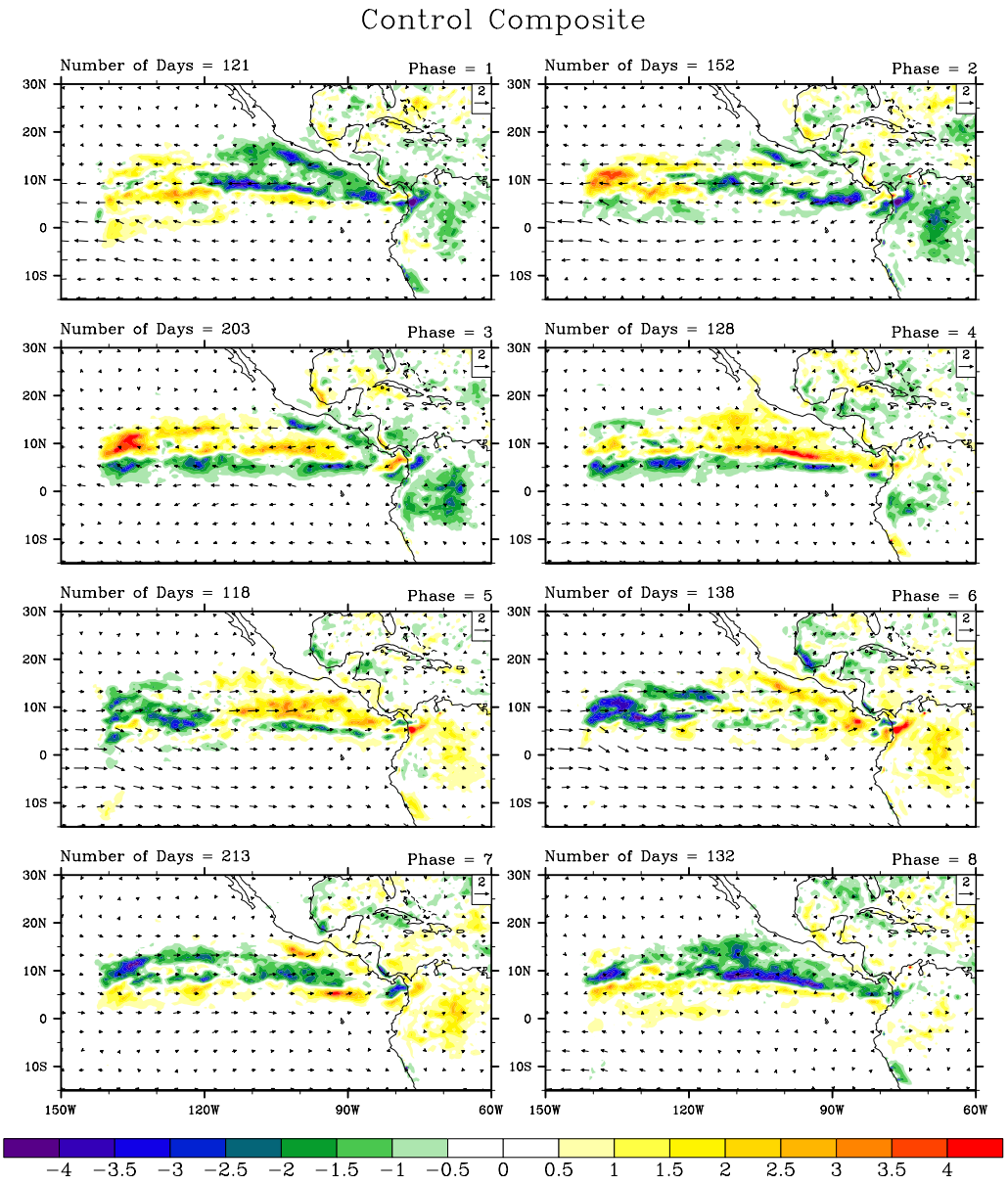

Figure 3.28 IRAM control model MJO composite of 30-90-day filtered 850-hPa horizontal wind anomalies (m/s, vectors) and precipitation (mm/day, contours) for 1997 – 2008 summers (June – October) zoomed in for east Pacific.

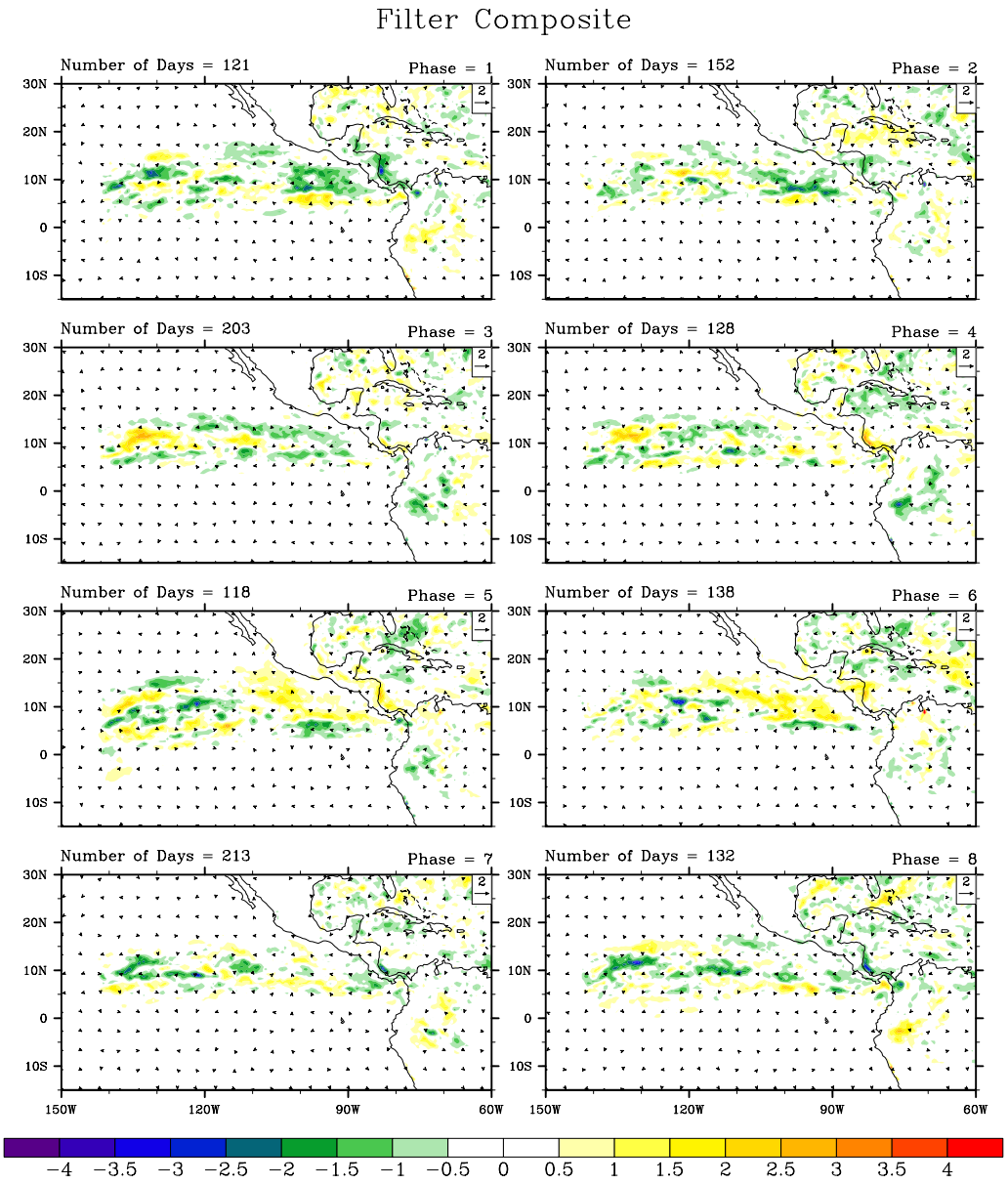

Figure 3.29 IRAM filter MJO composite of 30-90-day filtered 850-hPa horizontal wind anomalies (m/s, vectors) and precipitation (mm/day, contours) for 1997 – 2008 summers (June – October) zoomed in for east Pacific.

Although the IRAM control and filter models do not share similar evolutions of intraseasonal variability in the east Pacific when based on a global MJO index of reanalysis data, they may still share some essential local modes of 30-90-day variability. Figures 3.30, 3.31, and 3.32 show local multivariate EOFs of 30-90-day filtered 850-hPa zonal wind (color contours) and precipitation (line

contours) anomalies over the shown domain for NCEP/GPCP reanalysis, IRAM control model, and IRAM filter model, respectively. In the NCEP/GPCP reanalysis and IRAM control model, only the first EOFs are significant according to the criterion of North et al. (1982). None of the EOFs in the IRAM filter model are separable according to the North et al. (1982) criterion. In the reanalysis data, the first EOF has the zero precipitation contour generally following 120°W and separating opposite signed maxima in precipitation centered at 12°N, 135°W and 12°N, 110°W, respectively. There are two maxima in 850-hPa zonal winds with one along the equator to the south of the westernmost precipitation maximum and one in and to the west of the eastern precipitation maximum. The first EOF in the IRAM control model has similar structure to observations with a wind maximum over much of the east Pacific warm pool extending westward in the equatorial waveguide. North of 6°N, the zero precipitation contour is generally along 120°W and separates opposite signed maxima. These first EOFs in observations and the IRAM control model relate to the intraseasonal low-level westerly phase that is associated with the dipole precipitation pattern. The first EOF in the filter model is difficult to relate to physical processes. The structure is suggestive of positive precipitation anomalies east of 120°W in the east Pacific warm pool in association with intraseasonal low-level westerlies. The first EOF of the IRAM filter model explains less than a third of the intraseasonal variability that is explained by the first EOF of observations. The second EOFs in both IRAM model versions and reanalysis are not significant. In the multivariate analysis, east Pacific intraseasonal variability in the IRAM filter

model has fundamentally different modes than observations and the IRAM control model.

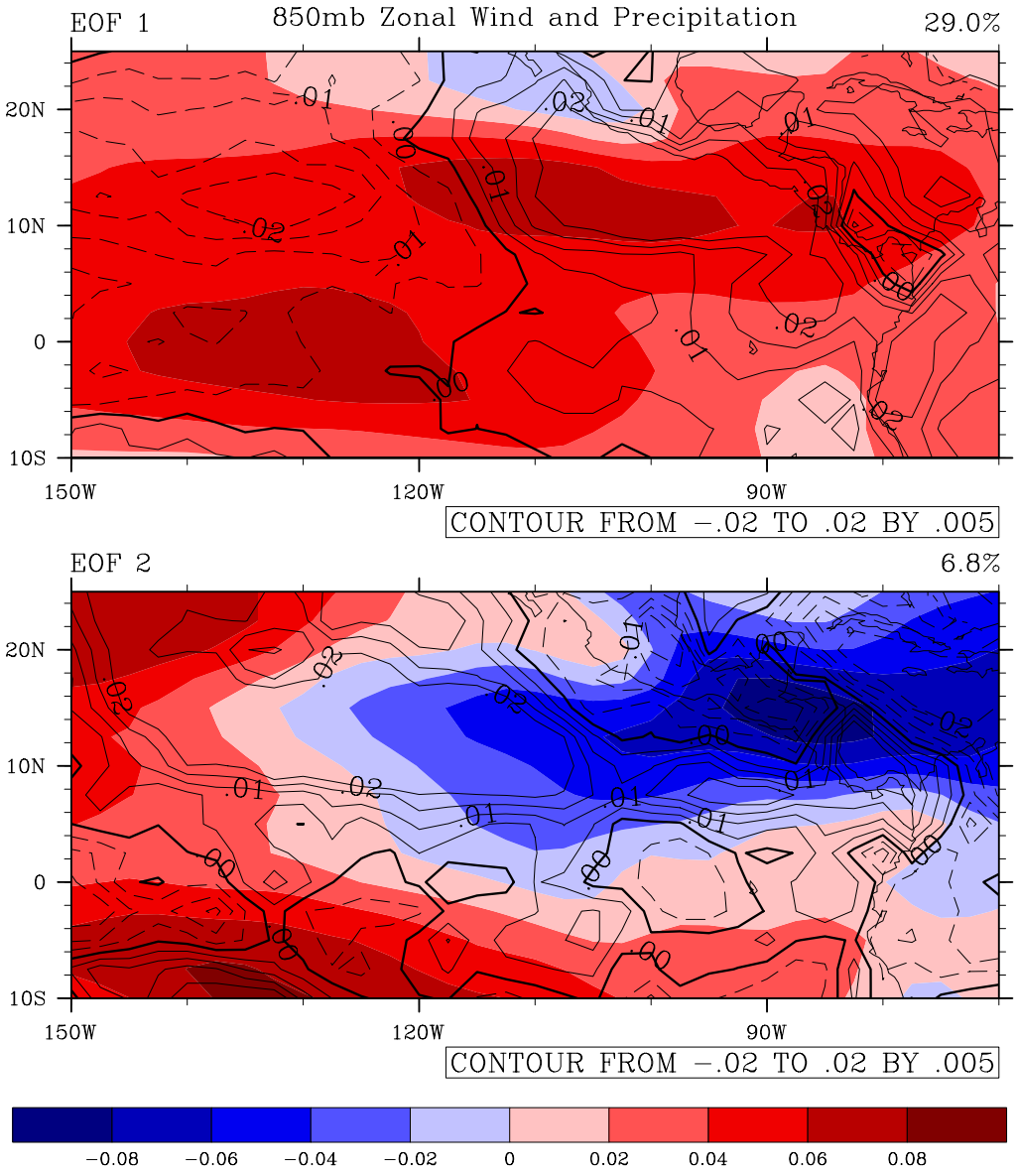

Figure 3.30 Multivariate EOF analyses of the GPCP and NCEP reanalysis 30-90-day precipitation (line contours) and 850-hPa zonal winds anomalies (color contours) over the shown domain. The contour interval for the precipitation anomalies is .005 and is .02 for the 850-hPa zonal wind anomalies. Variance explained by each EOF is shown in upper right hand corner.

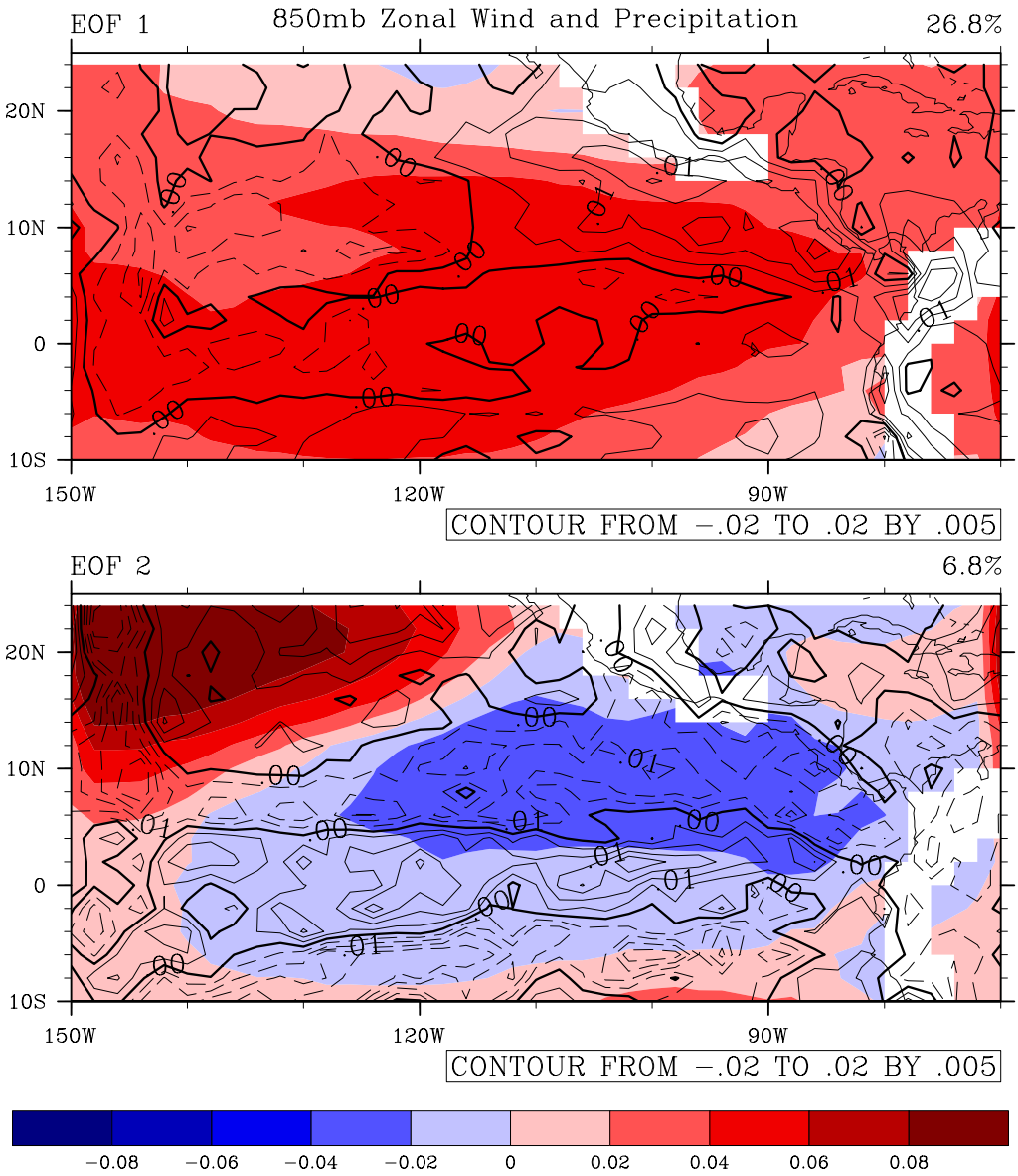

Figure 3.31 Multivariate EOF analyses of the IRAM control model 30-90-day precipitation (line contours) and 850-hPa zonal wind anomalies (color contours) over the shown domain. The contour interval for the precipitation anomalies is .005 and is .02 for the 850-hPa zonal wind anomalies. Variance explained by each EOF is shown in upper right hand corner.

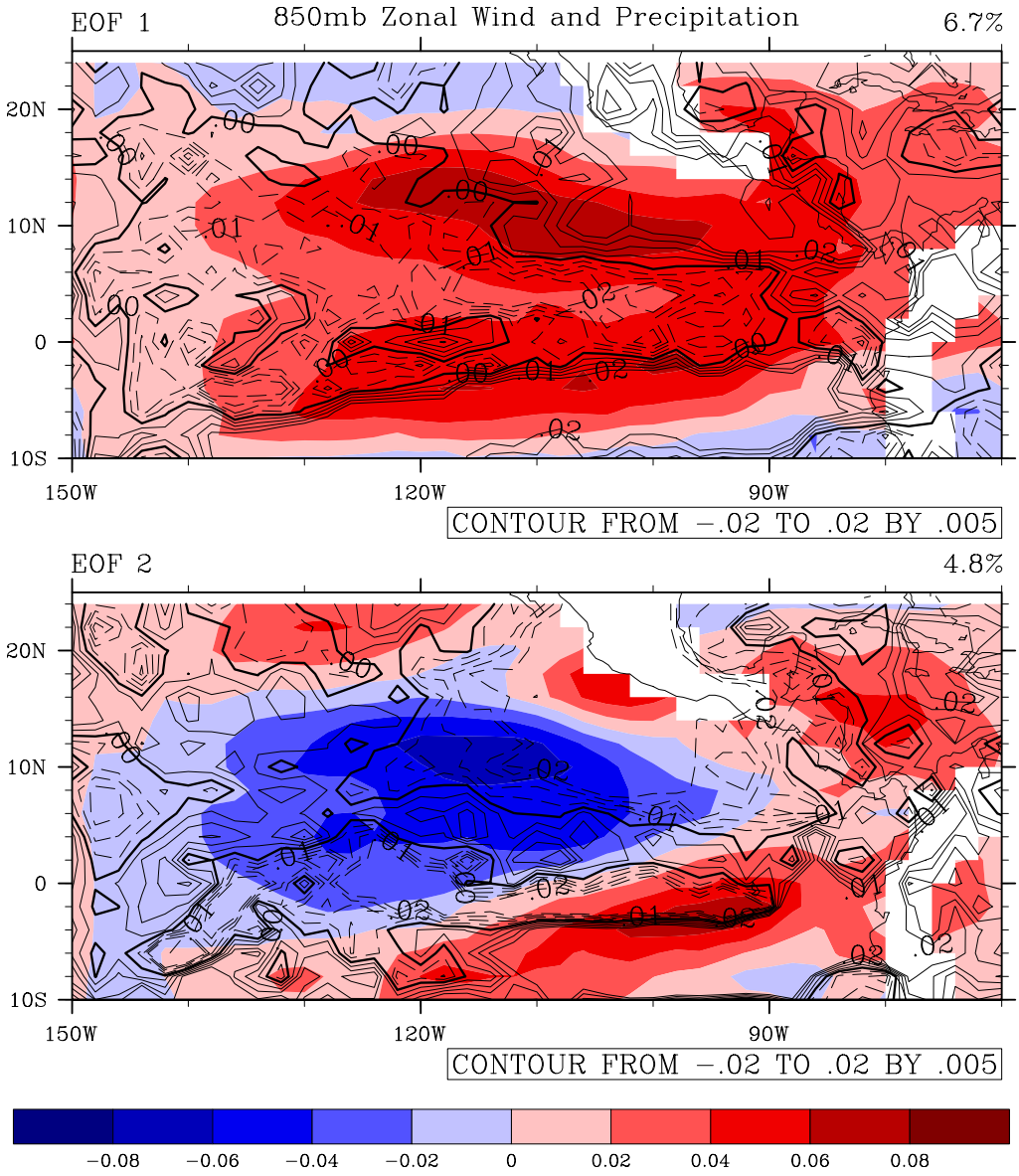

Figure 3.32 Multivariate EOF analysis of the IRAM filter model 30-90-day precipitation (line contours) and 850-hPa zonal wind anomalies (color contours) over the shown domain. The contour interval for the 850-hPa zonal wind and precipitation anomalies is .02 and .005, respectively. Variance explained by each EOF is shown in upper right hand corner.

To determine how intraseasonal variability evolves in the IRAM control and filter models when not indexed by the global MJO, a local index is used. In figure 3.33 the IRAM control model shows similar but stronger intraseasonal variability to the composite based on a global MJO index (figure 3.28). Enhanced positive 30-90-day precipitation anomalies occur in the east Pacific

warm pool during lags -5, 0 and 5 and are embedded in 30-90-day 850-hPa westerly anomalies. The local composite for the IRAM filter model also shows a weaker structure of enhanced precipitation anomalies embedded in westerlies at lags -5 and 0 near 10°N, 105°W (figure 3.34). Although westerly 850-hPa wind anomalies are present in the positive 30-90-day precipitation anomalies in lags -5 and 0 east of 120°W in both models, easterly phases of 850-hPa wind anomalies associated with negative 30-90-day precipitation anomalies are only present in the IRAM control model. Both composites have a comparable number of events from which they are averaged. Hence, east Pacific intraseasonal variability in the IRAM is strongly influenced by the MJO because significant intraseasonal variability at 50-day periods in low-level wind and precipitation does not exist in the absence of remote intraseasonal signals. However, the control model produces east Pacific 30-90-day low-level wind and precipitation anomalies in phase with global MJO activity.

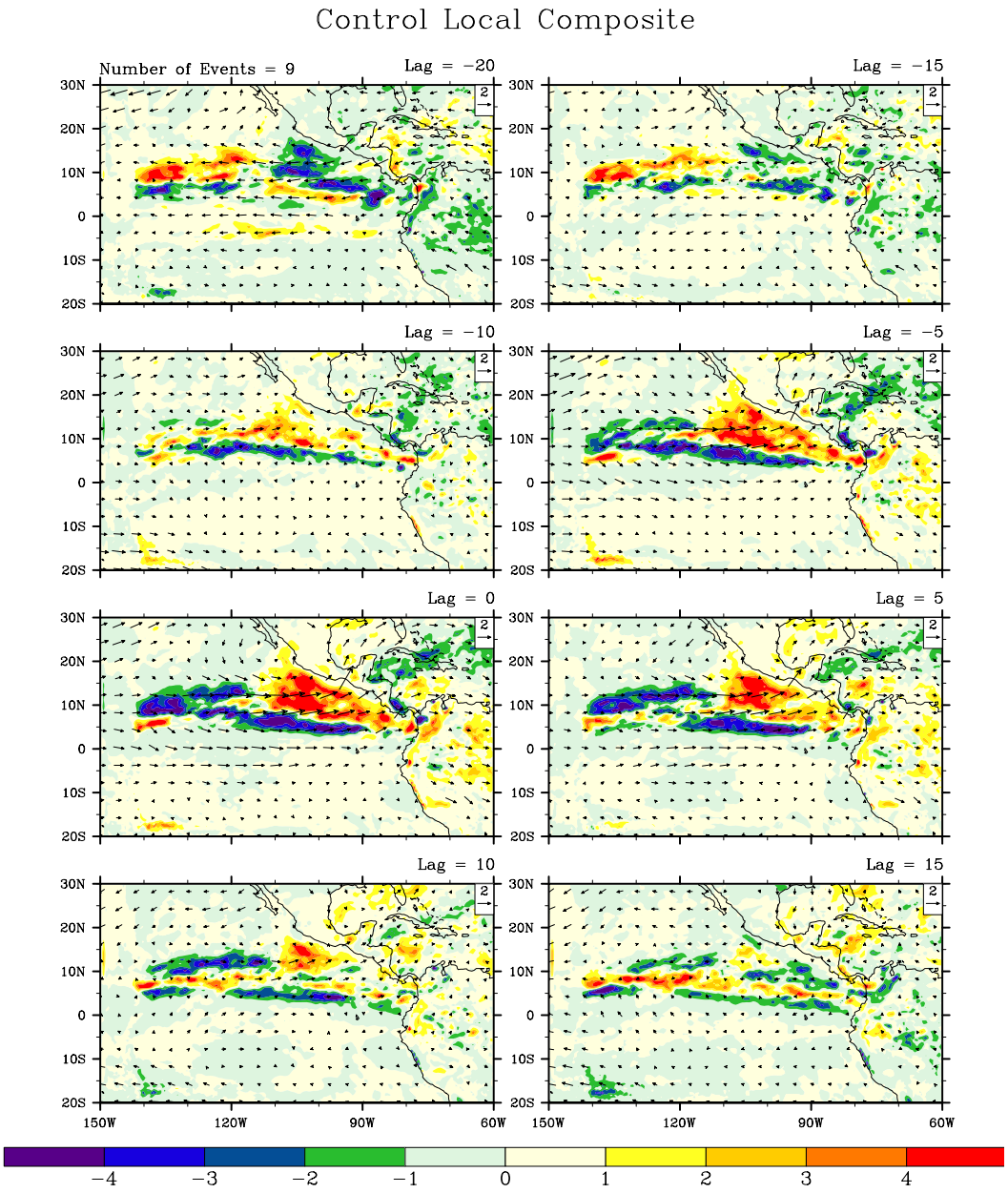

Figure 3.33 Local composite of 30-90-day precipitation (mm/day, contours) and 850-hPa wind anomalies (m/s, vectors) for the IRAM control model.

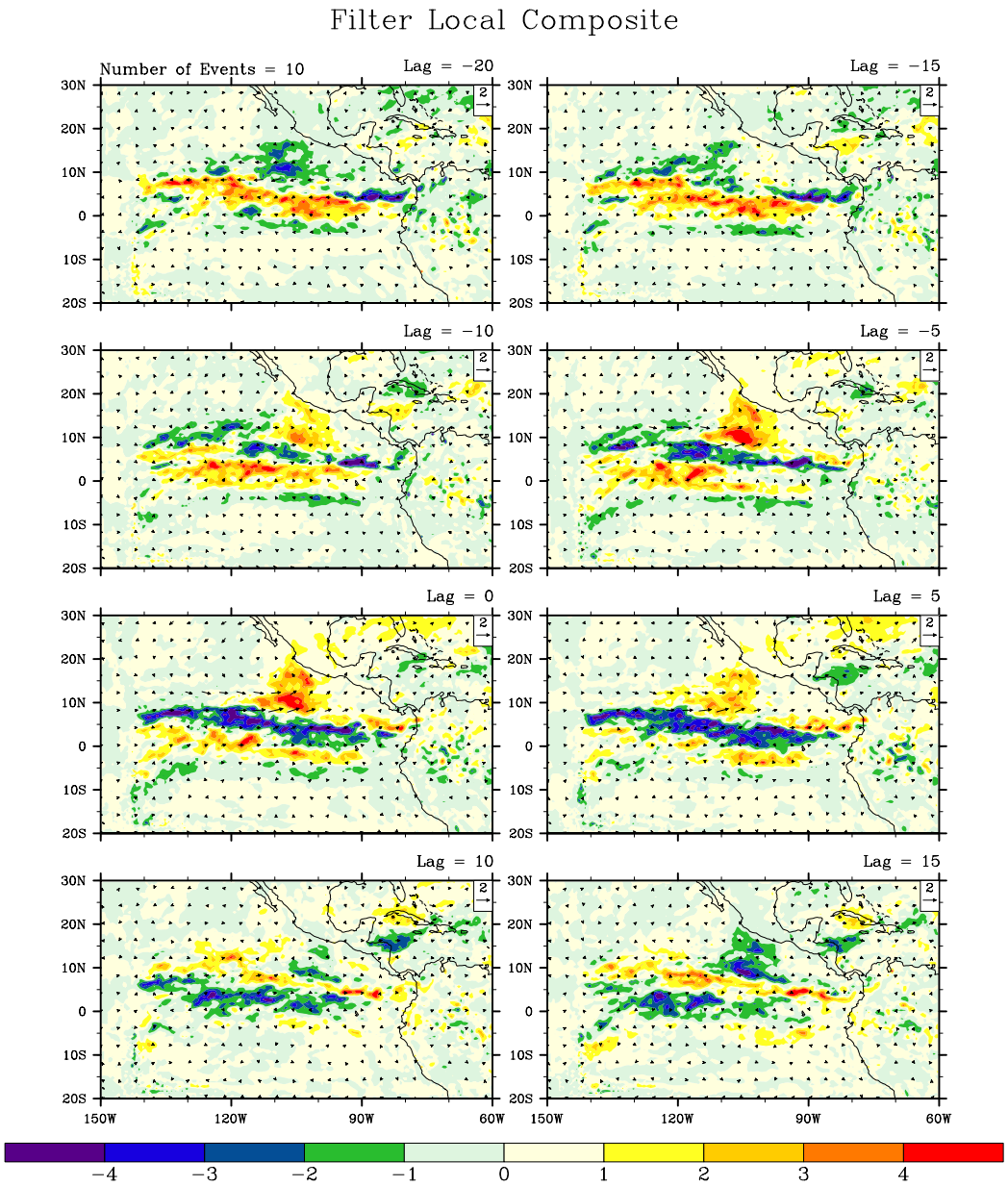

Figure 3.34 Local composite of 30-90-day precipitation (mm/day, contours) and 850-hPa wind anomalies (m/s, vectors) for the IRAM filter model.

3.2.5. Possible Mechanisms

In the IRAM model, east Pacific intraseasonal variability is not significant at characteristic 50-day periods when isolated from the MJO. These results suggest that communication from Eastern Hemisphere intraseasonal variability is necessary to the initiation and maintenance of east Pacific intraseasonal

variability. The principal form of intraseasonal communication between the equatorial Eastern Hemisphere and east Pacific is the Kelvin wave. Intraseasonal convective anomalies do not typically propagate east of the date line (figure 1.1). An important topic in this framework is the mechanisms by which convective coupling reoccurs in the east Pacific. Possible mechanisms of the convective recoupling in the IRAM control model are briefly discussed.

In observations, summer climatological westerlies are present in the summer climatological precipitation region east of 120°W (figure 3.23 (c)). During phases 5, 6, 7, and 8 of the global composite from NCEP and GPCP reanalysis (figure 3.27), 30-90-day 850-hPa westerly anomalies constructively add to the climatological westerlies to enhance the wind induced surface heat exchange. The important relationship between intraseasonal wind induced latent heat fluxes and intraseasonal precipitation in east Pacific observations is well documented (Maloney and Esbensen 2003, Maloney and Esbensen 2007). The composite field of 30-90-day latent heat flux anomalies based on the global index for the IRAM control model is fundamentally different than observations (figure 3.35). Because the IRAM model summer climatological low-level flow in the east Pacific warm pool is easterly, compared to westerly for observations, intraseasonal westerly anomalies do not constructively add to the mean flow. During intraseasonal easterly phases in the IRAM control model, the easterly anomalies constructively add to the mean easterly flow and enhance surface latent fluxes. During intraseasonal westerly phases, the mean flow is weakened by the wind anomalies and the 30-90-day latent heat flux anomalies are negative

in the east Pacific warm pool. This composite suggests that because the IRAM model has summer climatological easterlies in the east Pacific warm pool, the 30-90-day latent heat flux anomalies have an opposite sign from observations during an intraseasonal event. In the IRAM model of Small et al. (2010) with climatological westerlies in the east Pacific warm pool, positive intraseasonal latent heat flux anomalies are associated with westerly intraseasonal low-level wind anomalies and positive intraseasonal precipitation anomalies (Small et al. 2010 figure 15 (b) and (d)). Hence, these results suggest that the mean state of the low-level wind in the east Pacific warm pool is important in model representations of east Pacific intraseasonal variability through wind induced surface heat exchange mechanisms.

The composite plot of 30-90-day 1000-hPa convergence anomalies is consistent with the CAM3 model versions (figure 3.36). Weak 1000-hPa divergence anomalies occur during intraseasonal easterly phases. During intraseasonal westerly phases, 1000-hPa convergence anomalies present at 15°N between 120°W - 110°W during phase 5. The anomalies then become enhanced near the coastline during phases 6 and 7. The convergence anomalies are coincident with the weakly positive 30-90-day precipitation anomalies in the same regions during phases 6 and 7. The strongest positive 30-90-day precipitation anomalies occur during the weak westerly/easterly phases are not associated with strong 30-90-day latent heat flux or 100-hPa convergence anomalies.

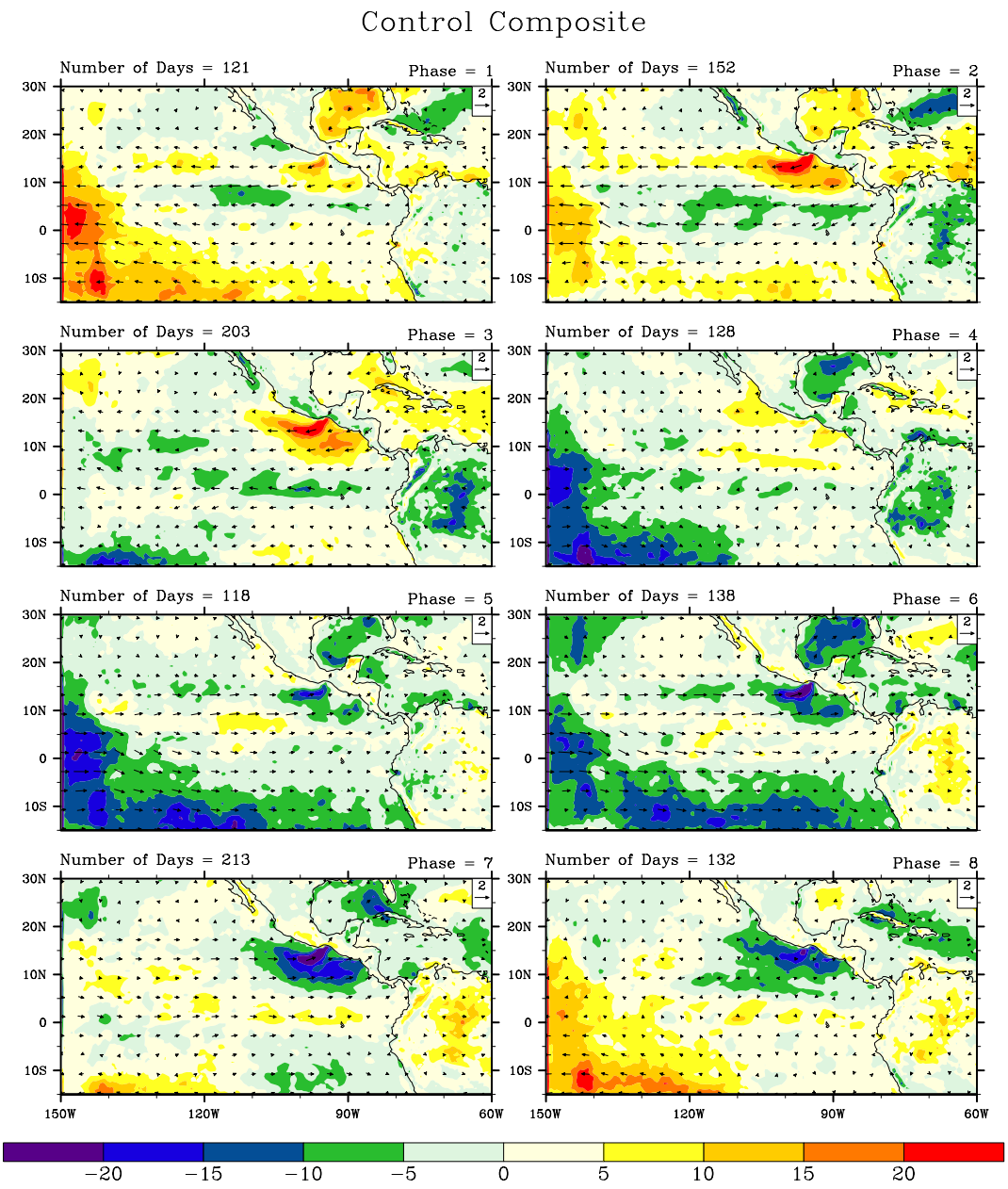

Figure 3.35 Global composite of 30-90-day latent heat flux anomalies (W/m^2, contours) and 30-90-day 850-hPa zonal winds anomalies (m/s, vectors) for the IRAM control model.

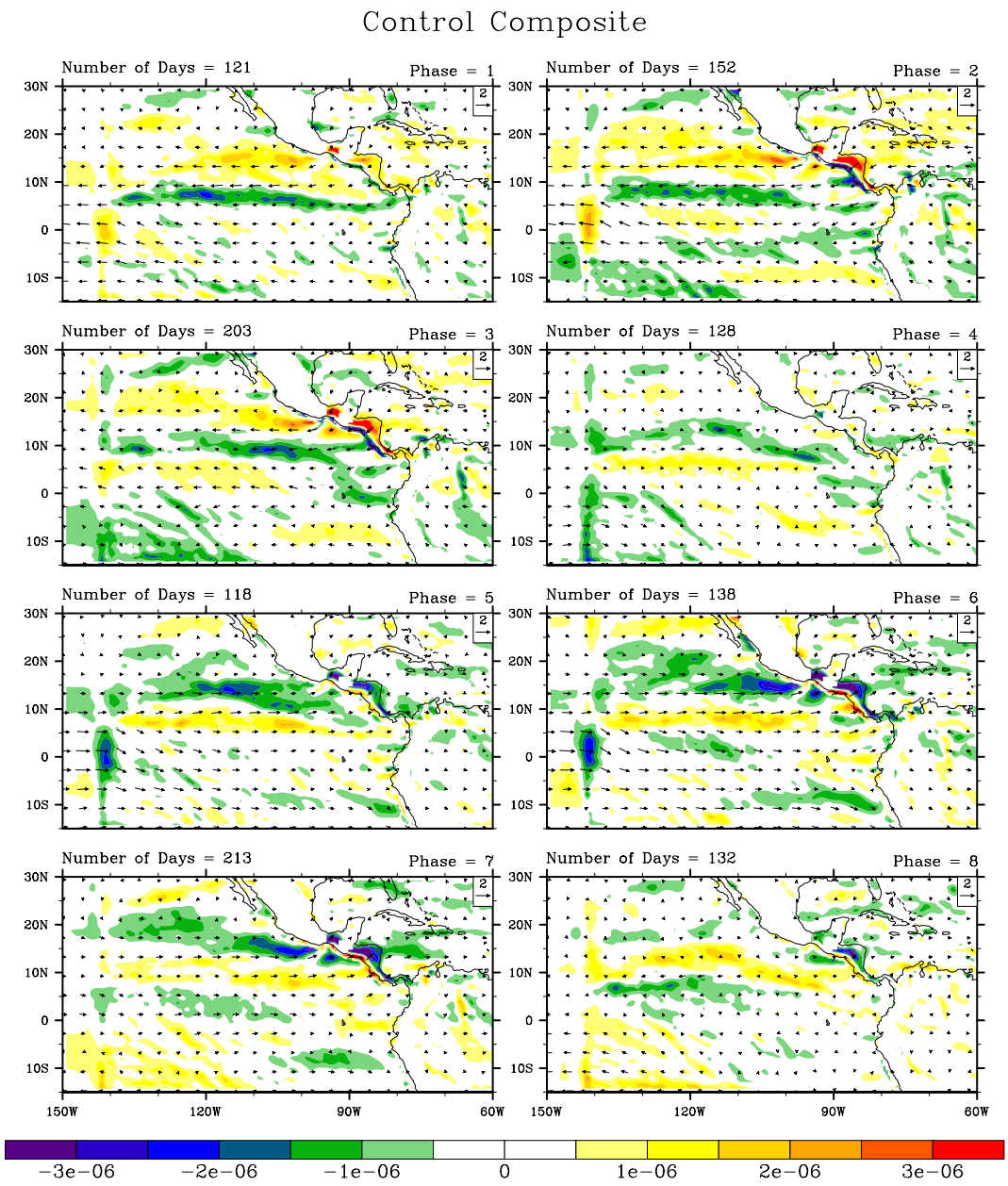

Figure 3.36 Local composite of 30-90-day 1000-hPa divergence anomalies (s^{-1}, contours) and 30-90-day 850-hPa horizontal wind anomalies (m/s, vectors) for the IRAM control model.

4. Summary and Conclusion

The sensitivity of two models to the isolation of the east Pacific from global MJO activity was analyzed. The purpose of this study was to determine the nature of the interactions between the MJO in the Eastern Hemisphere and intraseasonal variability in the east Pacific. A couple of interactions are possible. The first category is that of east Pacific independence on intraseasonal timescales such that east Pacific intraseasonal variability can exist in similar form without influence from the MJO. This theory suggests that the physical requirements and mechanisms for east Pacific intraseasonal variability are locally available and do not require any remote influences. The second category is that of east Pacific dependence to the MJO on intraseasonal timescales. If isolated from the MJO, east Pacific intraseasonal variability is not significantly different from noise. These categories are used to distinguish the relative importance of local and remote controls on east Pacific intraseasonal variability.

Several theories have been suggested to qualitatively describe the effects and relative contributions of remote and local controls of east Pacific intraseasonal variability. Small et al. (2010) suggests that dry Kelvin waves associated with the suppressed convective phase of the MJO in the Eastern Hemisphere propagate rapidly across the Pacific Ocean in response to a negative heating anomaly. The cool tropospheric temperature anomalies and

westerly winds associated with the Kelvin wave help destabilize the east Pacific. Additionally, Ekman convergence on the northern flank of the Kelvin wave could initiate an intraseasonal event. Strong communication between the Eastern Hemisphere MJO and intraseasonal variability in the east Pacific is supported in correlations of their time series (Maloney et al. 2008).

Some have suggested that the intraseasonal variability in the east Pacific could be sustained apart from the intraseasonal influences of the Eastern Hemisphere (Zhang and Dong 2004; Jiang et al. 2011). The main support in both general circulation models and observations is the absence of MJO convective signals in the central Pacific Ocean to strongly link the two basins. However, strong dynamical signals do link the two basins. Jiang et al. (2011) states that general circulation models with the most realistic representations of east Pacific intraseasonal variability have intraseasonal convective signals that originate in the central Pacific.

In order to isolate the east Pacific from the eastward propagating MJO that originates in the Eastern Hemisphere, various strategies were implemented in this study. In the CAM3 model, first efforts to remove intraseasonal variability in the Eastern Hemisphere by the suppression of intraseasonal surface fluxes were unsuccessful. By setting the surface fluxes to their summer season climatological value, MJO variability was reduced but not completely removed. Eastward propagating wind components were still present and entered the east Pacific, similar to the NO-WISHE runs in Maloney and Sobel (2004), even though precipitation variability was strongly reduced. Instead of setting surface fluxes to

their climatological values, a more effective strategy for removing MJO influence on the east Pacific in CAM3 was the inclusion of a sponge region in the central Pacific that dampens the eastward propagation of Kelvin waves.

In the CAM3 sponge model, it was shown that the east Pacific was not significantly influenced by the MJO and could be regarded as independent on intraseasonal timescales. The CAM3 sponge model showed significant power at intraseasonal timescales in precipitation. Variance plots of 30-90-day precipitation and 850-hPa horizontal wind anomalies were slightly weaker but spatially consistent with the CAM3 control model. When a global index of MJO activity was applied to the CAM3 sponge model to form composite plots, 30-90-day precipitation and 850-hPa horizontal wind anomalies in the east Pacific were not coherent with the MJO in the Eastern Hemisphere. Because multivariate EOF analysis applied to the CAM3 control and sponge models over the east Pacific showed similar distributions and variance explained, and hence suggest that the dominant mode of variability did not change, a local intraseasonal index was used to create east Pacific model composites. The local model composites showed very similar precipitation anomaly structures and relationships to the associated 850-hPa zonal wind anomalies. Enhanced precipitation east of 120°W was associated with westerly 850-hPa wind phases and suppressed precipitation with easterly 850-hPa wind phases in both model versions. The precipitation and low-level wind relationship is consistent with previous observational studies (Maloney and Hartmann 2001; Maloney and Kiehl 2002).

The results based on the CAM3 model suggest that intraseasonal variability in the east Pacific warm pool can be sustained by local feedbacks in the absence of MJO remote controls. Further, local convective-circulation feedbacks appear to be important to the initiation and maintenance of east Pacific warm pool intraseasonal events as shown in the evolution of surface convergence and latent heat fluxes. The Eastern Hemisphere and east Pacific perhaps share resonant frequencies that are easily harmonized through rapid eastward Kelvin wave propagation. Additionally, because intraseasonal variability in the east Pacific is larger in the control model than the sponge model no matter the compositing technique used, remote controls appear to positively contribute to intraseasonal oscillations there. Again, Kelvin waves that propagate rapidly across the Pacific Ocean can initiate and constructively contribute to the westerly and easterly phases that are associated with the strongest 30-90-day precipitation anomalies. The exact mechanisms will be examined in future work, although composite analysis suggests wind-induced flux anomalies and frictional convergence may be two physical mechanisms by which Eastern Hemisphere variability and associated Kelvin waves may help initiate and support east Pacific intraseasonal variability.

The IRAM model chosen in this study is particularly useful because boundary conditions can be directly controlled such that intraseasonal variability can be removed so as not to influence the model domain. This provides a very useful tool to evaluate the independence of east Pacific intraseasonal variability. To remove the propagation of intraseasonal variability into the east Pacific in the

IRAM filter model, 30-90-day variability was removed from the NCEP/NCAR reanalysis model boundary forcing. In the IRAM control model, significant power in both precipitation and 850-hPa zonal winds at timescales similar to observations was evident with similar spatial structure. In the IRAM filter model, significant power at intraseasonal timescales was not present in 850-hPa zonal winds and marginally significant in precipitation at intraseasonal timescales less than observations. When the global MJO index based on NCEP/NCAR and GPCP reanalysis data was applied to the IRAM control model to create composites, the phases and amplitudes of 30-90-day 850-hPa zonal wind and precipitation anomalies in the east Pacific, although much noisier, generally agreed with observations. For the IRAM filter model, the amplitude of the composite fields was generally much weaker and not coherent with the global MJO. Further examination using the student's t-test revealed that the IRAM filter composites were not significant at the 95% significance level. The IRAM filter model in the east Pacific did not project well onto the global measure of MJO variability. In the local multivariate EOF analysis of the IRAM filter model, the first EOF explained less than a third of the intraseasonal variance than the first EOF of the IRAM control model and was not significant. When composited based on a local index, both IRAM models showed that westerly phases of 30-90-day 850-hPa zonal wind anomalies are associated with enhanced 30-90-day precipitation anomalies east of 120°W, although the IRAM filter model composite fields are substantially weaker than the control model. The IRAM model does not support the ability for the east Pacific warm pool to sustain significant and

independent intraseasonal oscillations in isolation from MJO activity. Conclusions derived from the IRAM model require further investigation due to the possibly important difference in sign of the climatological low-level winds compared to observations. The sign of the climatological low-level winds is critical to the phase of 30-90-day latent heat flux anomalies and thus the east Pacific moisture field.

Because Jiang et al. (2011) suggests intraseasonal convection originating in the central Pacific that may not necessarily be MJO-related could be important in the representation of east Pacific intraseasonal events, it would be useful to extend the domain of the IRAM model to include much more of the central Pacific. Particularly since IRAM only receives thermodynamic and dynamic fields at the boundaries and not explicit convection, the model could perhaps benefit from additional space on the western domain to allow convection to develop further west. Aside from extending the IRAM domain, future work includes performing a moist static energy budget in the CAM3 model versions to compare the development and maintenance of intraseasonal moist static energy anomalies in the east Pacific warm pool. Comparison of leading terms in the budget may be important in further determining the roles of local and remote controls of east Pacific intraseasonal variability, as well as the destabilization mechanism for local intraseasonal variability. Mechanisms found for east Pacific intraseasonal variability may be useful in the study of intraseasonal variability in the Eastern Hemisphere.

References

1. Back, L. E., and C. S. Bretherton, 2006: Geographic variability in the export of moist static energy and vertical motion profiles in the tropical Pacific. *Geophys. Res. Lett.*, 33, L17810.

2. Back, L. E, and C. S. Bretherton, 2009: On the relationship between between SST gradients, boundary layer winds and convergence over the tropical oceans. *J. Climate*, 22, 4182-4196.

3. Bordoni, S. and B. Stevens, 2006: Principal Component Analysis of the Summertime Winds over the Gulf of California: A Gulf Surge Index. *Mon. Wea. Rev.*, **134**, 3395–3414.

4. Dee, D. P., Uppala, S. M., Simmons, A. J., Berrisford, P., Poli, P., Kobayashi, S., Andrae, U., Balmaseda, M. A., Balsamo, G., Bauer, P., Bechtold, P., Beljaars, A. C. M., van de Berg, L., Bidlot, J., Bormann, N., Delsol, C., Dragani, R., Fuentes, M., Geer, A. J., Haimberger, L., Healy, S. B., Hersbach, H., Hólm, E. V., Isaksen, L., Kållberg, P., Köhler, M., Matricardi, M., McNally, A. P., Monge-Sanz, B. M., Morcrette, J.-J., Park, B.-K., Peubey, C., de Rosnay, P., Tavolato, C., Thépaut, J.-N. and Vitart, F., 2011: The ERA-Interim reanalysis: configuration and performance of the data assimilation system. *Quart. J. R. Met. Soc.*, 137: 553–597.

5. Emanuel, K. A., 1987: An air-sea interaction model of intraseasonal oscillations in the tropics. *J. Atmos. Sci.*, 44, 2324–2340.

6. Gill, A. E., 1980: Some simple solutions for heat-induced tropical circulation. *Quart. J. R. Met. Soc.,* 106, 447–462.

7. Hannah, W. M. and E. D. Maloney, 2011: The role of moisture–convection feedbacks in simulating the Madden–Julian Oscillation. *J. Climate*, 24, 2754–2770.

8. Heckley, W. A. and A. E. Gill, 1984: Some simple analytical solutions to the problem of forced equatorial long waves*. Quart. J. R. Met. Soc.,* 110, 203-217.

9. Hendon, H. H. and M. L. Salby, 1994: Life cycle of the the Madden Julian oscillation. *J. Atmos. Sci.*, 51, 2225-2237.

10. Hendon, H. H., B. Liebmann, M. E. Newman, J. D. Glick, and J. E. Schemm, 2000: Medium-range forecast errors associated with active episodes of the Madden-Julian Oscillation, *Mon. Weather Rev.*, 128, 69–86

11. Huffman, G. J., R. F. Adler, M. M. Morrissey, D. T. Bolvin, S. Curtis, R. Joyce, B.McGavock, J. Susskind, 2001: Global precipitation at one-degree daily resolution from multisatellite observations. *Journal of Hydrometeorology*. 2, 36-50.

12. Inness, P. M., and J. M. Slingo, 2003: Simulation of the Madden– Julian Oscillation in a coupled general circulation model I: Comparison with observations and an atmosphere-only GCM. *J. Climate*, 16, 345–364.

13. Inness, P. M., J. M. Slingo, E. Guilyardi, and J. Cole, 2003: Simulation of the Madden-Julian Oscillation in a coupled general circulation model. Part II: The role of the basic state. *J. Climate*, 16, 365–382.

14. Jiang, X., D. E. Waliser, D. Kim, M. Zhao, K. R. Sperber, W. Stern, S. D. Schubert, G. J. Zhang, W. Wang, M. Khairoutdinov, R. Neale, and M.-I., Lee, 2011: Simulation of the intraseasonal oscillation over the Eastern Pacific ITCZ in climate models, *Climate Dynamics*, in press.

15. Jin, F.-F., D. Neelin, and M. Ghil, 1996: El Nino/Southern Oscillation and the annual cycle: Subharmonic frequency locking and aperiodicity. *Physica D*, 98, 442–465.

16. Kalnay, E., and Coauthors, 1996: The NCEP/NCAR 40-year reanalysis project. *Bull. Amer. Meteor. Soc.*, 77, 437–471.

17. Kim, D., A. H. Sobel, E. D. Maloney, D. M. W. Frierson, I. Kang, 2011: A systematic relationship between intraseasonal variability and mean state bias in AGCM simulations. *J. Climate*, 24, 5506–5520.

18. Kemball-Cook, S., B. Wang, and X. Fu, 2002: Simulation of the intraseasonal oscillation in the ECHAM-4 model: The impact of coupling with an ocean model, *J. Atmos. Sci.*, 59, 1433–1453.

19. Knutson, T. R. and K. M. Weickmann, 1987: 30-60 day atmospheric oscillations: Composite life cycles of convection and circulation anomalies. *Mon. Wea. Rev.*, 115, 1407-1436.

20. Krishnamurti, T. N., P. K. Jayakumar, J. Sheng, N. Surgi, andA. Kumar, 1985: Divergent circulations on the 30 to 50 daytime scale, *J. Atmos. Sci.*, 42, 364–375.

21. Landu, K., and E. D. Maloney, 2011: Understanding intraseasonal variability in an aquaplanet GCM. *J. Meteor. Soc. Japan*, 89, 195-210.

22. Lin, X., and R. H. Johnson, 1996: Kinematic and thermodynamic characteristics of the flow over the western Pacific warm pool during TOGA-COARE. *J. Atmos. Sci.* 53, 695-715

23. Madden, R. A. and P. R. Julian, 1971: Detection of a 40–50 day oscillation in the zonal wind in the tropical pacific. *J. Atmos. Sci.*, 28, 702–708.

24. Madden, R. A., and P. R. Julian, 1994: Observations of the 40-50 day tropical oscillation: a review. *Mon. Wea. Rev*., 122, 814-837.

25. Maloney, E. D. and D. L. Hartmann, 1998: Frictional moisture convergence in a composite life cycle of the Madden-Julian oscillation. *J. Climate*, 11, 2387-2403

26. Maloney, E. D., and D. L. Hartmann, 2000: Modulation of eastern north Pacific hurricanes by the Madden-Julian oscillation. *J. Climate*, 13, 1451-1460.

27. Maloney, E. D., and D. L. Hartmann, 2001: The Madden-Julian oscillation, barotropic dynamics, and north Pacific tropical cyclone formation. Part I: Observations. *J. Atmos. Sci.*, 58, 2545-2558.

28. Maloney, E. D., and J. T. Kiehl, 2002(a): MJO-related SST variations over the tropical eastern Pacific during Northern Hemisphere summer. *J. Climate*, 15, 675-689.

29. Maloney, E. D., and J. T. Kiehl, 2002(b): Intraseasonal eastern Pacific precipitation and SST variations in a GCM coupled to a slab ocean model. *J. Climate*, 15, 2989-3007.

30. Maloney, E. D., 2002: An intraseasonal oscillation composite lifecycle in the NCAR CCM3.6 with modified convection. *J. Climate* , **15** , 964-982.

31. Maloney, E. D., and S. K. Esbensen, 2003: The amplification of east Pacific Madden-Julian oscillation convection and wind anomalies during June-November. *J. Climate*, 16, 3482-3497.

32. Maloney, E. D., and A. H. Sobel, 2004: Surface fluxes and ocean coupling in the tropical intraseasonal oscillation. J. Climate, 17, 4368–4386.

33. Maloney, E. D., and S. K. Esbensen, 2005: A modeling study of summertime east Pacific wind-induced ocean-atmosphere exchange in the intraseasonal oscillation. *J. Climate*, 18, 568-584.

34. Maloney, E. D., and S. K. Esbensen, 2007: Satellite and buoy observations of intraseasonal variability in the tropical northeast Pacific. *Mon. Weather Rev.,* 135 , 3-19.

35. Maloney, E. D., D. B. Chelton, and S. K. Esbensen, 2008: Subseasonal SST variability in the tropical eastern north Pacific during boreal summer. *J. Climate*, 21, 4149-4167.

36. Maloney, E. D., 2009: The moist static energy budget of a composite tropical intraseasonal oscillation in a climate model. J. Climate, 22, 711–729.

37. Maloney, E.D., A.H. Sobel, and W.M. Hannah, 2010: Intraseasonal variability in an aquaplanet general circulation model. *J. Adv. Model. Earth Syst.* 2(5), 24 pp.

38. Mapes, B.E., T.T. Warner, M. Xu, and A.J. Negri, 2003: Diurnal patterns of rainfall in northwestern South America. Part I: Observations and context. *Mon. Weather Rev.,* 131, 799-812.

39. Mapes, B.E., T.T. Warner, and Mei Xu, 2003: Diurnal patterns of rainfall in northwestern South America. Part III: Diurnal gravity waves and nocturnal convection offshore. *Mon. Weather Rev.,* 131, 830-844.

40. Mathews, A. J., 2000, Propagation mechanisms for the Madden-Julian Oscillation, *Quart. J. R. Met. Soc.*, 126, 2637–2651.

41. McPhaden, M. J. 1999: Genesis and evolution of the 1997 – 98 El Nino. *Science*, 283, 950–954.

42. McPhaden, M. J. 2004: Evolution of the 2002/2003 El Nino, *Bull. Amer. Meteor. Soc.*, 85, 677–695.

43. Milliff, R. F. and R. A. Madden, 1996: The existence and vertical structure of fast, eastward-moving disturbances in the equatorial troposphere, *J. Atmos. Sci.*, 53, 586–597.

44. Moorthi, S., and M. J. Suarez, 1992: Relaxed Arakawa–Schubert: A parameterization of moist convection for general circulation models. Mon. Weather Rev., 120, 978–1002.

45. Neale, R. B., J. H. Richter, M. Jochum, 2008: The Impact of Convection on ENSO: From a Delayed Oscillator to a Series of Events. *J. Climate*, **21**, 5904–5924.

46. Neelin, D. J., I. M. Held, 1987: Modeling tropical convergence based on the moist static energy budget. *Mon. Weather Rev.*, 115, 3–12.

47. Nolan, D. S., C. Zhang, and S.-H.Chen, 2007: Dynamics of the shallow Circulation around ITCZ regions. *J. Atmos. Sci*., 64, 2262-2285.

48. Nolan, D. S., S. W. Powell, C. Zhang, and B. E. Mapes, 2010: Idealized simulations of the ITCZ and its multi-level flows. *J. Atmos. Sci ., 67* , 4028-4053.

49. North, G. R., T. L. Bell, R. F. Cahalan, Fanthune J. Moeng, 1982: Sampling Errors in the Estimation of Empirical Orthogonal Functions. *Mon. Wea. Rev.*, 110, 699–706.

50. Peters, M. E., Z. Kuang, C. C. Walker, 2008: Analysis of atmospheric energy transport in ERA-40 and implications for simple models of the mean tropical circulation. *J. Climate*, 21, 5229–5241.

51. Raymond, D. J., 2001: A new model of the Madden–Julian Oscillation. *J. Atmos. Sci.*, 58, 2807–2819.

52. Raymond, D.J., S. Sessions, A. Sobel, and Z. Fuchs, 2009: The mechanics of Gross moist stability. *J. Adv. Model. Earth Syst.* 1(9), 20 pp.

53. Raymond, D. J., and Z. Fuchs, 2009: Moisture modes and the Madden-Julian oscillation. *J. Climate*, 22, 3031-3046.

54. Small, R.J., S.-P. Xie and Y. Wang, 2003: Numerical simulation of atmospheric response to Pacific tropical instability waves. *J. Climate*, 16, 3723-3741.

55. Small R. J., Xie S-P., Y. Wang, S. K. Esbensen and D. Vickers, 2005: Numerical simulation of boundary layer structure and cross-equatorial flow in the eastern Pacific, *J. Atmos. Sci.,* 62, 1812-1830.

56. Small, R. J., S.-P. Xie, E. D. Maloney, S. P. deSzoeke, and Toru Miyama, 2010: Intraseasonal variability in the far-east Pacific: Investigation of the role of air-sea coupling in a regional coupled model. *Clim. Dyn.*, 36, 867-890.

57. Sobel, A. H., J. Nilsson, L. M. Polvani, 2001: The weak temperature gradient approximation and balanced tropical moisture waves. *J. Atmos. Sci.*, 58, 3650–3665.

58. Sobel, A.H., E.D. Maloney, G. Bellon, and D.M. Frierson, 2010: Surface fluxes and tropical intraseasonal variability: a reassessment. *J. Adv. Model. Earth Syst.* 2(2), 27 pp.

59. Sud, Y. C., and A. Molod, 1988: The roles of dry convection, cloud–radiation feedback processes, and the influence of recent improvements in the parameterization of convection in the GLA GCM. Mon. Weather Rev., 116, 2366–2387.

60. Tokioka, T., K. Yamazaki, A. Kitoh, and T. Ose, 1988: The equatorial 30-60 day oscillation and the Arakawa-Schubert penetrative cumulus parameterization. J. Meteor. Soc. Japan, 66, 883–901.

61. Waliser, D. E., K. M. Lau, and J.-H. Kim, 1999: The influence of coupled sea surface temperatures on the Madden-Julian Oscillation: A model perturbation experiment. *J. Atmos. Sci.,* 56, 333-358.

62. Wang, B., 1988: Dynamics of tropical low-frequency waves: An analysis of the moist Kelvin wave. *J. Atmos. Sci.*, 45, 2051-2065

63. Wang, B. and T. Li, 1994: Convective Interaction with Boundary-Layer Dynamics in the Development of a Tropical Intraseasonal System. *J. Atmos. Sci.*, 51, 1386–1400.

64. Wang, C., and D. B. Enfield, 2003: A further study of the tropical Western Hemisphere warm pool. *J. Climate,* 16, 1476–1493.

65. Wang, Y., S.-P. Xie, Xu, H. and B. Wang, 2004: Regional model simulations of marine boundary layer clouds over the Southeast Pacific off South America. Part I: Control experiment. *Mon. Weather Rev.*, 132, 274-296.

66. Wheeler, M.C., and H.H. Hendon, 2004: An all-season real-time multivariate MJO Index: Development of an index for monitoring and prediction. *Mon. Weather Rev.*, 132, 1917-1932.

67. Xie, S.-P., H. Xu, W.S. Kessler, and M. Nonaka, 2005: Air-sea interaction over the eastern Pacific warm pool: Gap winds, thermocline dome, and atmospheric convection. *J. Climate*, 18, 5-25.

68. Xie, S.-P., T. Miyama, Y. Wang, H. Xu, S.P. de Szoeke, R.J. Small, K.J. Richards, T. Mochizuki, and T. Awaji, 2007: A regional ocean-atmosphere model for eastern Pacific climate: Towards reducing tropical biases. *J. Climate*, 20, 1504-1522.

69. Xie S-P, K. Hu, J. Hafner , H. Tokinaga , Y. Du, G. Huang, T. Sampe, 2009: Indian Ocean capacitor effect on Indo-Western Pacific climate during the summer following El Nino. *J. Clim*ate, 22, 730-747

70. Xu, H., S.-P. Xie, Y. Wang, and R. J. Small, 2005: Effects of Central American mountains on the eastern Pacific winter ITCZ and moisture transport. *J. Climate,* 18, 3856–3873.

71. Yu, W., W. Han, E. D. Maloney, D. Gochis, and S.-P. Xie, 2011: Observations of eastward propagation of atmospheric intraseasonal oscillations from the Pacific to the Atlantic, *Journal of Geophysical Research,* 116, D02101,

72. Zhang, G. J., and N. A. McFarlane, 1995: Sensitivity of climate simulations to the parameterization of cumulus convection in the Canadian Climate Centre general circulation model. Atmos.–Ocean, 33, 407–446

73. Zhang, C. and M. J. McPhaden, 2000: Intraseasonal surface cooling in the equatorial western Pacific. *J. Climate,* 13, 2261-2276.

74. Zhang, C., M. McGauley, and N.A. Bond, 2004: Shallow meridional circulation in the tropical eastern Pacific. *J. Climate*, 17, 133-139.

75. Zhang, C. and M. Dong, 2004: Seasonality of the Madden-Julian Oscillation. *J. Climate*, 17, 3169-3180.

76. Zhang, C., 2005: The Madden Julian Oscillation, *Reviews of Geophysics*, 43, RG2003.

77. Zhang, C, M. Dong, S. Gualdi, H. H. Hendon, E. D. Maloney, A. Marshall, K. R. Sperber, and W. Wang, 2006: Simulations of the Madden-Julian Oscillation by four pairs of coupled and uncoupled global models. *Climate Dynamics*, 27, 573-592.